UNIVERSITY OF MINNESOTA

This is to certify that I have examined
this bound copy of a doctoral thesis by

Norihiro IZUMI

and have found that it is complete and satisfactory in all respects,
and that any and all revisions required by the final
examining committee have been made.

_____

Name of Faculty Adviser(s)

_____

Signature of Faculty Adviser(s)

_____

Date

GRADUATE SCHOOL

CHANNELIZATION AND DRAINAGE BASIN FORMATION IN COHESIVE SOILS

A THESIS

SUBMITTED TO THE FACULTY OF THE GRADUATE SCHOOL

OF THE UNIVERSITY OF MINNESOTA

BY

NORIHIRO IZUMI

IN PARTIAL FULFILLMENT OF THE REQUIREMENTS

FOR THE DEGREE OF

DOCTOR OF PHILOSOPHY

SEPTEMBER, 1993

ACKNOWLEDGEMENTS

The author wishes to express his sincere gratitude to his advisor, Professor Gary Parker, who guided the thesis research.

This research was funded by the United States Science Foundation, through grants No. CTS–8901598. The author also received support from the following sources: The University of Minnesota Department of Civil and Mineral Engineering (Civil Engineering Fellowship), and Graduate School (Grant–in–Aid of Research, Artistry and Scholarship). The author greatly appreciates these supports.

The author is grateful for all the helps given to him by people in the Unites States of America.

ABSTRACT

Analytical models for explaining the mechanism of drainage basin formation in cohesive soils are presented. A sheet flow on a plateau is assumed to cause erosion and the resulting channelization. Two different kinds of models are proposed.

In the "step foot erosion model", a linear stability analysis is brought to bear considering erosion right under a step (at the foot of the step) at the downstream end of a tilted plateau. The model predicts that infinitesimally small basin spacing tends to dominate. It is found that, while explaining an instability giving rise to channelization, the "step foot erosion model" cannot explain the mechanism of drainage basin wavelength selection.

Models for upstream–driven and downstream–driven channel inception using a "threshold hypothesis" for bed erosion on the plateau are then proposed. The models predict that a basin spacing of the order of depth divided by slope tends to dominate. The "threshold hypothesis" provides successful results to explain the mechanism of wavelength selection.

It is suggested that the surface erosion is substantial in the process of channelization and drainage basin wavelength selection.

TABLE OF CONTENTS

page

ACKNOWLEDGEMENTS i

ABSTRACT ii

TABLE OF CONTENTS iii

LIST OF FIGURES vi

LIST OF VARIABLES viii

1. INTRODUCTION 1

2. GOVERNING EQUATIONS 5

2.1 Governing equations for flow 5

2.1.1 St. Venant shallow water equations 5

2.1.2 Bed shear stresses 12

2.1.3 Reynolds stresses 12

2.2 Governing equation for erosion 14

3. STABILITY ANALYSIS OF DRAINAGE BASIN INCEPTION – STEP FOOT EROSION MODEL – 17

3.1 Introduction 17

3.2 Conceptual model 17

3.3 Formulation 18

3.3.1 Governing relations and linearization 18

3.3.2 Zeroth order solution; the base flow 23

3.3.3 Reduction of the first order problem 27

3.4 Solution 30
3.4.1 Outer layer, intermediate layer and inner layer 30
3.4.2 Solution in the outer layer 31
3.4.3 Solution in the inner layer 35
3.4.4 Solution in the intermediate layer 40
3.5 Stability analysis 41
3.6 Conclusions 47

4. USTREAM–DRIVEN DRAINAGE BASIN INCEPTION USING A THRESHOLD HYPOTHESIS 57
4.1 Introduction 57
4.2 Conceptual model 57
4.3 Formulation 60
4.3.1 Governing relations 60
4.3.2 Base flow solution; base–normal flow 61
4.3.3 Normalizations 64
4.4 Solution 66
4.4.1 Normal flow assumption 67
a) Linear analysis 67
b) Full nonlinear analysis 71
4.4.2 Linear analysis including the backwater and the Reynolds stress 74
a) Boundary and integral conditions 76
b) Solution at $O(a^0)$ 77
c) Solution at $O(a^1)$ 80

4.5 Threshold hypothesis 85
4.6 Discussion 89
4.7 Conclusions 91

5. DOWNSTREAM–DRIVEN DRAINAGE BASIN INCEPTION USING A THRESHOLD HYPOTHESIS 102
5.1 Introduction 102
5.2 Conceptual model 102
5.3 Formulation 104
5.4 Solution 108
5.4.1 Solution in the outer region 108
5.4.2 Solution in the inner region 113
a) Transformation 115
b) Solution in the outer layer 119
c) Solution in the inner layer 121
d) Solution in the intermediate layer 123
5.4.3 Composite solution 124
5.5 Threshold hypothesis 127
5.6 Conclusion 134

6. SUMMARY AND CONCLUSIONS 142
7. REFERENCES 145

LIST OF FIGURES

Figure 2–1. Coordinate system

Figure 3–1. Schematic diagram showing a plateau with a step. Flow is in the negative y direction.

Figure 3–2. Schematic diagram showing the backwater–driven tendency for flow to concentrate in the indentations of a sinuous step bounding a plateau.

Figure 3–3. Schematic diagram of the resulting system of basins.

Figure 3–4. Conformal transformation defined by (3–12) in which ak = 0.3.

Figure 3–5. Velocity and depth profiles for the case F = 0.5 and k = 4. (a) $u_1^\star$, (b) $v_1^\star$, (c) $h_1^\star$.

Figure 3–6. Velocity vectors near the step on the plateau for the case F = 0.5, k = 4 and a = 0.025.

Figure 3–7. Definition diagram showing the parameters $\tilde{Y}_e$, $\tilde{Y}_0$, and $\tilde{y}_e$.

Figure 3–8. Definition diagram showing the relation between $\tilde{c}_r$ and $\tilde{Y}$.

Figure 3–9. Flow intensification C_2 versus wavenumber k and the Froude number F.

Figure 4–1. Schematic diagram showing a plateau. Flow is in the positive y direction.

Figure 4–2. Schematic diagram showing perturbation on the plateau.

Figure 4–3. Schematic diagram showing upstream–driven channel inception

Figure 4–4. Definition diagram showing parameter $\psi = H_{th}/(SL_{th})$.

Figure 4–5. Streamline derived from the nonlinear analysis of normal flow assumption

Figure 4–6. Velocity and depth profiles for the case F = 0.5, and ψ = 0, 0.017 and 0.17. (a) v_0, (b) h_0.

Figure 4–7. Profile of v_1^* for the cases k = 0.3, 3 and 30, F = 0.5, ψ = 0.017, and ϵ = 0.00017.

Figure 4–8. Perturbed threshold distance ℓ_1 versus k and ψ for the case F = 0.5 and ϵ = 0.00017.

Figure 4–9. Schematic diagram showing long–time processes of drainage basin development.

Figure 5–1. Schematic diagram showing a plateau with a sinuous step at the downstream end. Note that the plateau is tilted but absolutely flat. Flow is in the positive y direction.

Figure 5–2. Definition diagram parameter $\psi = H_0/(SL_B)$.

Figure 5–3. Schematic diagram showing the outer and inner regions, and the outer, intermediate and inner layers.

Figure 5–4. Dimensionless threshold shear stress τ_{th} versus ℓ_0 and C_s.

Figure 5–5a. Perturbed threshold distance ℓ_1 versus k and ℓ_0 for the case C_s = 4 (F = 0.5).

Figure 5–5b. Perturbed threshold distance ℓ_1 versus k and ℓ_0 for the case C_s = 25 (F = 0.2).

LIST OF VARIABLES

A_p = a given area in eqn. (4–55);

A_0 = constant in eqn. (5–71);

A_1 = constant in eqn. (5–79a);

A_2 = constant in eqn. (5–79b, c);

a = dimensionless perturbation amplitude;

$\tilde{a}$ = perturbation amplitude;

a_0 = perturbation amplitude at $t = 0$;

B_0 = constant in eqn. (4–43);

B_1 = constant in eqn. (4–53) expressed by (4–54);

b = constant in eqn. (3–82a) expressed by (3–82c);

C_f = friction factor;

C_s = $C_f/S = F^{-2}$;

C_0 = constant in eqn (3–59);

C_1 = constant in eqn. (3–73a) corresponding to u_1 at the indentation of the step;

C_2 = constant in eqn. (3–73b) corresponding to v_1 at the indentation of the step;

c_r = dimensionless retreat speed of the step;

$\tilde{c}_r$ = retreat speed of the step;

c_{r0} = retreat speed of the base state;

E = erosion rate;

E_s = coefficient of the erosion function in (2–27);

F = $V_\infty/\sqrt{gH_\infty}$ in Chapter 3; and $V_{th}/\sqrt{gH_{th}}$ in Chapter 4;

$\bar{F}_i$ = time–averaged volume force per unit mass in the $\tilde{x}_i$ direction;

f_e = function of retreat speed;

f_0 = free function of y;

G = $\left[\frac{2}{3}F^{-2}(F^{-2}-1)\right]^{1/2}$;

g = gravitational acceleration;

H_{th} = depth for the threshold condition;

H_0 = depth at the step;

H_∞ = depth infinitely far upstream;

h = dimensionless local depth, equal to $\tilde{h}/H_\infty$ in Chapter 3; $\tilde{h}/H_{th}$ in Chapter 4, and $\tilde{h}/H_0$ in Chapter 5;

$\tilde{h}$ = local depth;

h_r = reference depth;

h_0 = depth of base flow;

h_1 = perturbed depth at order $O(a)$;

h_{01} = perturbed depth at order $O(a^0\delta^{1/2})$;

h_{10} = perturbed depth at order $O(a^1\delta^0)$;

h_{000} = depth of base–normal flow;

h_{010} = perturbation of v at order $O(a^0\psi^1\epsilon^0)$;

h_{001} = perturbation of v at order $O(a^0\psi^0\epsilon^1)$;

h_{100} = perturbation of v at order $O(a^1\psi^0\epsilon^0)$;

h_{110} = perturbation of v at order $O(a^1\psi^1\epsilon^0)$;

h_{101} = perturbation of v at order $O(a^1\psi^0\epsilon^1)$;

h_{020} = perturbation of v at order $O(a^0\psi^2\epsilon^0)$;

h_{011} = perturbation of v at order $O(a^0\psi^1\epsilon^1)$;

h_{002} = perturbation of v at order $O(a^0\psi^0\epsilon^2)$;

I	=	rainfall intensity;
$\underset{\sim}{\mathcal{I}}$	=	identity matrix;
J	=	Jacobian of transformation;
k	=	dimensionless perturbation wavenumber, equal to $\tilde{k}H_{\infty}/S$ in Chapter 3; $\tilde{k}H_{th}/S$ in Chapter 4; and $\tilde{k}H_0/S$ in Chapter 5;
$\tilde{k}$	=	perturbation wavenumber;
k_c	=	characteristic wavenumber;
$\underset{\sim}{\mathscr{L}}$	=	algebraic linear operator defined by (3–48c) in Chapter 3; and (5–69c) in Chapter 5;
$\underset{\sim}{\mathscr{L}}^0$	=	$\underset{\sim}{\mathscr{L}}$ in the outer layer;
ℓ	=	dimensionless threshold distance, from the divide in Chapter 4; and from the base mode downstream edge in Chapter 5;
$\tilde{\ell}$	=	threshold distance from the divide;
$\Delta\ell$	=	deviation from the threshold distance predicted from the base normal solution;
ℓ_0	=	threshold distance from the base mode downstream edge;
ℓ_1	=	perturbed threshold distance;
$\Delta\ell_0$	=	$\Delta\ell$ at order $O(a^0)$;
$\Delta\ell_1$	=	$\Delta\ell$ at order $O(a^1)$;
M	=	$\left[\frac{2}{3}(C_s-1)\right]^{1/2}$;
$\mathscr{m}$	=	vector defined by (3–48d) in Chapter 3; and (5–69d) in Chapter 5;
$\mathscr{m}^0$	=	$\mathscr{m}$ in the outer layer;
N	=	constant in eqn. (3–82a) expressed by (3–82b);
n_p	=	unit normal vector;

$\tilde{p}$	=	local time–averaged pressure;
$\tilde{q}$	=	water discharge per unit width;
$\tilde{q}_e$	=	$\tilde{q}$ evaluated at the edge of the plateau;
$\tilde{q}_r$	=	reference value of $\tilde{q}$;
q_x	=	x component of discharge vector = uh;
q_y	=	y component of discharge vector = vh;
$\vec{q}$	=	vectorial volume sediment transport rate per unit width;
S	=	slope of the plateau;
S_p	=	closed circle surrounding A_p in Figure 5–5;
t	=	dimensionless time;
$\tilde{t}$	=	time;
$\tilde{\mathscr{U}}$	=	$(u^2 + v^2)^{\frac{1}{2}}$;
U_0	=	velocity of the base flow at the edge of the sink;
u	=	dimensionless velocity in the transverse direction, corresponding to the ξ direction in Chapters 3 and 5; and the x direction in Chapter 4;
$\mathscr{u}$	=	solution vector defined by (3–48b) in Chapter 3; and (5–69b) in Chapter 5;
u'	=	dimensionless velocity in the x direction (transverse) in Chapters 3 and 5;
u''	=	u'/ψ;
$\tilde{u}$	=	depth–averaged velocity in the $\tilde{x}$ direction;
u^*	=	friction velocity;
u_r	=	reference velocity;
$\tilde{u}_i$	=	depth–averaged velocity in the $\tilde{x}_i$ direction;

u_1 = perturbation of u at order $O(a)$;

u_{100} = perturbation of u at order $O(a^1\psi^0\epsilon^0)$

u_{110} = perturbation of u at order $O(a^1\psi^1\epsilon^0)$;

u_{101} = perturbation of u at order $O(a^1\psi^0\epsilon^1)$;

u_{020} = perturbation of u at order $O(a^0\psi^2\epsilon^0)$

u_{011} = perturbation of u at order $O(a^0\psi^1\epsilon^1)$;

u_{002} = perturbation of u at order $O(a^0\psi^0\epsilon^2)$;

u_h = homogeneous part of u;

u_i = inhomogeneous part of u;

u^o = value of u in the outer layer;

$u_1^\star$ = $u_1/\sin k\xi$ in Chapters 3 and 5; and $u_1/\sin kx$ in Chapter 4;

$\tilde{u}_n$ = normal component of velocity normal to the step;

V_0 = velocity at the edge of the step;

V_∞ = velocity of the uniform flow in the region far upstream;

V_{th} = velocity of the threshold condition of erosion;

v = dimensionless velocity in the streamwise direction, corresponding to the η direction in Chapter 3 and 5; and the y direction in Chapter 4;

v' = dimensionless velocity in the y direction (streamwise) in Chapters 3 and 5;

$\tilde{v}$ = velocity in the y direction;

v_0 = base value of v;

v_1 = perturbation of v at order $O(a)$;

v_{01} = perturbation of v at order $O(a^0\delta^{1/2})$;

v_{10} = perturbation of v at order $O(a\delta^0)$;

v_{000} = base value of v;

v_{010} = perturbation of v at order $O(a^0\psi^1\epsilon^0)$;

v_{001} = perturbation of v at order $O(a^0\psi^0\epsilon^1)$;

v_{100} = perturbation of v at order $O(a^1\psi^0\epsilon^0)$;

v_{110} = perturbation of v at order $O(a^1\psi^1\epsilon^0)$;

v_{101} = perturbation of v at order $O(a^1\psi^0\epsilon^1)$;

v_{020} = perturbation of v at order $O(a^0\psi^2\epsilon^0)$;

v_{011} = perturbation of v at order $O(a^0\psi^1\epsilon^1)$;

v_{002} = perturbation of v at order $O(a^0\psi^0\epsilon^2)$;

$v_1^\star$ = $v_1/\cos k\xi$ in Chapters 3 and 5; and $v_1/\cos kx$ in Chapters 4;

x = dimensionless x coordinate (transverse), equal to $\tilde{x}/(H_\infty/S)$ in Chapter 3; $\tilde{x}/(H_{th}/S)$ in Chapter 4; and $\tilde{x}/(H_0/S)$ in Chapter 5;

$\tilde{x}$ = x coordinate (transverse);

x_b = x coordinate of the point B in Figure 4–5;

x_p = x coordinate of the point P in Figure 4–5;

$\tilde{x}_i$ = x_i coordinate;

Y = meaningful parameter in (1–3);

Y_e = dimensionless y coordinate of the location of the edge;

$\tilde{Y}_e$ = y coordinate of the location of the edge;

y = dimensionless y coordinate (streamwise), equal to $\tilde{y}/(H_\infty/S)$ in Chapter 3; $\tilde{y}/L_{th}$ in Chapter 4, and $\tilde{y}/L_B$ in Chapter 5;

$\tilde{y}$ = y coordinate (streamwise);

$\hat{y}$ = y/ψ;

y' = variable in the inner region = $(1-y)/\psi$;

y_e = dimensionless y coordinate of the edge;

y_b = y coordinate of the point B in Figure 4–5;

y_p = y coordinate of the point P in Figure 4–5;

$\tilde{y}_e$ = y coordinate of the edge;

z = z coordinate in the complex plane = x + iy;

$\tilde{z}$ = z coordinate (upward normal to the land surface);

α = coefficient of the eddy viscosity in (2–26);

$\tilde{\alpha}$ = shape factor for the vertical distribution of velocity;

γ = exponent of the erosion function in (2–27);

δ = thickness of the inner layer;

ϵ = dimensionless eddy viscosity = $\alpha S^2/C_f^{1/2}$;

ζ = complex variable in the complex plane equal to $\xi + i\eta$;

η = η coordinate (streamwise) in Chapters 3 and 5;

η^* = normalized η coordinate in the inner layer = $\delta^{-1}\eta$;

η_i = interface between the outer and intermediate layer;

$\tilde{\eta}_b$ = bed elevation;

θ = angle between the downstream edge and $\tilde{x}$ axis;

θ_i = angle of inclination;

λ_n = the nth eigenvalue;

λ_p = porosity of bed material;

λ_1 = negative eigenvalue;

$\tilde{\lambda}$ = perturbation wavelength;

$\tilde{\lambda}_c$ = characteristic basin spacing;

ν = kinematic viscosity;

ν_t = depth–averaged eddy viscosity in the horizontal direction;

ξ	=	ξ coordinate (transverse) in Chapters 3 and 5;
ξ^*	=	normalized ξ coordinate in the inner layer = $\delta^{-1}\xi$;
ρ	=	density of water;
σ	=	rate of tectonic uplift;
τ	=	dimensionless bed shear stress;
$\tilde{\tau}$	=	bed shear stress;
τ_x	=	dimensionless bed shear stress in the x direction;
τ_y	=	dimensionless bed shear stress in the y direction;
τ_{th}	=	dimensionless threshold bed shear stress = $\tilde{\tau}_{th}/\rho g V_0^2$;
$\tilde{\tau}_{th}$	=	threshold bed shear stress;
$\tilde{\tau}_x$	=	bed shear stress in the x direction;
$\tilde{\tau}_y$	=	bed shear stress in the y direction;
ψ	=	H_{th}/SL_{th} in Chapter 4; and H_0/SL_B in Chapter 5; and
ω	=	growth rate of perturbation.

1. INTRODUCTION

River drainage basins have long been of interest to geomorphologists and river specialists. Many researchers have tried to explain how drainage networks form on an originally flat surface of a plateau. Two famous examples of early work include Horton (1945) and Strahler (1958). Due to the complexity of the phenomenon, their work was limited to empirical description or qualitative explanation. A good summary of recent geomorphological literature on the subject can be found in Abrahams (1984).

It is only relatively recently that attempts have been made to develop theoretical models for the formation of drainage basins themselves, and the channel network within each basin.

A landmark analysis in which the concepts of nonlinear wave mechanics and linear stability analysis were brought to bear on the problem is that due to Smith and Bretherton (1972). In their analysis, the base state is taken to be a flat, tilted surface subjected to a uniform rainfall, giving rise to a base flow with a streamwise direction. Surface flow is modelled as normal flow directed parallel to the gradient of bed topography. Sediment discharge per unit width is computed by using a simple power relation including both water discharge per unit width and bed slope. Bed evolution is computed using the Exner equation of sediment continuity. This base state is then perturbed by defining infinitesimal troughs and ridges parallel to the direction of the base flow. The ridge–to–ridge spacing can then be interpreted as a wavelength λ; this allows for a linear stability analysis. One goal of such an analysis is determining the growth rate of perturbation amplitude as a function of wavenumber $\tilde{k}$, where $\tilde{k} = 2\pi/\lambda$. In linear stability analyses a typical assumption is

that the characteristic wavenumber that first tends to evolve is given by the one that maximizes perturbation growth rate. Unfortunately, however, the model of Smith and Bretherton predicts maximum growth rate for infinite $\tilde{k}$, i.e. a ridge spacing $\lambda = 0$.

Luke (1974) derived a nonlinear system of differential equations to describe evolution of landforms. His main concern was to obtain special solutions for the nonlinear differential equations. Though the equations he derived to describe landform evolution are further developed and extended than those in Smith and Bretherton's theory, Luke's analysis sheds no further light on the characteristic spacing of drainage basins.

Loewenherz (1991) has recently reconsidered the model of Smith and Bretherton. Her model achieves a maximum growth rate for a finite wavenumber only at the expense of introducing an ad–hoc "smearing function" to prevent the over–concentration of water in troughs.

In recent years, there has been a veritable explosion of literature on the subject of drainage basins. Since the present study concentrates on theoretical aspects of drainage basin formation, it suffices to mention work of a mechanistic nature. Foremost among these is the treatise of Willgoose et al. (1991); also of considerable value are the contributions made by Sawai et al. (1986), Roth et al. (1989), and Howard (1990; ref. as personal communication, 1993).

Of the above–quoted mechanistic models, those of Smith and Bretherton, Luke, Roth et al., Willgoose et al., and Loewenherz are all transportational in nature. That is, the governing equation for bed evolution used in each case can be cast in the following general form:

$$\frac{\partial \tilde{\eta}_b}{\partial \tilde{t}} - \sigma = -\frac{1}{(1 - \lambda_p)} \vec{\nabla} \cdot \vec{q}, \qquad (1\text{–}1)$$

where λ_p denotes porosity of bed material, $\tilde{t}$ denotes time, $\tilde{\eta}_b$ denotes bed elevation, σ denotes the rate of tectonic uplift, and $\vec{q}$ denotes the vectorial volume sediment transport rate per unit width. Bed elevation is seen to change in response to tectonic uplift and the differential transport of sediment.

The model of Sawai et al. alone, which is designed to explain rill formation in a badlands environment, treats the purely erosional problem for the case of cohesive sediment. Let $E = E(\tilde{\tau})$ denote the volume rate of erosion of material from the bed into suspension, which is taken to be a function of boundary shear stress $\tilde{\tau}$. In the case of erosion of cohesive material, it is often possible to assume that the eroded material is not redeposited due to the prevalence of below–capacity conditions for transport. The law for bed evolution now takes the form

$$\frac{\partial \tilde{\eta}_b}{\partial \tilde{t}} - \sigma = -E. \qquad (1\text{–}2)$$

The problem to be considered here is incisional drainage basin development in an environment of the type of a badlands or a loess plateau. With this in mind, (1–2) is adopted for bed evolution.

An incisional model based on pure erosion was adopted in this study, however, only after consideration of the work of Willgoose et al. (1991). Their very inspiring model is nevertheless based on an adaptation of a model due to Meinhardt (1982) originally designed to explain the formation of vein networks in leaves. As a result, a model which claims to be physically based contains a crucial equation

which has no real justification in the context of the problem under consideration.

This unjustified equation is the "Y" equation, which takes a form like

$$\frac{dY}{d\tilde{t}} = -0.1Y + \frac{Y^2}{1 + 9Y^2}. \qquad (1\text{–}3)$$

The role the equation plays in the theory is to provide a sudden "jump" condition that changes hillslope to channel. Its simple form, however, has yet to be derived from considerations of erodible–bed mechanics.

The final objective of this research is to study the mechanisms which operate to determine the spacing between drainage basins. In Chapter 3, a consideration of nonlinear wave mechanics and linear stability analysis of the type of Smith and Bretherton (1972), and Loewenherz (1991) is brought to bear, but in the different context of a purely erosional environment. This allows for the derivation of a physically–based "shock" condition that allows for the conversion of overland zones to channel zones through the mechanism of headcutting. In Chapters 4 and 5, an alternative to stability analysis that predicts the spacing between channels formed on the surface of the plateau is proposed. This is based on a consideration of the "threshold" discussed in Montgomery and Dietrich (1989).

2. GOVERNING EQUATIONS

2.1 Governing equations for flow

2.1.1 St. Venant shallow water equations

The surface of the earth displays a variety of interesting landforms created by fluvial action of flowing water. In most cases of interest, the scale of the landforms is much larger than the characteristic depth of the flow that sculpted them. In this analysis, then, the horizontal scale can be taken to be much larger than the scale of flow depth. As a result, the flow field can be approximated with the depth–averaged St. Venant shallow water equations. Because the effects of Reynolds stresses and a uniform rainfall will be considered in Chapter 5, the St. Venant equations including those effects need to be derived. While there are several studies which try to introduce the Reynolds stresses into the St. Venant equations (e.g., Rodi, 1982), a full derivation does not seem to be available. Therefore, this chapter begins with the derivation of the St. Venant equations including the effects of Reynolds stresses and a uniform rainfall.

The flow causing fluvial action is commonly turbulent, and can therefore be described by the Reynolds equations. For three–dimensional incompressible flow, the Reynolds equation and the continuity equation take the form

$$\frac{\partial \bar{u}_i}{\partial \tilde{t}} + \bar{u}_j \frac{\partial \bar{u}_i}{\partial \tilde{x}_j} = \bar{F}_i - \frac{1}{\rho} \frac{\partial \bar{p}}{\partial \tilde{x}_i} - \frac{\partial \overline{u_i' u_j'}}{\partial \tilde{x}_j} + \nu \frac{\partial^2 \bar{u}_i}{\partial \tilde{x}_j \partial \tilde{x}_j}, \tag{2–1}$$

$$\frac{\partial \bar{u}_j}{\partial \tilde{x}_j} = 0, \tag{2–2}$$

where $\tilde{x}_1$ and $\tilde{x}_2$ correspond to $\tilde{x}$ and $\tilde{y}$ respectively and are taken parallel to the land surface (Figure 2–1), $\tilde{x}_3$ correponds to $\tilde{z}$ and is taken upward orthogonal to the land surface, $\bar{u}_i$ is the time–averaged velocity component in the $\tilde{x}_i$ direction, $\bar{p}$ is local, time–averaged pressure, ρ is fluid density, ν is kinematic viscosity, and $\bar{F}_i$ is the time–averaged volume force per unit mass in the $\tilde{x}_i$ direction. Einstein's summation rule is applied hereafter. In the absence of qualification, the subscripts i and j take the values 1, 2 and 3.

Consider a plateau which is flat but slightly tilted. Then, the volume forces acting on flow on the plateau can be expressed by

$$\bar{F}_i = g \sin \theta_i, \quad i = 1, 2, \tag{2–3a}$$

$$\bar{F}_3 = - g \cos \theta_1 \cos \theta_2. \tag{2–3b}$$

Here g is gravitational acceleration and θ_i is angle of inclination in the $\tilde{x}_i$ direction. If θ_i is very small, the approximations $\sin \theta_i \simeq - \partial \tilde{\eta}_b / \partial \tilde{x}_i$, $\cos \theta_i \simeq 1$, where $\tilde{\eta}_b$ is bed elevation can be made. The volume force vector can thus be approximated by

$$\bar{F}_i = - g \frac{\partial \tilde{\eta}_b}{\partial \tilde{x}_i}, \quad i = 1, 2, \tag{2–4a}$$

$$\bar{F}_3 = - g. \tag{2–4b}$$

As described before, the horizontal scale is taken to be much larger than the scale of flow depth. Since the horizontal components of velocity are also much

larger than velocity in the upward normal direction, the inertia terms, Reynolds stress terms and viscous terms in the upward normal direction are all negligibly small. As a result, the case i = 3 in (2–1) is well approximated by the hydrostatic expression

$$-g-\frac{1}{\rho}\frac{\partial \bar{p}}{\partial \tilde{x}_3}=0. \tag{2–5}$$

Equation (2–5) is integrated to yield

$$\bar{p}=\rho g(\tilde{h}-\tilde{x}_3), \tag{2–6}$$

where the atmospheric pressure is set equal to be zero (gage pressure). Note that the assumption of hydrostatic distribution breaks down wherever abrupt changes of flow occur, such as in the immediate vicinity of a free overfall.

The procedure of depth–averaging is performed below. Adding (2–2) multiplied by $\bar{u}_i$ to (2–1), the following equation is obtained:

$$\frac{\partial \bar{u}_i}{\partial \tilde{t}}+\frac{\partial \bar{u}_i \partial \bar{u}_j}{\partial \tilde{x}_j}=-g\frac{\partial \tilde{\eta}_b}{\partial \tilde{x}_i}-g\frac{\partial \tilde{h}}{\partial \tilde{x}_i}-\frac{\partial \overline{u_i' u_j'}}{\partial \tilde{x}_j}+\nu\frac{\partial^2 \bar{u}_i}{\partial \tilde{x}_j \partial \tilde{x}_j},$$

$$i=1,\ 2. \tag{2–7}$$

The left hand side of (2–7) is depth–integrated as

$$\int_0^{\tilde{h}} \frac{\partial \bar{u}_i}{\partial \tilde{t}}\, d\tilde{x}_3 + \int_0^{\tilde{h}} \frac{\partial \bar{u}_i}{\partial \tilde{x}_j} \frac{\partial \bar{u}_j}{\partial \tilde{x}_j}\, d\tilde{x}_3$$

$$= \frac{\partial}{\partial \tilde{t}} \int_0^{\tilde{h}} \bar{u}_i \, d\tilde{x}_3 - \bar{u}_i|_{\tilde{x}_3=\tilde{h}} \frac{\partial \tilde{h}}{\partial \tilde{t}} + \frac{\partial}{\partial \tilde{x}_1} \int_0^{\tilde{h}} \bar{u}_i \bar{u}_1 \, d\tilde{x}_3 - \bar{u}_i \bar{u}_1|_{\tilde{x}_3=\tilde{h}} \frac{\partial \tilde{h}}{\partial \tilde{x}_1}$$

$$+ \frac{\partial}{\partial \tilde{x}_2} \int_0^{\tilde{h}} \bar{u}_i \bar{u}_2 \, d\tilde{x}_3 - \bar{u}_i \bar{u}_2|_{\tilde{x}_3=\tilde{h}} \frac{\partial \tilde{h}}{\partial \tilde{x}_2} + \bar{u}_i \bar{u}_3|_{\tilde{x}_3=\tilde{h}},$$

$$i = 1, 2. \qquad (2\text{–}8)$$

If the rainfall intensity is denoted by I, $\bar{u}_3$ at the water surface is given according to the kinematic boundary condition as

$$\bar{u}_3|_{\tilde{x}_3=\tilde{h}} + I = \frac{d\tilde{h}}{d\tilde{t}} = \frac{\partial \tilde{h}}{\partial \tilde{t}} + \bar{u}_j|_{\tilde{x}_3=\tilde{h}} \frac{\partial \tilde{h}}{\partial \tilde{x}_j}, \quad j = 1, 2. \qquad (2\text{–}9)$$

With the aid of (2–9), (2–8) reduces to

$$\int_0^{\tilde{h}} \frac{\partial \bar{u}_i}{\partial \tilde{t}}\, d\tilde{x}_3 + \int_0^{\tilde{h}} \frac{\partial \bar{u}_i}{\partial \tilde{x}_j} \frac{\partial \bar{u}_j}{\partial \tilde{x}_j}\, d\tilde{x}_3 = \frac{\partial}{\partial \tilde{t}} \int_0^{\tilde{h}} \bar{u}_i d\tilde{x}_3 + \frac{\partial}{\partial \tilde{x}_j} \int_0^{\tilde{h}} \bar{u}_i \bar{u}_j d\tilde{x}_3 - I\bar{u}_i \big|_{\tilde{x}_3=\tilde{h}},$$

$$i, j = 1, 2. \qquad (2\text{–}10)$$

The right–hand side of (2–7) is depth–integrated to yield

$$\int_0^{\tilde{h}}\Big(-g\frac{\partial\tilde{\eta}_b}{\partial\tilde{x}_i}-g\frac{\partial\tilde{h}}{\partial\tilde{x}_i}-\frac{\partial\overline{u_i'u_j'}}{\partial\tilde{x}_j}+\nu\frac{\partial^2\bar{u}_i}{\partial\tilde{x}_j\partial\tilde{x}_j}\Big)d\tilde{x}_3$$

$$=-g\tilde{h}\frac{\partial\tilde{\eta}_b}{\partial\tilde{x}_i}-g\tilde{h}\frac{\partial\tilde{h}}{\partial\tilde{x}_i}-\int_0^{\tilde{h}}\Big(\frac{\partial\overline{u_i'u_1'}}{\partial\tilde{x}_1}+\frac{\partial\overline{u_i'u_2'}}{\partial\tilde{x}_2}\Big)d\tilde{x}_3+\nu\int_0^{\tilde{h}}\Big(\frac{\partial^2\bar{u}_i}{\partial\tilde{x}_1\partial\tilde{x}_1}+\frac{\partial^2\bar{u}_i}{\partial\tilde{x}_2\partial\tilde{x}_2}\Big)d\tilde{x}_3$$

$$-\nu\frac{\partial\bar{u}_i}{\partial\tilde{x}_3}\Big|_{\tilde{x}_3=0},\quad i=1,2. \tag{2–11}$$

Equation (2–7) is thus depth–integrated to yield

$$\frac{\partial}{\partial\tilde{t}}\int_0^{\tilde{h}}\bar{u}_i d\tilde{x}_3+\frac{\partial}{\partial\tilde{x}_j}\int_0^{\tilde{h}}\bar{u}_i\bar{u}_j d\tilde{x}_3-I\bar{u}_i\big|_{\tilde{x}_3=\tilde{h}}=-g\tilde{h}\frac{\partial\tilde{\eta}_b}{\partial\tilde{x}_i}-g\tilde{h}\frac{\partial\tilde{h}}{\partial\tilde{x}_i}$$

$$-\int_0^{\tilde{h}}\frac{\partial\overline{u_i'u_j'}}{\partial\tilde{x}_j}d\tilde{x}_3+\nu\int_0^{\tilde{h}}\frac{\partial^2\bar{u}_i}{\partial\tilde{x}_j\partial\tilde{x}_j}d\tilde{x}_3-\frac{\tilde{\tau}_i}{\rho\tilde{h}},\quad i,j=1,2, \tag{2–12}$$

where $\rho\nu\partial\tilde{u}_i/\partial\tilde{x}_3\big|_{\tilde{x}_3=0}$ is denoted by $\tilde{\tau}_i$, which corresponds to the two dimensional ($i=1,2$) bed shear stress vector.

Depth–averaged velocity $\tilde{u}_i$ is defined as

$$\tilde{u}_i=\frac{1}{\tilde{h}}\int_0^{\tilde{h}}\bar{u}_i d\tilde{x}_3,\quad i=1,2. \tag{2–13}$$

The introduction of quasi–similarity hypothesis for the vertical distribution of velocity allows for the following expression:

$$\int_0^{\tilde{h}}\bar{u}_i\bar{u}_j d\tilde{x}_3=\tilde{\alpha}\,\tilde{u}_i\tilde{u}_j\tilde{h},\quad i,j=1,2, \tag{2–14}$$

where $\tilde{\alpha}$ is a shape factor that is known to be close to unity in the case of fully–developed turbulent flow. Hereinafter $\tilde{\alpha}$ is assumed to be unity. Since in fully turbulent flow the viscous stresses are usually much smaller than the Reynolds stresses, the fourth term on the right hand side of (2–12) is dropped. Then (2–12) reduces to

$$\frac{\partial}{\partial \tilde{t}}(\tilde{u}_i\tilde{h}) + \frac{\partial}{\partial \tilde{x}_j}(\tilde{u}_i\tilde{u}_j\tilde{h}) - I\bar{u}_i\big|_{\tilde{x}_3=\tilde{h}} = -g\tilde{h}\frac{\partial \tilde{\eta}_b}{\partial \tilde{x}_i} - g\tilde{h}\frac{\partial \tilde{h}}{\partial \tilde{x}_i} - \int_0^{\tilde{h}} \frac{\partial \overline{\tilde{u}_i'\tilde{u}_j'}}{\partial \tilde{x}_j}\, d\tilde{x}_3 - \frac{\tilde{\tau}_i}{\rho\tilde{h}}, \quad i, j = 1, 2, \tag{2–15}$$

or upon manipulation,

$$\frac{\partial \tilde{u}_i}{\partial \tilde{t}} + \tilde{u}_j\frac{\partial \tilde{u}_i}{\partial \tilde{x}_j} + \frac{\tilde{u}_i}{\tilde{h}}\left(\frac{\partial \tilde{h}}{\partial \tilde{t}} + \frac{\partial \tilde{u}_j\tilde{h}}{\partial \tilde{x}_j}\right) - \frac{I}{\tilde{h}}\bar{u}_i\big|_{\tilde{x}_3=\tilde{h}} = -g\frac{\partial \tilde{\eta}_b}{\partial \tilde{x}_i} - g\frac{\partial \tilde{h}}{\partial \tilde{x}_i} - \frac{1}{\tilde{h}}\int_0^{\tilde{h}} \frac{\partial \overline{\tilde{u}_i'\tilde{u}_j'}}{\partial \tilde{x}_j}\, d\tilde{x}_3 - \frac{\tilde{\tau}_i}{\rho\tilde{h}}, \quad i, j = 1, 2. \tag{2–16}$$

The continuity equation is depth–integrated as follows:

$$\int_0^{\tilde{h}} \frac{\partial \bar{u}_j}{\partial \tilde{x}_j}\, d\tilde{x}_3$$

$$= \frac{\partial}{\partial \tilde{x}_1}\int_0^{\tilde{h}} \bar{u}_1 d\tilde{x}_3 - \frac{\partial \tilde{h}}{\partial \tilde{x}_1}\bar{u}_1\big|_{\tilde{x}_3=\tilde{h}} + \frac{\partial}{\partial \tilde{x}_2}\int_0^{\tilde{h}} \bar{u}_2 d\tilde{x}_3 - \frac{\partial \tilde{h}}{\partial \tilde{x}_2}\bar{u}_2\big|_{\tilde{x}_3=\tilde{h}} + \bar{u}_3\big|_{\tilde{x}_3=\tilde{h}}$$

$$= 0. \tag{2–17}$$

With the use of (2–9) and (2–13), (2–17) reduces to

$$\frac{\partial \tilde{h}}{\partial \tilde{t}} + \frac{\partial \tilde{u}_j \tilde{h}}{\partial \tilde{x}_j} = I, \qquad j = 1, 2. \tag{2–18}$$

With the aid of (2–18), (2–16) yields the depth–averaged version of momentum equations of the form

$$\frac{\partial \tilde{u}_i}{\partial \tilde{t}} + \tilde{u}_j \frac{\partial \tilde{u}_i}{\partial \tilde{x}_j} + \frac{I}{\tilde{h}} (\tilde{u}_i - \bar{u}_i \big|_{\tilde{x}_3 = \tilde{h}}) = -g \frac{\partial \tilde{\eta}_b}{\partial \tilde{x}_i} - g \frac{\partial \tilde{h}}{\partial \tilde{x}_i}$$
$$- \frac{1}{\tilde{h}} \int_0^{\tilde{h}} \frac{\partial \overline{u_i' u_j'}}{\partial \tilde{x}_j} d\tilde{x}_3 - \frac{\tilde{\tau}_i}{\rho \tilde{h}}. \qquad i, j = 1, 2. \tag{2–19}$$

In the absence of clarification, i and j hereinafter take the values 1 and 2. Since the vertical profile of velocity is highly uniform in the case of fully developed turbulent flow, the difference between $\tilde{u}_i$ and $\bar{u}_i$ at $\tilde{x}_3 = \tilde{h}$ can be assumed to be small as long as secondary courrents are not very large. Then, the third term of the left–hand side of (2–19) can be neglected. In addition, the quasi–steady assumption is made in this study, according to which the time variation of flow is much faster than that of the landforms. In other words, the flow is assumed to react spontaneously to geomorphic change. With this in mind, the time derivative term in (2–19) is also neglected. The governing equations of the flow are then finally obtained as

$$\tilde{u}_j \frac{\partial \tilde{u}_i}{\partial \tilde{x}_j} = -g\frac{\partial \tilde{h}}{\partial \tilde{x}_i} - g\frac{\partial \tilde{\eta}_b}{\partial \tilde{x}_i} - \frac{1}{\tilde{h}}\int_0^{\tilde{h}} \frac{\partial \overline{\tilde{u}_i' \tilde{u}_j'}}{\partial \tilde{x}_j} d\tilde{x}_3 - \frac{\tilde{\tau}_i}{\rho \tilde{h}}, \tag{2–20}$$

$$\frac{\partial \tilde{u}_j \tilde{h}}{\partial \tilde{x}_j} = I. \tag{2–21}$$

2.1.2 Bed shear stresses

Bed shear stresses are evaluated with the use of a friction factor C_f;

$$\tilde{\tau}_i = \rho C_f \tilde{\mathscr{U}} \tilde{u}_i, \tag{2–22}$$

where $\tilde{\mathscr{U}}^2 = \tilde{u}_i \tilde{u}_i$. For the present analysis the crude assumption of constant C_f is made. Note that the above assumption renders $\tilde{\tau}_i$ parallel to $\tilde{u}_i$.

2.1.3 Reynolds stresses

According to the traditional Boussinesq assumption, the Reynolds stresses can be evaluated with the use of eddy viscosity ν_t and time–averaged local (i.e. not depth–averaged) velocity $\bar{u}$; that is

$$-\rho \overline{u_i' v_j'} = \rho \nu_t \frac{\partial \bar{u}_i}{\partial \tilde{x}_j}. \tag{2–23}$$

If a depth–averaged value of ν_t is adopted as an approximation, then ν_t is not a

function of $\tilde{x}_3$ and the Reynolds stresses in (2–20) are expressed by

$$-\frac{1}{\tilde{h}}\int_0^{\tilde{h}} \overline{\frac{\partial u_i' u_j'}{\partial \tilde{x}_j}}\, d\tilde{x}_3 = \frac{1}{\tilde{h}}\int_0^{\tilde{h}} \frac{\partial}{\partial \tilde{x}_j}(\nu_t \frac{\partial \tilde{u}_i}{\partial \tilde{x}_j}) d\tilde{x}_3$$

$$= \frac{\partial}{\partial \tilde{x}_j}(\nu_t \frac{\partial \tilde{u}_i}{\partial \tilde{x}_j}) + \frac{\partial}{\partial \tilde{x}_j}\Big[\frac{\nu_t}{\tilde{h}}\frac{\partial \tilde{h}}{\partial \tilde{x}_j}(\tilde{u}_i - \bar{u}_i|_{\tilde{x}_3=\tilde{h}})\Big]$$

$$+ \nu_t\Big[\frac{1}{\tilde{h}}\frac{\partial \tilde{h}}{\partial \tilde{x}_j}\Big]^2(\tilde{u}_i - \bar{u}_i|_{\tilde{x}_3=\tilde{h}}) + \frac{\nu_t}{\tilde{h}}\frac{\partial \tilde{h}}{\partial \tilde{x}_j}\Big[\frac{\partial \tilde{u}_i}{\partial \tilde{x}_j} - \frac{\partial \bar{u}_i}{\partial \tilde{x}_j}\Big|_{\tilde{x}_3=\tilde{h}}\Big]. \qquad (2\text{–}24)$$

As described before, the difference between $\tilde{u}_i$ and $\bar{u}_i$ at $\tilde{x}_3 = \tilde{h}$ can be assumed to be negligibly small, thus allowing for the neglect of the second, third and fourth terms of the right–hand side of (2–24), the depth–averaged Reynolds stress term approximates to a simple diffusional form. In addition, since (2–23) itself is already a crude assumption, the residual terms can be probably dropped with sufficient accuracy. Therefore, the following assumption is made in this study;

$$\frac{1}{\tilde{h}}\int_0^{\tilde{h}} \overline{\frac{\partial u_i' u_j'}{\partial \tilde{x}_j}}\, d\tilde{z} = \frac{\partial}{\partial \tilde{x}_j}(\nu_t \frac{\partial \tilde{u}_i}{\partial \tilde{x}_j}). \qquad (2\text{–}25)$$

The eddy viscosity in the horizontal direction is known to be slightly larger than the vertical eddy viscosity (e.g., Webel and Schatzman, 1984). In the similar manner to the depth–averaged eddy viscosity in the vertical direction, ν_t is assumed to be estimated by the form

$$\nu_t = \alpha \tilde{u}_r^* \tilde{h}_r. \qquad (2\text{–}26)$$

where α is a dimensionless constant, and $\tilde{u}_r^*$ and $\tilde{h}_r$ are a reference friction velocity and a characteristic depth associated with the turbulent structure of the corresponding flow field, respectively. In the case of channel flow, $\tilde{u}_r^*$ is set equal to the friction velocity, $\tilde{h}_r$ is set equal to depth at the channel center and α is taken to be 0.13 (Parker, 1978; Ikeda et al., 1990).

2.2 Governing equation for erosion

As noted previously, only purely erosional landforms sculpted into cohesive material are considered here. A large body of experimental work on the relation between the erosion rate and the boundary shear stress, or near–bed velocity, is available (e.g. Parthenaides, 1965; Arathurai and Arulanadan, 1978) A common empirical form for the erosion function is the power form

$$E = E_s(\tilde{\tau} - \tilde{\tau}_{th})^{\gamma}. \tag{2–27}$$

Here $\tilde{\tau}_{th}$ denotes a critical bed shear stress below which no erosion occurs. Furthermore, the parameter $\tilde{\tau}$ denotes the magnitude of the bed shear stress vector, i.e.

$$\tilde{\tau} = \sqrt{\tilde{\tau}_1^2 + \tilde{\tau}_2^2} = \rho C_f(\tilde{u}_1^2 + \tilde{u}_2^2). \tag{2–28}$$

The coefficients E_s and γ can be expected to be positive; otherwise, they are rather strongly dependent upon the physico–chemical properties of the material in question.

If the slope of the landform is sufficiently small, bed degradation per unit time is equal to the erosion rate, allowing for the use of the following form in the Exner equation;

$$\frac{\partial \tilde{\eta}_b}{\partial \tilde{t}} = -\frac{1}{1-\lambda_P} E_s (\tilde{\tau} - \tilde{\tau}_{th})^{\gamma}. \tag{2-29}$$

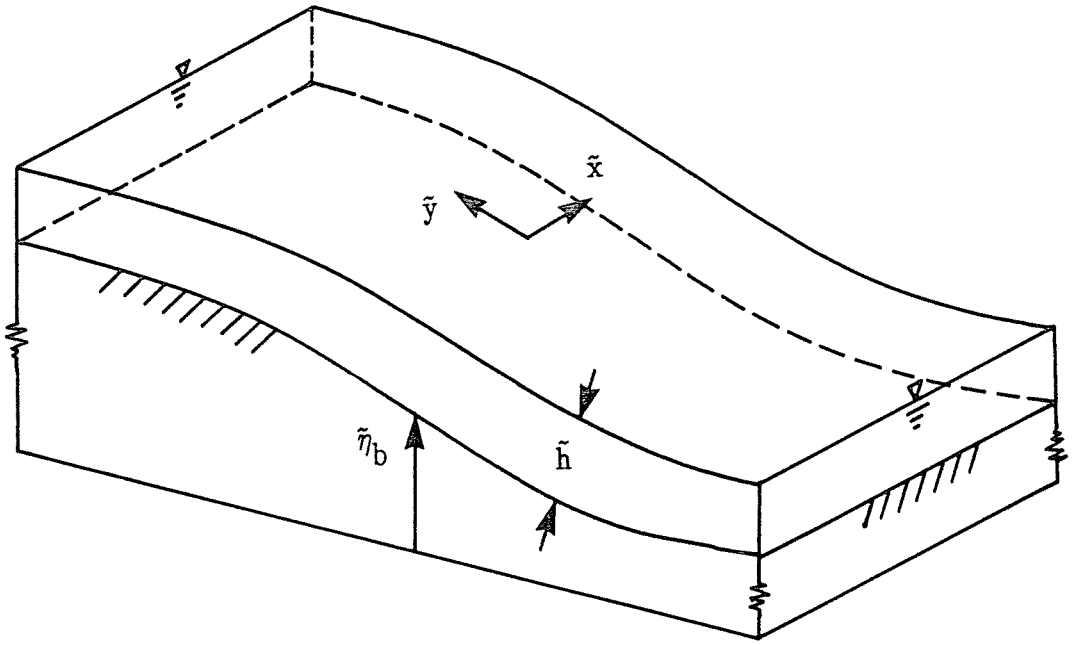

Figure 2–1. Coordinate system

3. STABILITY ANALYSIS OF DRAINAGE BASIN INCEPTION
– STEP FOOT EROSION MODEL –

3.1 Introduction

In this chapter, the first of several models of drainage basin inception is proposed. In order to allow for a simplified stability analysis, the assumption is made that erosion occurs only at the foot of the step ("step foot erosion model"). According to this simple assumption, the retreat speed of the step can be estimated solely as a function of discharge per unit width right under the step.

3.2 Conceptual models

Figure 3–1 shows a plateau composed of cohesive material which is flat, but which has a mild slope S in the $\tilde{y}$ direction. The downstream edge of the plateau terminates in a step–like overfall. It is assumed that a laterally uniform discharge of water is supplied at the upstream edge of the plateau, resulting in a continuous sheet flow that eventually cascades over the step. As noted in the figure, the $\tilde{y}$ coordinate is directed upslope, with its origin located at the step, and the $\tilde{x}$ coordinate is taken to be perpendicular to it.

Far upstream of the overfall, the flow is assumed to be in a normal, or equilibrium state. Here all the flow is directed in the $\tilde{y}$ direction, and depth and velocity are constant. The slope S is assumed to be low enough for the flow to be subcritical in the Froude sense. As the flow approaches the step, then, velocity increases and depth decreases in accordance with an M2 backwater curve. It is assumed that the magnitude of the boundary shear stress $\tilde{\tau}$ everywhere on the

plateau is below the critical value for bed erosion according to (2–27).

The edge of the step itself is first assumed to be perfectly straight and parallel to the $\tilde{x}$ direction. The flow cascades down at the step and reattaches to the erosible surface under the step. It is assumed that active erosion occurs at the foot of the step because of the strong impact of the falling water. One can visualize this erosion as resulting in the gradual upstream propagation of the step.

Suppose now that a small perturbation is given to the shape of the step, such that its edge is described by

$$\tilde{y} = \tilde{a} \cos \tilde{k}\tilde{x}, \tag{3–1}$$

where $\tilde{a}$ and $\tilde{k}$ are the amplitude and wave number of perturbation, respectively. In the present linear analysis, the amplitude is assumed to be small. As shown in Figure 3–2, then, the overfall is wavy in nature, consisting of alternating indentations and protuberances in the transverse direction. In the case of subcritical overland flow, the indentations should act to attract the flow, causing a gathering of streamlines. The protuberances should result in a commensurate repulsion of the flow, as illustrated in Figure 3–2. As a result, boundary shear stress under the overfall can be expected to be intensified near the indentations and reduced near the protuberances. The resulting differential erosion should cause the incision of incipient channels, each with its mouth located at a point of maximum indentation along the edge. The zones of highest erosion could be expected to gradually migrate upstream, each so forming an upward–extending channel acting as the main stem of an incipient drainage basin.

In this chapter, it is the above process that is postulated to be the cause of

channelization resulting in drainage basin formation. The transverse distance between each drainage basin would be given by the wavelength $\tilde{\lambda}$ of the perturbation (3–1), where $\tilde{\lambda} = 2\pi/\tilde{k}$. Although the present analysis considers only the initiation of this process, channel extension and bifurcation might be expected to result in the system of basins schematized in Figure 3–3, each containing a network of connected tributaries.

The main goal of the present analysis is the prediction of the distance $\tilde{\lambda}$ between adjacent drainage basins in terms of a standard linear stability analysis. If there exists a specific wavelength at which intensification at the indentations is maximized, perturbations with that wavelength should grow faster and thus tend to dominate. This provides a mechanism for the selection of spacing between drainage basins.

3.3 Formulation

3.3.1 Governing relations and linearization

In accordance with Figure 3–1, it is assumed that a flat plateau has a slight slope S ascending in the positive $\tilde{y}$ direction. Bed elevation in excess of that of the edge of the dropoff can be expressed as

$$\tilde{\eta}_b = S\tilde{y}. \tag{3–2}$$

Equations (2–20) and (2–21) then take the forms

$$\tilde{u}\frac{\partial\tilde{u}}{\partial\tilde{x}} + \tilde{v}\frac{\partial\tilde{u}}{\partial\tilde{y}} = -g\frac{\partial\tilde{h}}{\partial\tilde{x}} - \frac{\tilde{\tau}_x}{\rho\tilde{h}}, \tag{3–3}$$

$$\tilde{u}\frac{\partial\tilde{v}}{\partial\tilde{x}} + \tilde{v}\frac{\partial\tilde{v}}{\partial\tilde{y}} = -g\frac{\partial\tilde{h}}{\partial\tilde{y}} - gS - \frac{\tilde{\tau}_y}{\rho\tilde{h}}, \tag{3–4}$$

$$\frac{\partial\tilde{u}\tilde{h}}{\partial\tilde{x}} + \frac{\partial\tilde{v}\tilde{h}}{\partial\tilde{y}} = 0. \tag{3–5}$$

Here the Reynolds stress and rainfall are neglected.

Because the flow drops off a vertical edge at the downstream end of the flow domain, the downstream boundary condition can be taken as that of a Froude number of unity. In the present analysis, it suffices to prescribe this boundary condition as

$$\frac{\tilde{u}_n^2}{g\tilde{h}} = 1 \quad \text{at } \tilde{y} = \tilde{a}\cos\tilde{k}\tilde{x}, \tag{3–6}$$

where $\tilde{u}_n$ is the component of velocity normal to the step.

Infinitely far upstream from the step, the flow converges to uniform flow over a constant slope S; that is

$$\tilde{u} = 0,\ \tilde{v} = V_\infty,\ \tilde{h} = H_\infty, \quad \text{at } \tilde{y} = \infty. \tag{3–7a, b, c}$$

Here V_∞ and H_∞ are the velocity and the depth of the uniform flow infinitely far upstream from the step. This flow is taken to be subcritical here.

The following dimensionless parameters are introduced;

$$(\tilde{u}, \tilde{v}) = V_\infty(u', v'), \quad \tilde{h} = H_\infty h, \tag{3–8a, b}$$

$$(\tilde{x}, \tilde{y}, \tilde{a}) = (H_\infty/S)(x, y, a), \quad \tilde{k} = (H_\infty/S)^{-1}k. \tag{3–8c, d}$$

Using the above normalization, the governing equations reduce to

$$F^2\left(u'\frac{\partial u'}{\partial x} + v'\frac{\partial u'}{\partial y} \right) = -\frac{\partial h}{\partial x} - \frac{\sqrt{u'^2 + v'^2}}{h}u', \tag{3–9}$$

$$F^2\left(u'\frac{\partial v'}{\partial x} + v'\frac{\partial v'}{\partial y} \right) = -\frac{\partial h}{\partial y} - 1 - \frac{\sqrt{u'^2 + v'^2}}{h}v', \tag{3–10}$$

$$\frac{\partial u'h}{\partial x} + \frac{\partial v'h}{\partial y} = 0. \tag{3–11}$$

Here the parameter $F = V_\infty/\sqrt{gH_\infty}$ denotes the Froude number of the normal flow far upstream of the edge, which is taken to be less than unity.

It is convenient to employ the following conformal transformation, illustrated in Figure 3–4, in order to analyze the effect of a wavy perturbation to the edge of the dropoff;

$$z = \zeta + iae^{ik\zeta}, \tag{3–12}$$

where $z = x + iy$ and $\zeta = \xi + i\eta$. In real coordinates, the transformation is given as

$$x = \xi - ae^{-k\eta}\sin k\xi, \quad y = \eta + ae^{-k\eta}\cos k\xi. \qquad (3\text{–}13a, b)$$

The Jacobian of the transformation is

$$J = \frac{\partial(x,\ y)}{\partial(\xi,\ \eta)} = 1 - 2ake^{-k\eta}\cos k\xi + (ak)^2 e^{-2k\eta}. \qquad (3\text{–}14)$$

In the limit as the parameter ak approaches unity, the wavy character of the edge devolves into cusps. In the present linear analysis, ak is taken to be very small, in which case the edge shape is well approximated by a simple sinusoidal function. While a more general transformation can in principle be used by adding higher harmonics, (3–14) is sufficiently versatile for most purposes.

The equations of motion written in the transformed plane now take the form

$$F^2\left(\frac{u}{J^{1/2}}\frac{\partial u}{\partial \xi} + \frac{v}{J^{1/2}}\frac{\partial u}{\partial \eta} + \frac{uv}{J}\frac{\partial J^{1/2}}{\partial \eta} - \frac{v^2}{J}\frac{\partial J^{1/2}}{\partial \xi}\right)$$
$$= -\frac{1}{J^{1/2}}\frac{\partial h}{\partial \xi} + \frac{ake^{-k\eta}\sin\ k\xi}{J^{1/2}} - \frac{\sqrt{u^2 + v^2}}{h}u, \qquad (3\text{–}15)$$

$$F^2\left(\frac{u}{J^{1/2}}\frac{\partial v}{\partial \xi} + \frac{v}{J^{1/2}}\frac{\partial v}{\partial \eta} + \frac{uv}{J}\frac{\partial J^{1/2}}{\partial \xi} - \frac{u^2}{J}\frac{\partial J^{1/2}}{\partial \eta}\right)$$
$$= -\frac{1}{J^{1/2}}\frac{\partial h}{\partial \eta} - \frac{1 - ake^{-k\eta}\cos\ k\xi}{J^{1/2}} - \frac{\sqrt{u^2 + v^2}}{h}v, \qquad (3\text{–}16)$$

$$\frac{\partial(J^{1/2}uh)}{\partial \xi} + \frac{\partial(J^{1/2}vh)}{\partial \eta} = 0, \qquad (3\text{–}17)$$

where u and v are the velocities in the ξ and η directions, respectively.

Here dimensionless amplitude a is taken as a small parameter; the following expansions in powers of a are introduced;

$$u = au_1(\xi, \eta) + a^2u_2(\xi, \eta) + \ldots., \tag{3–18a}$$

$$v = -[v_0(\eta) + av_1(\xi, \eta) + a^2v_2(\xi, \eta) + \ldots.], \tag{3–18b}$$

$$h = h_0(\eta) + ah_1(\xi, \eta) + a^2h_2(\xi, \eta) + \ldots.. \tag{3–18c}$$

At leading order, i.e. $O(a^0)$, (3–16) and (3–17) give

$$F^2v_0\frac{dv_0}{d\eta} + \frac{dh_0}{d\eta} = -1 + \frac{v_0^2}{h_0}, \tag{3–19}$$

$$\frac{dv_0h_0}{d\eta} = 0. \tag{3–20}$$

This describes the base flow in the absence of perturbations.

At the next order, $O(a)$, the governing equations give

$$F^2\left(-v_0\frac{\partial u_1}{\partial\eta} - k^2v_0^2e^{-k\eta}\sin k\xi\right) + \frac{\partial h_1}{\partial\xi} = ke^{-k\eta}\sin k\xi - \frac{v_0}{h_0}u_1, \tag{3–21}$$

$$F^2\left(v_0\frac{\partial v_1}{\partial\eta} + v_1\frac{\partial v_0}{\partial\eta} + kv_0\frac{\partial v_0}{\partial\eta}e^{-k\eta}\cos k\xi\right) + \frac{\partial h_1}{\partial\eta} + k\frac{\partial h_0}{\partial\eta}e^{-k\eta}\cos k\xi$$

$$= 2\frac{v_0}{h_0}v_1 - \left(\frac{v_0}{h_0}\right)^2 h_1, \tag{3–22}$$

$$kh_0\frac{\partial u_1}{\partial \xi} - k^2 v_0 h_0 e^{-k\eta}\cos k\xi - h_0\frac{\partial v_1}{\partial \eta} - h_1\frac{\partial v_0}{\partial \eta}$$

$$- v_0\frac{\partial h_1}{\partial \eta} - v_1\frac{\partial h_0}{\partial \eta} + k\frac{\partial v_0 h_0}{\partial \eta}e^{-k\eta}\cos k\xi = 0. \tag{3–23}$$

3.3.2 Zeroth order solution; the base flow

For the subcritical flow considered here, (3–19) and (3–20) describe a simple M2 backwater curve. Since the flow becomes uniform with $v_0 = h_0 = 1$ far upstream of the step, (3–20) can be integrated to yield

$$v_0 h_0 = 1. \tag{3–24}$$

Between (3–19) and (3–24), the following ordinary differential equation for v_0 is obtained:

$$\frac{dv_0}{d\eta} = -\frac{v_0^3 - 1}{v_0^{-2} - F^2 v_0^2}. \tag{3–25}$$

The boundary condition at the downstream end of the domain is the overfall condition of (3–6) as applied to the base flow; in conjunction with (3–24), this yields

$$v_0\Big|_{\eta=0} = F^{-2/3}, \quad h_0\Big|_{\eta=0} = F^{2/3}. \tag{3–26a, b}$$

Equation (3–25) can be integrated directly with (3–26) to yield an M2 backwater curve in implicit form;

$$-\int_{F^{-2/3}}^{v_0} \frac{v_0^{-2} - F^2 v_0}{v_0^3 - 1}\, dv_0 = \eta. \tag{3–27}$$

What is not apparent about this solution, however, is the existence of a singularity in the derivative $dv_0/d\eta$ at $\eta = 0$. Applying the boundary condition (3–26) to the denominator of the right hand side of (3–25) yields the result

$$\frac{dv_0}{d\eta}\Big|_{\eta=0} = -\infty. \tag{3–28}$$

As long as the parameter $F < 1$ is chosen to be order one, it is readily seen that both v_0 and h_0 are also order one on their complete domain of solution. The expansion solution of the form (3–18) sought here, however, will turn out to depend not only on v_0 but also its first derivative. With this in mind, special treatment will be required near the point $\eta = 0$ of singularity

As a prelude to future developments, a simple technique for describing the singularity is presented here. A boundary layer of thickness scaling with some small parameter δ near the overfall is considered. A physical basis for defining the magnitude of δ is considered later. An inner variable η^* near the overfall is defined as

$$\eta^* = \delta^{-1}\eta. \tag{3–29}$$

Substitution of (3–29) into (3–19) and (3–20) yields the relations

$$F^2 v_0 \frac{dv_0}{d\eta^*} + \frac{dh_0}{d\eta^*} = \delta\left(-1 + \frac{v_0^2}{h_0} \right), \tag{3–30}$$

$$\frac{dv_0 h_0}{d\eta^*} = 0. \tag{3–31}$$

The flow velocity v_0 and flow depth h_0 are now expanded in δ as follows;

$$v_0 = F^{-2/3} + \delta^{1/2} v_{01} + \delta v_{02} + \ldots, \tag{3–32a}$$

$$h_0 = F^{2/3} + \delta^{1/2} h_{01} + \delta h_{02} + \ldots. \tag{3–32b}$$

Note that the forms (3–32a, b) automatically satisfy the boundary condition (3–26) as long as

$$v_{0n}\Big|_{\eta^*=0} = 0, \quad n = 1, 2, 3, \ldots, \tag{3–33a}$$

$$h_{0n}\Big|_{\eta^*=0} = 0, \quad n = 1, 2, 3, \ldots. \tag{3–33b}$$

At the lowest non–vanishing order, i.e. $O(\delta^{1/2})$, the streamwise momentum equation (3–30) gives

$$F^{4/3}\frac{dv_{01}}{d\eta^*} + \frac{dh_{01}}{d\eta^*} = 0. \tag{3–34}$$

Integrating (3–34) with the aid of (3–33) yields

$$F^{4/3}v_{01} + h_{01} = 0. \tag{3–35}$$

The continuity equation (3–31) likewise yields at $O(\delta^{1/2})$

$$F^{2/3}\frac{dv_{01}}{d\eta^*} + F^{-2/3}\frac{dh_{01}}{d\eta^*} = 0. \tag{3–36}$$

This equation is integrated to yield (3–35) once again. No further information about v_{01} and h_{01} can be obtained at $O(\delta^{1/2})$.

Progressing to $O(\delta)$, (3–30) and (3–31) yield, respectively,

$$F^{4/3}\frac{dv_{02}}{d\eta^*} + \frac{dh_{02}}{d\eta^*} = -F^2 v_{01}\frac{dv_{01}}{d\eta^*} - 1 + F^{-2}, \tag{3–37}$$

$$F^{2/3}\frac{dv_{02}}{d\eta^*} + F^{-2/3}\frac{dh_{02}}{d\eta^*} = -\frac{d}{d\eta^*}(v_{01}h_{01}). \tag{3–38}$$

If (3–38) is multiplied by $F^{2/3}$, it is seen that the right–hand side of both the above equations are identical. Subtracting one from the other yields a second relation connecting v_{01} and h_{01} in addition to (3–35). Eliminating h_{01}, the following relation for v_{01} is obtained:

$$\frac{3}{2}F^2\frac{dv_{01}^2}{d\eta^*} = F^{-2} - 1. \tag{3–39}$$

Integrating and applying (3–33a), it is found that

$$v_{01} = -G\eta^{*1/2}, \tag{3–40a}$$

where

$$G = \left[\frac{2}{3}F^{-2}(F^{-2}-1)\right]^{1/2}. \tag{3–40b}$$

Likewise, the form for h_{01} is found from (3–40) and (3–35) to be

$$h_{01} = F^{4/3}\,G\eta^{*1/2}. \tag{3–41}$$

The singularity in the derivative of both v_{01} and h_{01} at $\eta^* = 0$ is readily apparent.

Transforming (3–40a) and (3–41) back into the variables v_0, h_0, and η, it is found that near $\eta = 0$

$$v_0 = F^{-2/3} - G\eta^{1/2}, \tag{3–42}$$

$$h_0 = F^{2/3} + F^{4/3}G\eta^{1/2}. \tag{3–43}$$

Considering the derivatives of v_0 and h_0 with respect to η, the above expressions can be expected to be valid as long as δ is chosen to be small compared to G^{-2}.

3.3.3 Reduction of the first order problem

The first order equations (3–21) ~ (3–23) admit solutions of the form

$$u_1 = u_1^{\star}(\eta)\sin k\xi,\ \ v_1 = v_1^{\star}(\eta)\cos k\xi, \qquad (3\text{–}44a, b)$$

$$h_1 = h_1^{\star}(\eta)\cos k\xi. \qquad (3\text{–}44c)$$

Substituting (3–44) into (3–21), (3–22) and (3–23), and reducing with the aid of (3–24) and (3–19), the following equations are obtained:

$$\frac{du_1^{\star}}{d\eta} = \frac{v_0}{F^2}u_1^{\star} - \frac{k}{F^2 v_0}h_1^{\star} - k\left(kv_0 + \frac{1}{F^2 v_0}\right)e^{-k\eta}, \qquad (3\text{–}45)$$

$$\frac{dv_1^{\star}}{d\eta} = \frac{k}{1 - F^2 v_0^3}u_1^{\star} + \frac{F^2 v_0^3 \frac{dv_0}{d\eta} - 2v_0^5 + \frac{dv_0}{d\eta}}{v_0(1 - F^2 v_0^3)}v_1^{\star}$$
$$+ \frac{v_0^6 - v_0\frac{dv_0}{d\eta}}{1 - F^2 v_0^3}h_1^{\star} + k\frac{v_0^5 - v_0^2 - kv_0}{1 - F^2 v_0^3}e^{-k\eta}, \qquad (3\text{–}46)$$

$$\frac{dh_1^{\star}}{d\eta} = -\frac{kF^2 v_0}{1 - F^2 v_0^3}u_1^{\star} - \frac{2F^2\frac{dv_0}{d\eta} - 2v_0^2}{1 - F^2 v_0^3}v_1^{\star}$$
$$- \frac{v_0^4 - F^2 v_0^2\frac{dv_0}{d\eta}}{1 - F^2 v_0^3}h_1^{\star} - k\frac{v_0^3 - 1 - kF^2 v_0^2}{1 - F^2 v_0^3}e^{-k\eta}. \qquad (3\text{–}47)$$

Equations (3–45), (3–46) and (3–47) can be written in compact matrix form as

$$\frac{d\,\underset{\sim}{u}}{d\eta} = \underset{\sim}{\mathscr{L}}(\eta)\,\underset{\sim}{u} + \underset{\sim}{m}(\eta)e^{-k\eta}, \tag{3–48a}$$

where

$$\underset{\sim}{u} = \begin{bmatrix} u_1^\star \\ v_1^\star \\ h_1^\star \end{bmatrix}, \tag{3–48b}$$

$$\underset{\sim}{\mathscr{L}}(\eta) = \begin{bmatrix} L_{11}\, L_{12}\, L_{13} \\ L_{21}\, L_{22}\, L_{23} \\ L_{31}\, L_{32}\, L_{33} \end{bmatrix}, \tag{3–48c}$$

$$L_{11} = \frac{v_0}{F^2},\ L_{12} = 0,\ L_{13} = -\frac{k}{F^2 v_0},\ L_{21} = \frac{k}{1 - F^2 v_0^3},$$

$$L_{22} = \frac{F^2 v_0^3 \frac{dv_0}{d\eta} - 2v_0^5 + \frac{dv_0}{d\eta}}{v_0(1 - F^2 v_0^3)},\ L_{23} = \frac{v_0^6 - v_0\,\frac{dv_0}{d\eta}}{1 - F^2 v_0^3},$$

$$L_{31} = -\frac{kF^2 v_0}{1 - F^2 v_0^3},\ L_{32} = -\frac{2F^2\frac{dv_0}{d\eta} - 2v_0^2}{1 - F^2 v_0^3},$$

$$L_{33} = -\frac{v_0^4 - F^2 v_0^2\,\frac{dv_0}{d\eta}}{1 - F^2 v_0^3},$$

and

$$\mathcal{m}(\eta) = \begin{bmatrix} m_1 \\ m_2 \\ m_3 \end{bmatrix}, \tag{3–48d}$$

$$m_1 = -k\left(kv_0 + \frac{1}{F^2 v_0} \right), \quad m_2 = k\,\frac{v_0^5 - v_0^2 - kv_0}{1 - F^2 v_0^3},$$

$$m_3 = -k\,\frac{v_0^3 - 1 - kF^2 v_0^2}{1 - F^2 v_0^3}.$$

Note that $\mathcal{L}(\eta)$ and $\mathcal{m}(\eta)$ are functions of η via the parameter v_0 and its first derivative.

3.4 Solution

3.4.1 Outer layer, intermediate layer and inner layer.

Before actually solving the problem, it is useful to outline the solution strategy. This strategy is defined in terms of three distinct layers, here called the inner, outer, and intermediate layers

In the region very far upstream of the step, the flow converges to the uniform base flow as described above. Where uniform flow is attained there is a perfect balance between the downslope gravitational force and the resistive force associated with bed shear stress. Here the outer layer is defined to be one in which the deviation from this normal solution is very small. As a result, the equations of motion can be accurately linearized about a constant base state corresponding to uniform flow. This results in a set of ordinary differential equations with constant

coefficients, allowing for a simple closed solution for which the homogeneous part has exponential form.

As shown earlier, the base solution (3–27) possesses a singularity in the derivative at the edge of the overfall, where the Froude number of the flow attains unity. This is a characteristic feature of the M2 curve; in the present coordinate system, $dv_0/d\eta$ attains the value $-\infty$, and $dh_0/d\eta$ attains the value $+\infty$, at $\eta = 0$. This singular behavior carries over to the perturbed flow field. The zone affected by singular behavior is characteristically quite thin. Within it, however, the two–dimensional flow farther upstream simplifies into a one–dimensional flow. This thin layer, scaled with the previously introduced parameter δ, is termed the inner layer in this analysis.

Between the outer and inner layers is an intermediate layer where the inertial, gravitational, resistive, and pressure forces are roughly in balance. The effects of inertia and pressure in particular render the flow interesting, and account for the tendency for the flow to gather toward the indentations.

3.4.2 Solution in the outer layer.

The outer layer is realized as η becomes large. As η approaches infinity, v_0 approaches 1 and $dv_0/d\eta$ approaches 0. In the outer layer, then, the flow is allowed to deviate only slightly from this normal flow. With this assumption, the matrix $\underset{\sim}{\mathscr{L}}$, and vector $\mathscr{m}$, which in general depend upon η, can be approximated by invariant forms, the elements of which are evaluated from (3–48c) at normal flow. Reduction yields

$$\underset{\sim}{\mathcal{L}}^{o} = \begin{bmatrix} \frac{1}{F^2} & 0 & -\frac{k}{F^2} \\ \frac{k}{1-F^2} & -\frac{2}{1-F^2} & \frac{1}{1-F^2} \\ -\frac{kF^2}{1-F^2} & \frac{2}{1-F^2} & -\frac{1}{1-F^2} \end{bmatrix}, \tag{3–49}$$

and

$$\mathcal{m}^{o} = \begin{bmatrix} -\frac{k}{F^2} - k^2 \\ -\frac{k^2}{1-F^2} \\ \frac{k^2F^2}{1-F^2} \end{bmatrix}, \tag{3–50}$$

where the superscript o is used to denote constants and variables in the outer layer.

The differential system (3–48) now reduces to

$$\frac{d\mathcal{u}^{o}}{d\eta} = \underset{\sim}{\mathcal{L}}^{o}\,\mathcal{u}^{o} + \mathcal{m}^{o}e^{-k\eta}. \tag{3–51}$$

Inspection of (3–51) reveals the existence of a forcing term proportional to $e^{-k\eta}$. With this in mind, a solution of the form

$$\mathcal{u}^{o} = \mathcal{u}_{h}(\eta) + \mathcal{u}_{i}e^{-k\eta}, \tag{3–52}$$

is assumed. Here $\mathcal{u}_{h}(\eta)$ and $\mathcal{u}_{i}e^{-k\eta}$ are homogeneous and inhomogeneous solutions

respectively, and $\boldsymbol{u}_i$ is a constant vector. Substituting (3–52) into (3–51), the following relations are obtained;

$$\frac{d\boldsymbol{u}_h}{d\eta} = \underset{\sim}{\mathscr{L}}^0 \boldsymbol{u}_h , \tag{3–53}$$

and

$$[\underset{\sim}{\mathscr{L}}^0 + k\underset{\sim}{\mathscr{I}}]\boldsymbol{u}_i + \boldsymbol{m}^0 = 0, \tag{3–54}$$

where $\underset{\sim}{\mathscr{I}}$ is the identical matrix.

The solutions to (3–53) can now be taken to be of exponential form;

$$\boldsymbol{u}_h = \sum_{n=1}^{3} \boldsymbol{u}_{hn} e^{\lambda_n \eta}, \tag{3–55}$$

where λ_n denote the eigenvalues. The resulting eigenvalue problem is

$$[\underset{\sim}{\mathscr{L}}^0 - \lambda_n \underset{\sim}{\mathscr{I}}]\boldsymbol{u}_{hn} = 0. \tag{3–56}$$

Upon reduction, the solvability condition for (3–56) yields the following cubic characteristic equation for λ_n;

$$F^2(1-F^2)\lambda_n^3 + (4F^2-1)\lambda_n^2 - (3+k^2F^2)\lambda_n + 2k^2 = 0. \tag{3–57}$$

In general, it is found that one of the roots λ_n of (3–57) is always a negative

real number; the other two have positive real parts. It can be seen that $\mathcal{u}^0$ diverges as $\eta \to \infty$ when the real part of λ_n is positive. If the complete solution to first order is to properly converge to normal flow far upstream, it follows that eigenvectors corresponding to eigenvalues which have positive real parts larger than k must vanish. This is equivalent to the application of the following boundary conditions to $v_1^\star$ and $h_1^\star$ in (3–44);

$$v_1^\star(\infty) = h_1^\star(\infty) = 0. \tag{3–58}$$

Now let the single remaining negative real eigenvalue be denoted as λ_1. The corresponding eigenvector is found to have the form

$$\mathcal{u}_{h1} = C_0 \begin{bmatrix} \dfrac{k}{1 - F^2\lambda_1} \\ \dfrac{1 + \lambda_1}{2 - F^2\lambda_1} \\ 1 \end{bmatrix}, \tag{3–59}$$

where C_0 is a free constant.

The inhomogeneous solution $\mathcal{u}_i$ is found from (3–54) to be

$$\mathcal{u}_i = \begin{bmatrix} k \\ 0 \\ 0 \end{bmatrix}. \tag{3–60}$$

The complete solution is thus

$$\mathbf{u}^0 = C_0 \begin{bmatrix} \dfrac{k}{1 - F^2\lambda_1} \\ \dfrac{1 + \lambda_1}{2 - F^2\lambda_1} \\ 1 \end{bmatrix} e^{\lambda_1 \eta} + \begin{bmatrix} k \\ 0 \\ 0 \end{bmatrix} e^{-k\eta}, \qquad (3\text{–}61)$$

in the outer layer. Note that, as expected, $\mathbf{u}^0 \to 0$ as $\eta \to \infty$. A precise definition of the domain in η used to define the outer layer is deferred until later.

3.4.3 Solution in the inner layer

It can be seen from (3–48) that the character of the perturbed solution in general depends on the derivative $dv_0/d\eta$. As noted earlier, however, this parameter displays a singularity at the free overfall located at $\eta = 0$. It is thus impossible to directly integrate (3–48) numerically up to the overfall. To study the behavior of the governing equations near the step, it is necessary to introduce an inner layer which captures the singularity. Here this inner parameter is measured in terms of the scale parameter δ introduced earlier in (3–29).

In the inner layer, then, η is renormalized as

$$\eta^* = \delta^{-1}\eta. \qquad (3\text{–}62)$$

Note that η^* varies from 0 (edge) to 1 as η itself varies from 0 to δ. The governing equations (3–15) ~ (3–17) thus take the form

$$F^2\Big(\delta\frac{u}{J^{1/2}}\frac{\partial u}{\partial\xi}+\frac{v}{J^{1/2}}\frac{\partial u}{\partial\eta^*}+\frac{uv}{J}\frac{\partial J^{1/2}}{\partial\eta^*}-\delta\frac{v^2}{J}\frac{\partial J^{1/2}}{\partial\xi}\Big)$$

$$=-\delta\frac{1}{J^{1/2}}\frac{\partial h}{\partial\xi}+\delta\Big(\frac{ake^{-\delta k\eta^*}\sin k\xi}{J^{1/2}}-\frac{\sqrt{u^2+v^2}}{h}u\Big), \qquad (3\text{–}63)$$

$$F^2\Big(\delta\frac{u}{J^{1/2}}\frac{\partial v}{\partial\xi}+\frac{v}{J^{1/2}}\frac{\partial v}{\partial\eta^*}+\delta\frac{uv}{J}\frac{\partial J^{1/2}}{\partial\xi}-\frac{u^2}{J}\frac{\partial J^{1/2}}{\partial\eta^*}\Big)$$

$$=-\frac{1}{J^{1/2}}\frac{\partial h}{\partial\eta^*}+\delta\Big(-\frac{1-ake^{-\delta k\eta^*}\cos k\xi}{J^{1/2}}-\frac{\sqrt{u^2+v^2}}{h}v\Big), \qquad (3\text{–}64)$$

$$\delta\frac{\partial(J^{1/2}uh)}{\partial\xi}+\frac{\partial(J^{1/2}vh)}{\partial\eta^*}=0, \qquad (3\text{–}65)$$

where

$$J=1-2ak\cos k\xi\,(1-k\delta\eta^*+....)+(ak)^2(1-2k\delta\eta^*+....)$$

$$=1-ak\cos k\xi+(ak)^2+\delta(2ak^2\cos k\xi-2a^2k^3)\eta^*+O(\delta^2). \qquad (3\text{–}66)$$

In analogy to the base flow solution, the higher terms in a in (3–18) may also be expanded in δ as

$$u_1=u_{10}(\xi)+\delta^{1/2}u_{11}(\xi,\eta)+\delta u_{12}(\xi,\eta)+...., \qquad (3\text{–}67a)$$

$$v_1=v_{10}(\xi)+\delta^{1/2}v_{11}(\xi,\eta)+\delta v_{12}(\xi,\eta)+...., \qquad (3\text{–}67b)$$

$$h_1 = h_{10}(\xi) + \delta^{1/2} h_{11}(\xi,\eta) + \delta h_{12}(\xi,\eta) + \ldots., \qquad (3\text{–}67c)$$

.....

Substituting (3–67) into (3–18), u, v, and h are re–expanded to yield

$$u = a u_{10}(\xi) + a\delta^{1/2} u_{11}(\xi,\eta^*) + \ldots., \qquad (3\text{–}68a)$$

$$v = -[\, F^{-2/3} + a v_{10}(\xi) + \delta^{1/2} v_{01}(\eta^*) + a\delta^{1/2} v_{11}(\xi,\eta^*) + \ldots.], \qquad (3\text{–}68b)$$

$$h = F^{2/3} + a h_{10}(\xi) + \delta^{1/2} h_{01}(\eta^*) + a\delta^{1/2} h_{11}(\xi,\eta^*) + \ldots.. \qquad (3\text{–}68c)$$

Note that terms which are of $O(\delta^{1/2})$ or higher in δ describe variations within the inner layer, and are thus taken to vanish at $\eta^* = 0$;

$$u_{mn}\Big|_{\eta^*=0} = v_{mn}\Big|_{\eta^*=0} = h_{mn}\Big|_{\eta^*=0} = 0,$$

$$m = 0, 1, 2, 3, \ldots., n = 1, 2, 3, \ldots.. \qquad (3\text{–}69a, b, c)$$

Terms which are independent of δ need not vanish at $\eta^* = 0$. In light of (3–6) and (3–26), however, the following condition must hold:

$$F^2(F^{-2/3} + \sum_{m=1}^{\infty} a^m v_{m0})^2 = F^{2/3} + \sum_{m=1}^{\infty} a^m h_{m0}. \qquad (3\text{–}70)$$

At order a, for example, (3–70) yields

$$2F^{4/3}v_{10} = h_{10}. \tag{3–71}$$

As noted previously, a condition for the validity of the expansion in δ is that δ be small compared to the order–constant G^{-2}. Here δ is chosen to have the same order as a^2. Substituting (3–68) into (3–63) ~ (3–66), reducing with the aid of (3–69) and (3–71), and dropping terms of $O(a^2)$, $O(a\delta^{1/2})$, $O(\delta)$, and smaller, the following approximate results are obtained.

$$u = au_{10}, \tag{3–72a}$$

$$v = -\left(F^{-2/3} - \delta^{1/2} G\, \eta^{*1/2} + av_{10}(\xi) \right), \tag{3–72b}$$

$$h = F^{2/3} + \delta^{1/2} F^{4/3} G\eta^{*1/2} + 2aF^{4/3}v_{10}(\xi). \tag{3–72c}$$

Here the parameter G is that given in (3–40b). Implicit in the above relations is the result that the terms v_{01} and h_{01} in (3–72) are identical to the corresponding values found for the base solution as (3–42) and (3–43). Note that the parameters u_{10} and v_{10} are both function of ξ only.

As described earlier, the inner solution is to be matched to an intermediate solution of the form of (3–44). With this in mind, u_{01} and v_{01} may be taken to have the following forms:

$$u_{10} = C_1 \sin k\xi, \tag{3–73a}$$

$$v_{10} = C_2 \cos k\xi, \tag{3–73b}$$

where C_1 and C_2 are constants.

In order to facilitate matching of the inner solution with the solution in the intermediate layer, (3–72) is reduced with (3–73) and transformed into the variable δ via (3–62);

$$u = aC_1 \sin k\xi, \tag{3–74a}$$

$$v = -\left(F^{-2/3} - G\eta^{1/2} + aC_2 \cos k\xi + ... \right), \tag{3–74b}$$

$$h = F^{2/3} + F^{4/3}G\eta^{1/2} + 2aF^{4/3}C_2 \cos k\xi + ... \tag{3–74c}$$

Matching is then performed at $\eta = \delta$, i.e. $\eta^* = 1$. The following matching condition is obtained for the base flow:

$$v_0|_{\eta=\delta} = F^{-2/3} - \delta^{1/2}G, \tag{3–75a}$$

$$h_0|_{\eta=\delta} = F^{2/3} + F^{4/3}\delta^{1/2}G. \tag{3–75b}$$

At O(a), the following matching conditions are obtained:

$$u_1^\star|_{\eta=\delta} = C_1, \tag{3–76a}$$

$$v_1^\star|_{\eta=\delta} = C_2, \tag{3–76b}$$

$$h_1^\star|_{\eta=\delta} = 2F^{4/3}C_2, \tag{3–76c}$$

or in compact matrix form,

$$\mathcal{A}^{i} = \begin{bmatrix} C_1 \\ C_2 \\ 2F^{4/3}C_2 \end{bmatrix} \text{ at } \eta = \delta. \tag{3–77}$$

3.4.4 Solutions in intermediate layer.

The solution for v_0 can be evaluated numerically by integrating (3–25) upstream from the point $\eta = \delta$ using the Runge–Kutta method. The required boundary condition is (3–75a). The form of (3–25) insures that v_0 converges to unity far upstream. The point η_i defining the interface between the outer and intermediate layer can then be defined such that v_0 is sufficiently close to unity.

The full differential system (3–48) is then solved numerically in the intermediate layer. The outer solution contains the one free constant C_0, which provides the basis for a shooting method. A guess for the value of C_0 is made; the Runge–Kutta method is then used to step the solution downstream of the point η_i of matching with the outer solution. At the point $\eta = \delta$, matching with the inner solution is tested. In particular, the parameters C_1, C_2, and C_3 are estimated as

$$C_1 = u_1^{\star}(\eta, C_0)\big|_{\eta=\delta}, \tag{3–78a}$$

$$C_2 = v_1^{\star}(\eta, C_0)\big|_{\eta=\delta}, \tag{3–78b}$$

$$C_3 = h_1^{\star}(\eta, C_0)\big|_{\eta=\delta}. \tag{3–78c}$$

Note the indicated functional dependence of the solution on the guess for C_0 in the above relations. According to (3–76c), correct matching and evaluation of the constants C_0, C_1, and C_2 is obtained if

$$C_3 = 2F^{4/3}C_2. \tag{3–79}$$

A Newton–Raphson technique is used to improve the successive guesses for C_0. The method is continued until all three unknown constants C_0, C_1, and C_2 are successfully evaluated.

3.5 Stability analysis

In Figure 3–5, the parameters $u_1^\star(\eta)$, $v_1^\star(\eta)$, and $h_1^\star(\eta)$ are shown as functions of η for the case F = 0.5, k = 4. These parameters can be interpreted as the velocities and depth along a line extending upstream from the center of an indentation such as that illustrated in Figure 3–2. Far upstream of the step, it is seen that $u_1^\star$ increases and $h_1^\star$ decreases in the direction of the step. Because inertial effects are still small in this region, the discharge per unit width remains constant. Near the edge of the dropoff, however, inertial effects cause $h_1^\star$ to increase in order to satisfy the boundary condition at the step.

In Figure 3–6, a complete velocity field is illustrated over one transverse wavelength. It is seen that as the step is approached, the velocity vectors are deflected toward the indentation. At the edge of the step, the velocity at the center of an indentation is seen to be larger than that at the center of a protuberance.

The flow velocities and depth at the step ($\eta = 0$) are seen from (3–74) to be

given to linear order in a by the relations

$$u = aC_1 \sin k\xi, \tag{3–80a}$$

$$v = -(F^{-2/3} + aC_2 \cos k\xi), \tag{3–80b}$$

$$h = F^{2/3} + 2aF^{4/3}C_2 \cos k\xi. \tag{3–80c}$$

In the present analysis, the gradual retreat of a free overfall (waterfall) is considered. As mentioned in 3.2, erosion is caused by the impact of the falling water. Therefore, it is resonable that the retreat speed $\tilde{c}_r$ is assumed to be an increasing function of discharge per unit width, $\tilde{q}$; that is

$$\tilde{c}_r = f_e(\tilde{q}_e). \tag{3–81}$$

Here $\tilde{q}_e$ denotes the value of $\tilde{q}$ evaluated at the upstream edge of the overfall. The implication is that larger amounts of discharge at the downstream edge result in higher velocities of retreat of the overfall.

Equation (3–81) can always be expanded in power form about some reference edge discharge $\tilde{q}_r$, i.e.

$$\tilde{c}_r = b\tilde{q}_e^{\,N}, \tag{3–82a}$$

where

$$N \equiv \frac{\tilde{q}_e}{f_e}\frac{df_e}{d\tilde{q}_e}\bigg|_{\tilde{q}_e=\tilde{q}_r} ; \quad b \equiv f_e(\tilde{q}_r)\,\tilde{q}_r^{-N}. \qquad (3\text{–}82b, c)$$

The condition that the overfall retreat more rapidly with increasing discharge places the condition that b and N must be positive. Precise values are not specified in the present linear analysis.

Between (3–82) and (3–80), the (dimensioned) magnitude of the discharge per unit width $\tilde{q}_e$ at the overfall edge is seen to be given to linear order in amplitude a by the relation

$$\tilde{q}_e = V_\infty H_\infty (1 + 3aF^{2/3}C_2 \cos k\xi). \qquad (3\text{–}83)$$

It is assumed that the elevated discharge due to the concentration of flow under an indentation is responsible for the initiation of a channel. Here a very simple stability analysis is performed to obtain a first estimate of the distance between initial channels, and thus incipient drainage basins, as illustrated in Figure 3–3. The relation (3–82) is postulated as the governing relation for magnitude of the upstream migration speed.

The direction of upstream migration is taken to be perpendicular to the overfall edge. Note that the overfall serves as the origin of the η coordinate in Figure 3–4. Let the distance $\tilde{Y}_e(\tilde{x}, \tilde{t})$ denote the distance of the overfall in the y direction from some fixed line, as shown in Figure 3–7. As seen in Figure 3–1, the mean line of the overfall corresponds to the origin of the y coordinate. The distance from the fixed line of Figure 3–7 to this mean line is taken to be $\tilde{Y}_0(\tilde{t})$, such that

$$\tilde{Y}_e(\tilde{x}, \tilde{t}) = \tilde{Y}_0(\tilde{t}) + \tilde{y}_e(\tilde{x}, \tilde{t}), \tag{3–84}$$

where $\tilde{y}_e(\tilde{x}, \tilde{t})$ denotes the location of the edge of the overfall in the $\tilde{x}$–$\tilde{y}$ coordinate system of Figure 3–1.

The geometric relation connecting the speed of retreat $\tilde{c}_r$ and the distance $\tilde{Y}_e$ is illustrated in Figure 3–8; it can be stated as

$$\frac{1}{\left[1 + \left(\frac{\partial \tilde{Y}_e}{\partial \tilde{x}}\right)^2\right]^{1/2}} \frac{\partial \tilde{Y}_e}{\partial \tilde{t}} = \tilde{c}_r. \tag{3–85}$$

The parameters $\tilde{Y}_e$, $\tilde{Y}_0$, and $\tilde{y}_e$ can be reduced to the corresponding nondimensional forms Y_e, Y_0, and y_e using the length scale $H_\infty S^{-1}$ of (3–8), and the velocity scale V_∞ can be used to reduce $\tilde{c}_r$ to the dimensionless form c_r. Using (3–84) and (3–85) the following dimensionless form is obtained;

$$\frac{1}{[1 + (\frac{\partial y_e}{\partial x})^2]^{1/2}} (\dot{Y}_0 + \frac{\partial y_e}{\partial t}) = c_r. \tag{3–86}$$

Here the superscript $\dot{}$ denotes the ordinary derivative with respect to t.

The above relation is now linearized. Evaluating (3–13) at the overfall edge ($\eta = 0$) and reducing for small amplitude a, the following results are obtained;

$$y_e(x,t) = a \cos kx \; ; \quad x = \xi. \tag{3–87}$$

Between (3–82), (3–83), (3–84), (3–85), (3–87) and the appropriate

transformations between dimensioned and dimensionless, (3–86) can be reduced to the following forms. At $O(a^0)$, the base rate of retreat is given by

$$\dot{Y}_0 = c_{r0}, \tag{3–88a}$$

where

$$c_{r0} = \frac{1}{V_\infty} b \tilde{q}_{e0}^{N}; \quad \tilde{q}_{eo} = \rho C_f V_\infty^2 F^{-4/3}. \tag{3–88b,c}$$

At $O(a)$, it is found that

$$\frac{\partial y_e}{\partial t} = 3aNc_{r0}C_2F^{2/3}\cos kx. \tag{3–89}$$

It is now possible to perform a linear stability analysis of the overfall retreat. Equations (3–87) and (3–89) reduce to

$$\frac{da}{dt} = 3Nc_{r0}F^{2/3}C_2a. \tag{3–90}$$

The above equations has exponential solutions of the form

$$a = a_0 e^{\omega t}, \tag{3–91a}$$

where

$$\omega = 3Nc_{r0}F^{2/3}C_2(k). \tag{3–91b}$$

Note that only C_2 depends on wavenumber k in (3–91b).

In the above relation, the parameters N, c_{r0}, and F can all be taken as positive. It follows that $\omega > 0$, and instability results, if C_2 is positive. An examination of (3–80) and (3–83) confirms that a positive value of C_2 corresponds to a gathering of flow toward the indentations.

The functional dependence of C_2 versus wavenumber k is described in Figure 3–9 for several values of Froude number F. It is found that the parameter C_2 is positive for all values of k for which calculations were performed. It appears to go to infinity with k. This implies that downstream end is always unstable and maximum instability appears for infinitely large value of k. The predictions of Figure 3–9 provide an estimate of the wavelength between incipient drainage basins predicted by the present analysis. Between (3–8d) and the relation

$$\tilde{\lambda} = \frac{2\pi}{\tilde{k}}, \tag{3–92}$$

the following result is obtained for characteristic basin spacing $\tilde{\lambda}_c$:

$$\tilde{\lambda}_c = 2\pi H_\infty S^{-1} k_c^{-1} . \tag{3–93}$$

Here k_c is the characteristic wavenumber which maximizes $C_2(k)$. According to the relation (3–93), Figure 3–9 also shows that the characteristic basin spacing $\tilde{\lambda}_c$ is infinitely small.

It is concluded that the charcteristic basin spacing cannot be obtained from the stability analysis using the foot step erosion model proposed in this chapter.

3.6 Conclusion

A theoretical model is presented to explain the process of drainage basin inception on plateau composed of cohesive soil using the simple assumption of "step foot erosion".

The velocity distribution and water surface profile on a plateau which has a sinuous step at the downstream end are obtained theoretically using perturbation techniques.

It is found that flow is gathered to and intensified at indentations, and that the intensification is maximized when the wavelength of the perturbation is infinitesimally small. It is concluded that the process of drainage basin inception cannot be explained by means of the "step foot erosion" model, in which bed shear stress is assumed to be below critical everywhere on the plateau, and with erosion only at the foot of the step.

The problem of drainage basin inception is approached from different point of view in Chapters 4 and 5.

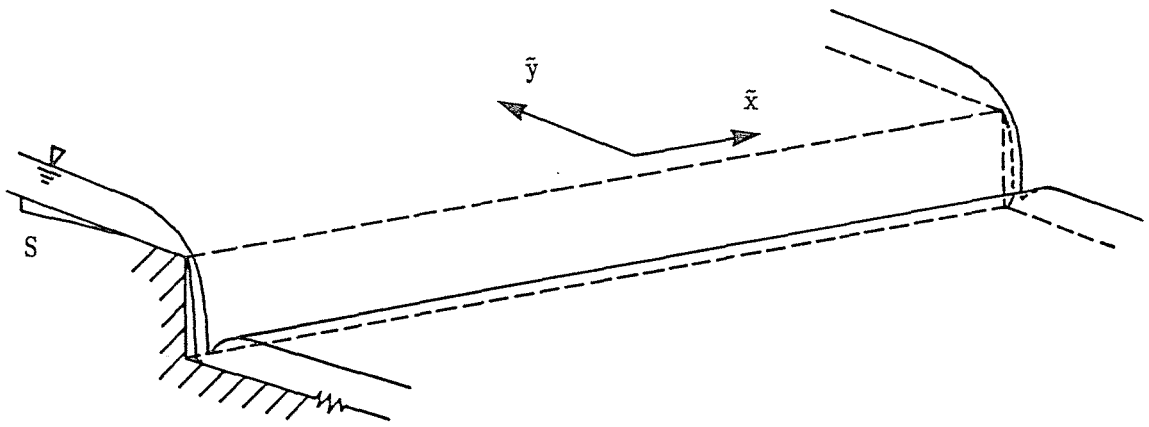

Figure 3–1. Schematic diagram showing a plateau with a step. Flow is in the negative y direction.

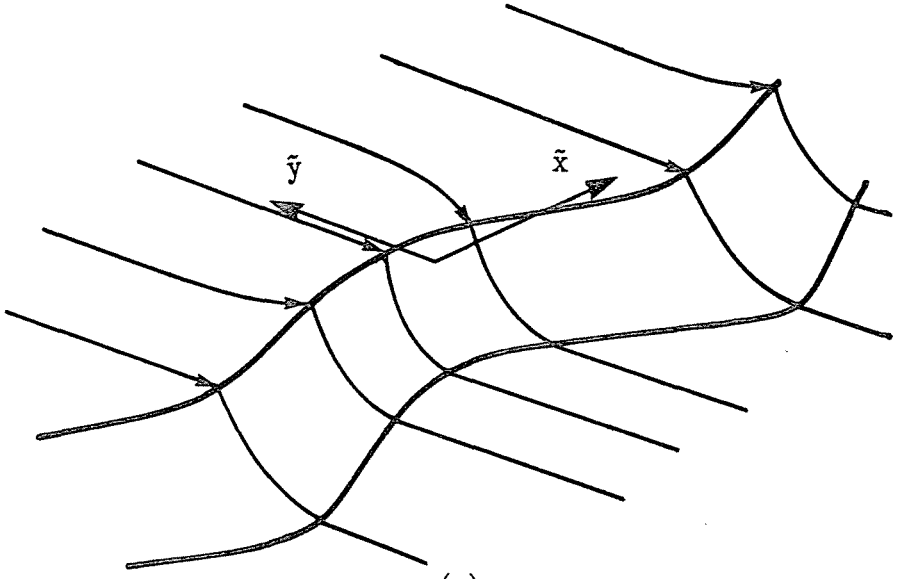

(a)

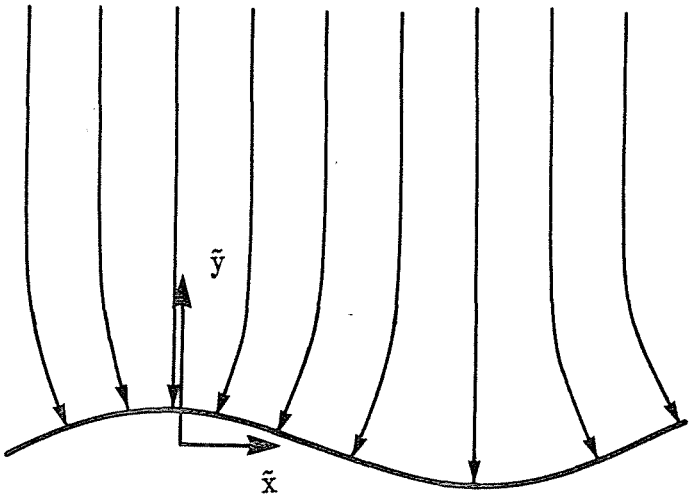

(b)

Figure 3–2. Schematic diagram showing the backwater–driven tendency for flow to concentrate in the indentations of a sinuous step bounding a plateau.

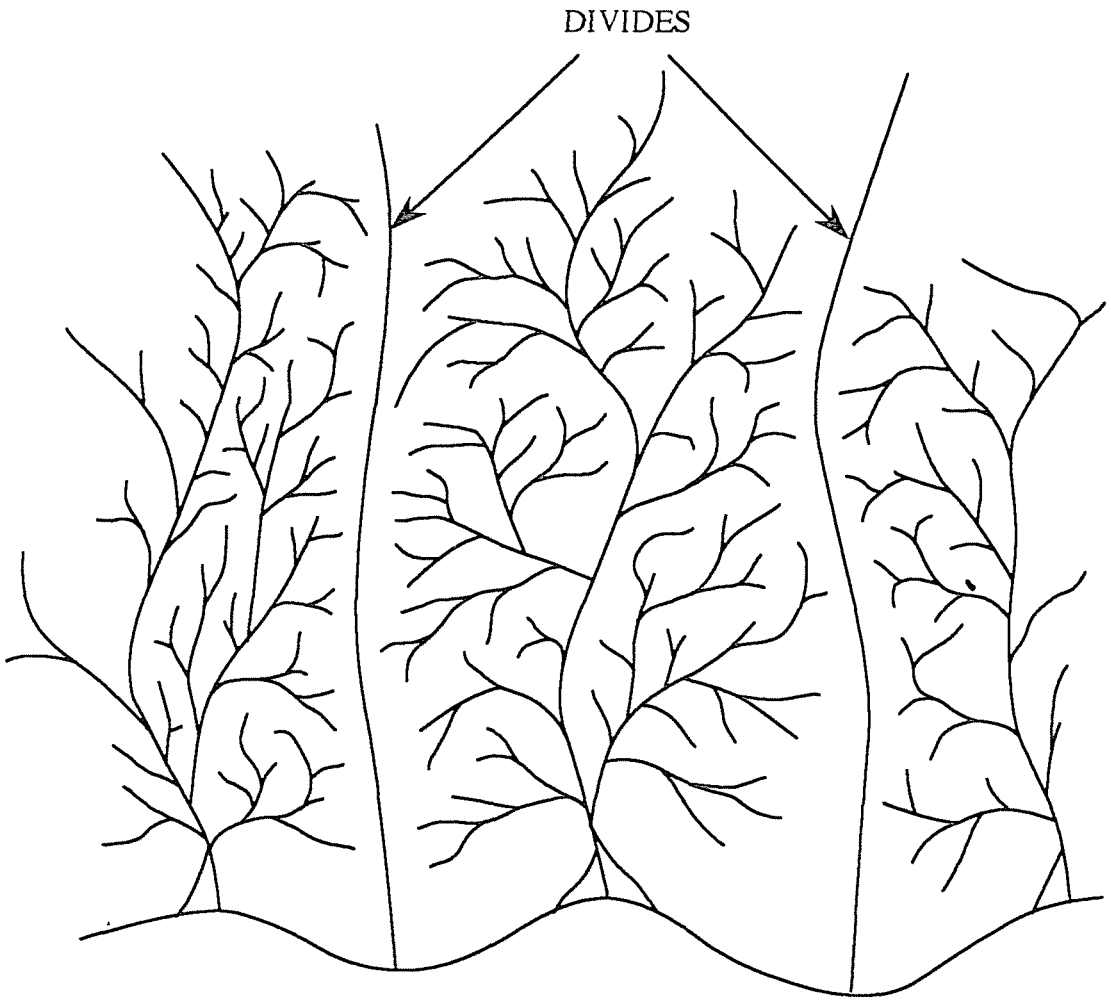

Figure 3–3. Schematic diagram of the resulting system of basins.

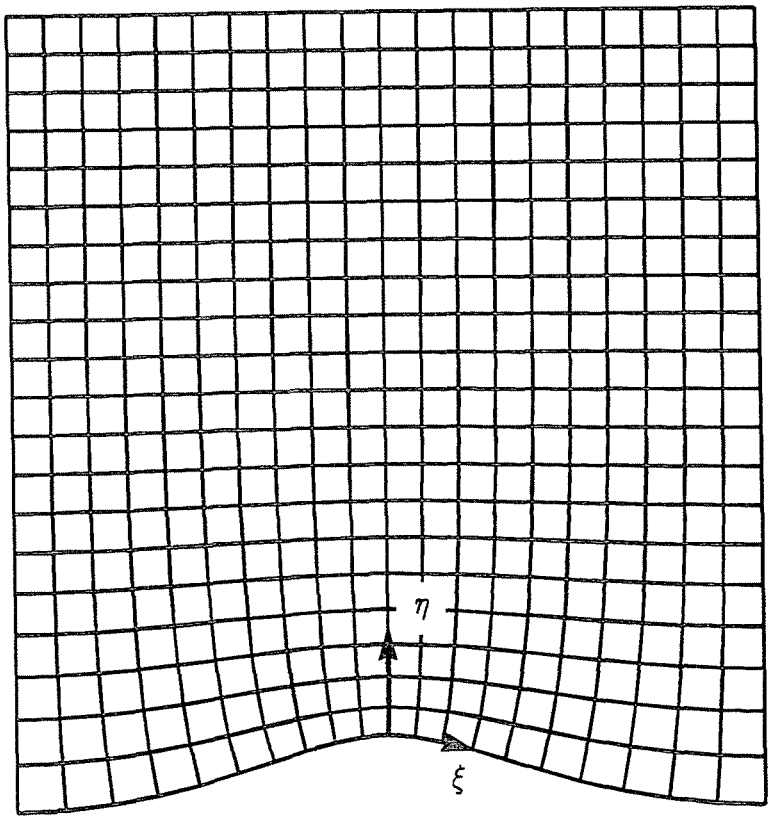

Figure 3–4. Conformal transformation defined by (3–12) in which ak = 0.3.

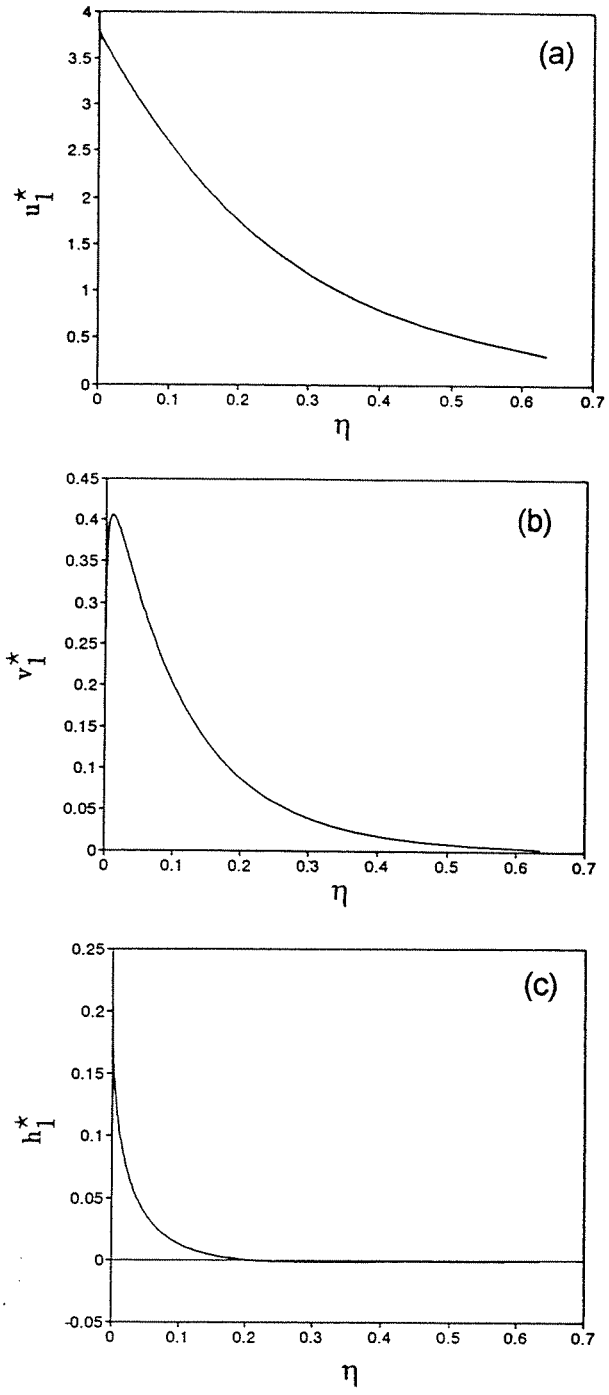

Figure 3–5. Velocity and depth profiles for the case F = 0.5 and k = 4. (a) $u_1^\star$, (b) $v_1^\star$, (c) $h_1^\star$.

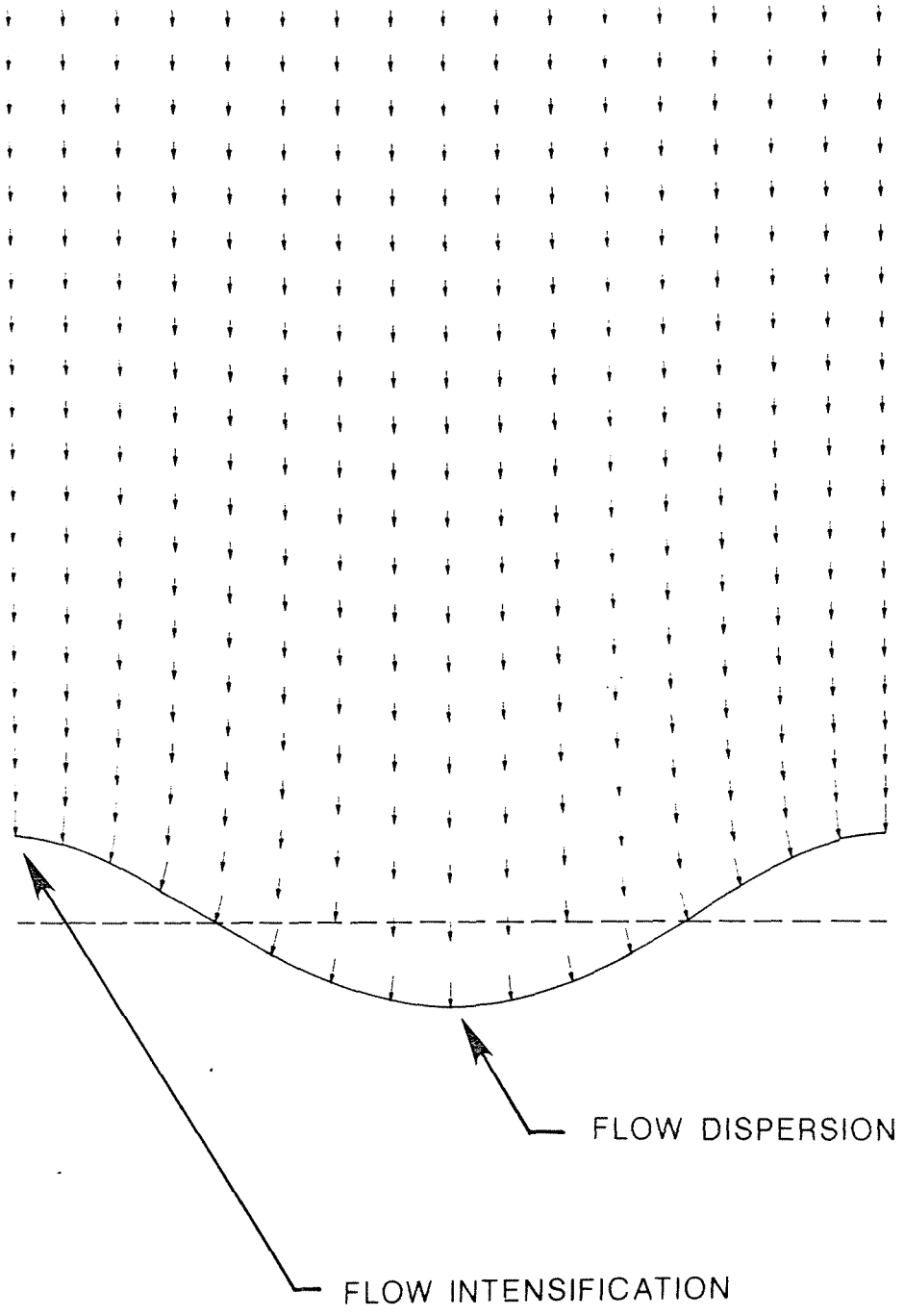

Figure 3–6. Velocity vectors near the step on the plateau for the case F = 0.5, k = 4 and a = 0.025.

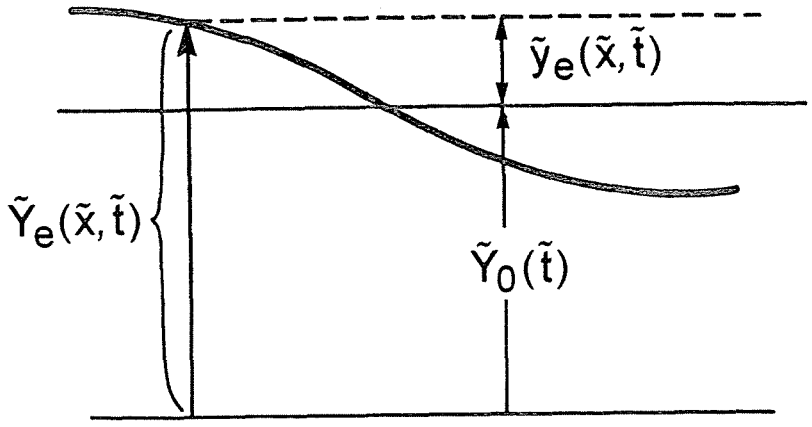

Figure 3–7. Definition diagram showing the parameters $\tilde{Y}_e$, $\tilde{Y}_0$, and $\tilde{y}_e$.

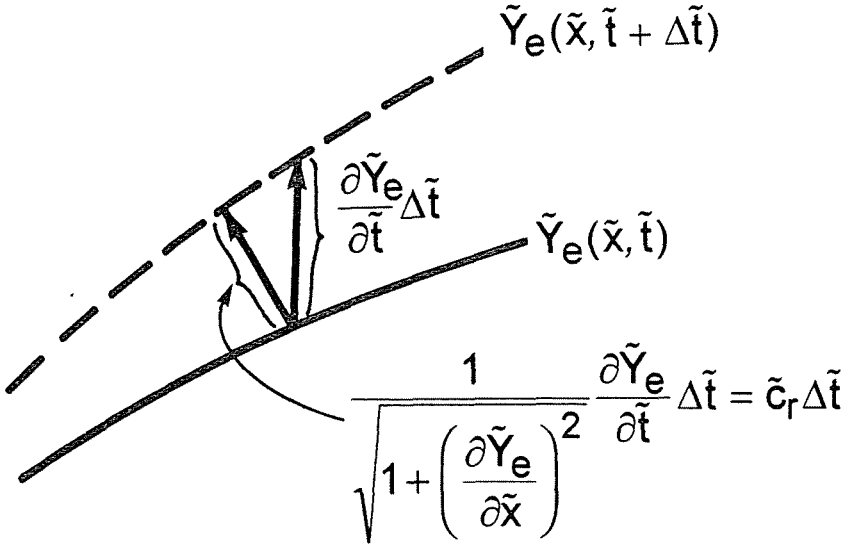

Figure 3–8. Definition diagram showing the relation between $\tilde{c}_r$ and $\tilde{Y}$.

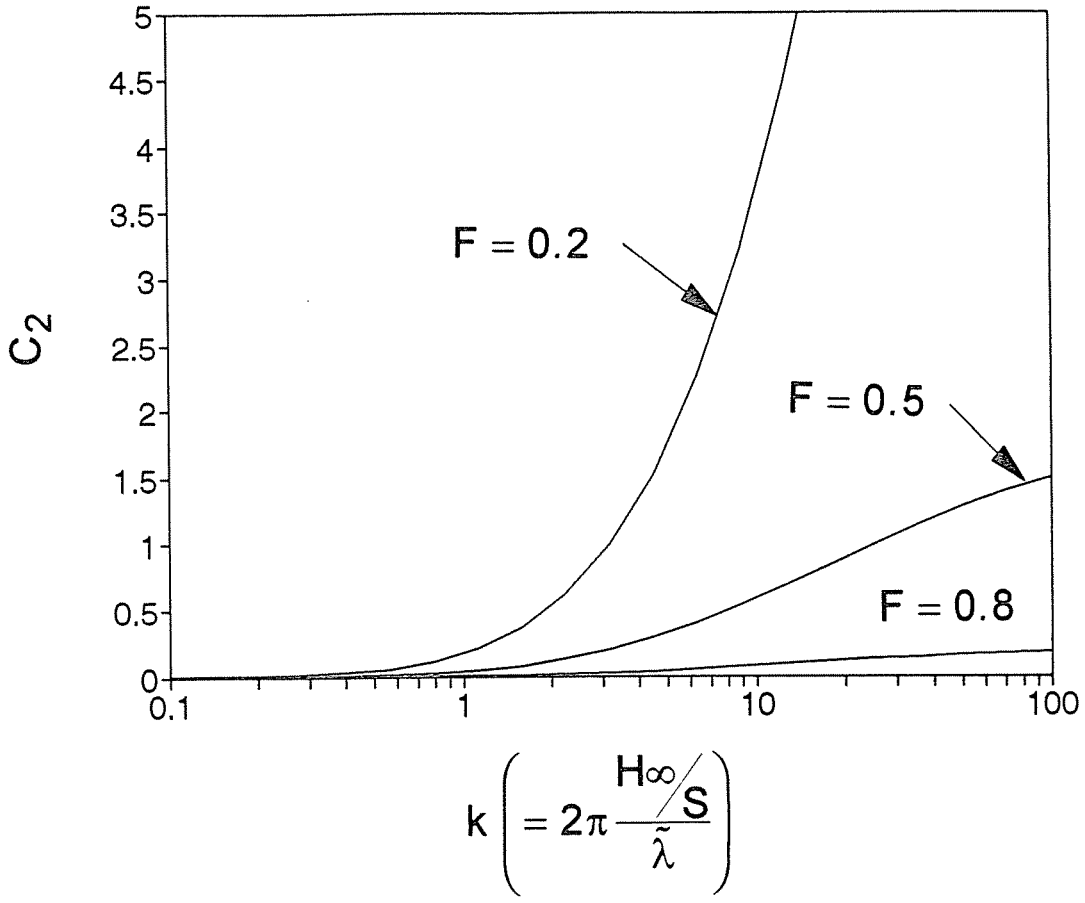

Figure 3–9. Flow intensification C_2 versus wavenumber k and the Froude number F.

4. UPSTREAM–DRIVEN DRAINAGE BASIN INCEPTION USING A THRESHOLD HYPOTHESIS

4.1 Introduction

In Chapter 3, a theoretical model of drainage basin inception was proposed. This model was based on classical linear stability analysis; it resulted in the achievement of maximum perturbation growth rate at infinitely large wavenumbers. This implies that the characteristic wavelength is infinitesimally small. The "step foot erosion model" thus fails to satisfactorily explain the processes of drainage basin inception. This may be because the assumption made in Chapter 3 is not generally valid. According to the assumption of the "step foot erosion model", erosion resulting in channel inception occurs only at the foot of the step. This is reasonable only when the water discharge is limited in a certain special range, in which falling water has enough energy to give rise to erosion right under the step, but the shear stress on the plateau itself is nowhere large enough to cause bed erosion. If the discharge exceeds this range, however, erosion occurs on the surface of the plateau. The analysis is thus extended to cases in which erosion occurs not only right under the step but also on the surface of the plateau.

As an alternative to stability analysis, a new "threshold model" is proposed. This is based on the threshold arguments of Montgomery and Dietrich (1989). One of their thresholds consists of a critical shear stress generated by an overland flow sufficient to erode the bed and thus initiate channel formation.

4.2 Conceptual model

Fig. 4–1 shows a plateau composed of cohesive material which is flat, but which has a slight slope S in the $\tilde{y}$ direction. A uniform rainfall is assumed over the entire plateau. If the upstream edge is taken as the origin and the downstream direction as the positive $\tilde{y}$ direction, the water discharge of the surface flow increases linearly in $\tilde{y}$ as a result of rainfall. At the same time, the bed shear stress increases in the downstream direction, eventually reaching the threshold value for bed erosion at some point on the plateau. If the plateau is completely flat, the threshold points form a straight line parallel to the $\tilde{x}$ direction, downstream of which erosion starts to occur. The surface of a plateau in nature can never be expected, however, to be perfectly flat. Rather it always includes a component of irregularity. This irregularity can be described by the superposition of Fourier modes with various wavenumbers. At the linear level, the flow on an irregular surface can also be expressed in terms of superposition of flows on sinuous surfaces with various wavenumbers. With this in mind, the flow field on a sinuous surface of specified wavenumber is considered.

Let the surface of the plateau be flat but tilted with mild slope S in the $\tilde{y}$ (streamwise) direction; to this add a small transverse sinusoidal perturbation of amplitude $\tilde{a}$. The resulting bed surface is given by

$$\tilde{\eta}_b = -S\tilde{y} - \tilde{a}\cos\tilde{k}\tilde{x}, \qquad (4\text{–}1)$$

as shown in Figure 4–2. Here $\tilde{\eta}_b$ is taken to be zero at $\tilde{y} = 0$, i.e. the divide, in the unperturbed state.

Consider first the case of a constant downslope discharge per unit width supplied along the divide, in the absence of rainfall. As it flows downslope, water

tends to gather in the troughs. The velocity of the resulting overland flow can be expected to be larger in the troughs than over the ridges, because flow velocity is roughly proportional to square root of the corresponding depth. It will be shown that this flow concentration due to this topographical effect has no dependency on the wavenumber k.

Suppose, however, that a steady, uniform rainfall is provided everywhere over the surface. It will be shown that this uniform rainfall accelerates flow in troughs more strongly than over ridges. This drives an enhanced lateral flow from ridges to troughs in accordance with the condition of water continuity. This effect is stronger for shorter wavelengths. If it were not for backwater effects, flow would be continuously concentrated toward the center of troughs, resulting in infinite concentration of flow in the troughs. Transverse backwater effects, however, yield a net force from trough to ridge, so preventing the overconcentration of flow. As wavelength k becomes small, the transverse Reynolds stress acts to reduce the flow concentration at troughs. A combination of all these effects results in the maximization of flow concentration at some finite wavelength.

Near the value of k associated with maximum flow concentration, the locus of threshold shear stress does not form a straight line in the transverse ($\tilde{x}$) direction. In troughs, where velocity is intensified, the flow reaches the threshold condition in a shorter distance downstream of the divide than over the ridges as shown in Figure 4–2. This can be expected to result in a preferential tendency for channelization along the troughs, a tendency that would be magnified farther downstream. Once channels are formed on the plateau surface, each channel can gather more and more water and grow rapidly, thus preventing other channels from being formed nearby (Figure 4–3). Following this scenario, channels the heads of which form in the

shortest distance downstream of the divide should dominate during the initial stage of channel formation. It is therefore hypothesized that the wavelength which minimizes the distance from the divide to the point at which the threshold condition is reached in a trough is taken to be the characteristic spacing of the incipient basin.

As revealed later, the flow considered here does not have to be subcritical in the Froude sense, a feature that distinguishes the analysis from that in Chapter 3.

4.3 Formulation

4.3.1 Governing relations

In accordance with Figure 4–1, it is assumed that the plateau has a slight slope S descending in the positive $\tilde{y}$ direction. Perturbed bed elevation is expressed by (4–1). Equations (2–20) and (2–21) then take the forms

$$\tilde{u}\frac{\partial\tilde{u}}{\partial\tilde{x}} + \tilde{v}\frac{\partial\tilde{u}}{\partial\tilde{y}} = -g\frac{\partial\tilde{h}}{\partial\tilde{x}} - g\tilde{a}\tilde{k}\sin\tilde{k}\tilde{x} - \frac{C_f\sqrt{\tilde{u}^2+\tilde{v}^2}}{\tilde{h}}\tilde{u} + \frac{\partial}{\partial\tilde{x}}(\nu_t\frac{\partial\tilde{u}}{\partial\tilde{x}}) + \frac{\partial}{\partial\tilde{y}}(\nu_t\frac{\partial\tilde{u}}{\partial\tilde{y}}), \tag{4–2}$$

$$\tilde{u}\frac{\partial\tilde{v}}{\partial\tilde{x}} + \tilde{v}\frac{\partial\tilde{v}}{\partial\tilde{y}} = -g\frac{\partial\tilde{h}}{\partial\tilde{y}} + gS - \frac{C_f\sqrt{\tilde{u}^2+\tilde{v}^2}}{\tilde{h}}\tilde{v} + \frac{\partial}{\partial\tilde{x}}(\nu_t\frac{\partial\tilde{v}}{\partial\tilde{x}}) + \frac{\partial}{\partial\tilde{y}}(\nu_t\frac{\partial\tilde{v}}{\partial\tilde{y}}), \tag{4–3}$$

$$\frac{\partial\tilde{u}\tilde{h}}{\partial\tilde{x}} + \frac{\partial\tilde{v}\tilde{h}}{\partial\tilde{y}} = I, \tag{4–4}$$

where I is rainfall intensity (volume per unit bed area per unit time).

4.3.2 Base flow solution; base–normal flow

If there is no perturbation on the bed surface, equations (4–2), (4–3) and (4–4) reduce to

$$\tilde{v}\frac{d\tilde{v}}{d\tilde{y}} = -g\frac{d\tilde{h}}{d\tilde{y}} + gS - \frac{C_f\tilde{v}^2}{\tilde{h}} + \frac{d}{d\tilde{y}}(\nu_t\frac{d\tilde{v}}{d\tilde{y}}), \tag{4–5}$$

$$\frac{d\tilde{v}\tilde{h}}{d\tilde{y}} = I. \tag{4–6}$$

A boundary condition on these equations is that there be no flow beyond the divide; that is,

$$\tilde{v}\tilde{h} = 0 \quad \text{at } \tilde{y} = 0. \tag{4–7}$$

A solution to these equations defines the base flow, which is to be perturbed according to (4–1).

There is a simple version of this base flow, however, that turns out to be an accurate approximation everywhere except in a thin region near the divide, i.e. $\tilde{y} = 0$. It is obtained by neglecting the backwater and turbulent diffusion terms (4–5), yielding the force balance characteristic of normal (equilibrium) overland flow:

$$gS - \frac{C_f \tilde{v}^2}{\tilde{h}} = 0. \tag{4–8}$$

The flow solution obtained from (4–6) and (4–7) is herein called the base–normal flow.

This base–normal flow can be solved as follows. Equation (4–6) is integrated with (4–7) to yield

$$\tilde{v}\tilde{h} = I\tilde{y}. \tag{4–9}$$

Equations (4–7) and (4–9) then give solutions of the form

$$\tilde{v} = \left(\frac{gSI}{C_f} \right)^{\frac{1}{3}} \tilde{y}^{\frac{1}{3}}, \quad \tilde{h} = \left(\frac{C_f I^2}{gS} \right)^{\frac{1}{3}} \tilde{y}^{\frac{2}{3}}. \tag{4–10, 11}$$

That is, velocity and depth are proportional to $\tilde{y}^{\frac{1}{3}}$ and $\tilde{y}^{\frac{2}{3}}$, respectively.

It is now useful to back–calculate the order of magnitude of the terms neglected in going from (4–5) to (4–8). The backwater terms in (4–5) are estimated using the solutions (4–10) and (4–11) as follows:

$$\tilde{v}\frac{\partial \tilde{v}}{\partial \tilde{y}} + g\frac{\partial \tilde{h}}{\partial \tilde{y}} \simeq (gI)^{\frac{2}{3}} \left[\left(\frac{S}{C_f} \right)^{\frac{2}{3}} + \left(\frac{C_f}{S} \right)^{\frac{2}{3}} \right] \tilde{y}^{-\frac{1}{3}}. \tag{4–12}$$

The streamwise Reynolds stress term is similarly estimated as

$$\nu_t \frac{\partial^2 \tilde{v}}{\partial \tilde{y}^2} \simeq -\frac{2}{9} \nu_t \left(\frac{gSI}{C_f} \right)^{\frac{1}{3}} \tilde{y}^{-\frac{5}{3}}. \tag{4–13}$$

The eddy viscosity ν_t is assumed to take the form

$$\nu_t = \alpha \tilde{u}^* \tilde{h}, \tag{4–14}$$

where $\tilde{u}^*$ and denotes the friction velocity of the surface flow. Recalling that $\tilde{u}^* = \sqrt{C_f}\tilde{v}$, the use of (4–9) and (4–14) yields the result

$$\nu_t = \alpha \sqrt{C_f} \tilde{v} \tilde{h} = \alpha \sqrt{C_f} I \tilde{y}. \tag{4–15}$$

Then (4–13) yields

$$\nu_t \frac{\partial^2 \tilde{v}}{\partial \tilde{y}^2} \simeq -\frac{2}{9} \alpha \sqrt{C_f} I \left(\frac{gSI}{C_f} \right)^{\frac{1}{3}} \tilde{y}^{-\frac{2}{3}}. \tag{4–16}$$

Comparing the estimates (4–12) and (4–16) with the original force balance of the base flow (4–5), it is seen that the ratio of backwater terms to the gravitational term varies as $\tilde{y}^{-1/3}$, and the rate of the streamwise Reynolds stress term to the gravitational term varies as $\tilde{y}^{-2/3}$. Since the force balance of the base–normal flow of (4–8) is between gravity and friction, the indication is that the backwater and Reynolds stress terms of the base flow become negligible sufficiently far downstream. This conclusion is put on a more formal basis below.

4.3.3 Normalizations

Let the distance from the divide $\tilde{y}$ at which the threshold bed shear stress $\tilde{\tau}_c$ for bed erosion is first attained by the base–normal flow be given by L_{th}. The shear stress itself is given by the relation

$$\tilde{\tau}_{th} = \rho C_f V_{th}^2, \tag{4–17a}$$

where V_{th} denotes the flow velocity of the base–normal flow at $\tilde{y} = L_{th}$, the depth there is likewise defined to be H_{th}. Mass conservation of water ensures that

$$V_{th} H_{th} = I L_{th}. \tag{4–17b}$$

Equation (4–10) applied to (4–17b) yields the result

$$L_{th} = \frac{C_f}{gSI} V_{th}^3. \tag{4–17c}$$

The following normalizations allow for a dimensionless treatment:

$$(\tilde{u}, \tilde{v}) = V_{th}(u, v), \ (\tilde{a}, \tilde{h}) = H_{th}(a, h), \tag{4–18a,b}$$

$$\tilde{x} = (H_{th}/S)x, \ (\tilde{y}, \tilde{\ell}) = L_{th}(y, \ell), \tag{4–18c,d}$$

$$\tilde{k} = (H_{th}/S)^{-1} k. \tag{4–18e}$$

where $\tilde{\ell}$ is the distance of the threshold point downstream of the divide. Note that

according to the base–normal solution, $\ell = 1$. The normalized governing equations thus take the form

$$F^2\left(u\frac{\partial u}{\partial x} + \psi v\frac{\partial u}{\partial y} \right) = -\frac{\partial h}{\partial x} - ak \sin kx - \frac{\sqrt{u^2+v^2}}{h}\, u$$

$$+ \epsilon\left[\frac{\partial}{\partial x}\left(\sqrt{u^2+v^2}\, h\frac{\partial u}{\partial x}\right) + \psi^2\frac{\partial}{\partial y}\left(\sqrt{u^2+v^2}\, h\frac{\partial u}{\partial y}\right) \right], \qquad (4\text{–}19)$$

$$F^2\left(u\frac{\partial v}{\partial x} + \psi v\frac{\partial v}{\partial y} \right) = -\psi\frac{\partial h}{\partial y} + 1 - \frac{\sqrt{u^2+v^2}}{h}\, v$$

$$+ \epsilon\left[\frac{\partial}{\partial x}\left(\sqrt{u^2+v^2}\, h\frac{\partial v}{\partial x}\right) + \psi^2\frac{\partial}{\partial y}\left(\sqrt{u^2+v^2}\, h\frac{\partial v}{\partial y}\right) \right], \qquad (4\text{–}20)$$

$$\frac{\partial uh}{\partial x} + \psi\frac{\partial vh}{\partial y} = \psi. \qquad (4\text{–}21)$$

In the above equations, F is the Froude number of the base–normal flow, which according to (4–10) and (4–11) is constant in $\tilde{y}$ and thus given by

$$F = \frac{V_{th}}{\sqrt{g H_{th}}} = \left(\frac{S}{C_f} \right)^{1/2}. \qquad (4\text{–}22)$$

The model places no restriction on the value of this Froude number; indeed it can exceed unity. The parameter ψ in (4–19) ~ (4–21) is defined as

$$\psi = \frac{H_{th}}{SL_{th}}. \qquad (4\text{–}23)$$

As seen in Figure 4–4, it is thus equal to the depth of overland base–normal flow at threshold conditions divided by the elevation drop from the divide to the point $\tilde{y} = L_{th}$ at which the threshold for bed erosion is reached. As the overland flow due to rainfall can be generally be expected to be extremely thin, ψ can be expected to be a very small parameter for most cases of interest. Finally, the dimensionless eddy viscosity ϵ takes the form

$$\epsilon = \alpha S^2 / C_f^{1/2}. \tag{4–24}$$

The parameter α is of the order of 0.1 (Parker, 1978; Ikeda et al., 1990), as is also likely for the parameter $C_f^{1/2}$. It then follows that $\epsilon \sim S^2$ and is thus a small parameter.

Note that in deriving (4–19) and (4–20), the eddy viscosity ν_t has been evaluated using the base–normal result (4–15). The terms involving the eddy viscosity are in general small, so that accuracy sufficient for the present analysis can be achieved by this approximation.

The reason for the normalizations (4–18), and in particular (4–18c, d) can now be readily seen by examining the base flow, for which u and a vanish and v and h are functions of y alone. Equations (4–20) and (4–21) reduce for this case to

$$\psi F^2 v \frac{dv}{dy} = -\psi \frac{dh}{dy} + 1 - \frac{v^2}{h} - \epsilon \psi^2 \frac{d}{dy}(vh\frac{dv}{dy}), \tag{4–20a}$$

$$\frac{dvh}{dy} = 1. \tag{4–21a}$$

It is now seen that in the limit as $\psi \to 0$, the equations governing the base flow

reduce strictly to those governing the base–normal flow.

4.4 Solution

4.4.1 Normal flow assumption

In order to understand the difference between the present model and those of the type of Smith & Bretherton (1972), the solution for normal flow over a perturbed bed is provided here.

In the models of Smith and Bretherton (1972) and Loewenhertz (1991), overland flow over the wavy bed given by (4–1) is analyzed according to the normal flow approximation. It is shown below why this approximation must yield the unsatisfactory result of a characteristic wavelength of drainage basin spacing equal to zero.

a) Linear analysis

If the backwater and Reynolds stress terms are neglected in (4–19) and (4–20), the governing equations take the form

$$-\mathrm{ak}\sin\mathrm{kx}-\frac{\sqrt{\mathrm{u}^2+\mathrm{v}^2}}{\mathrm{h}}\,\mathrm{u}=0, \tag{4–25}$$

$$1-\frac{\sqrt{\mathrm{u}^2+\mathrm{v}^2}}{\mathrm{h}}\,\mathrm{v}=0, \tag{4–26}$$

$$\frac{\partial \mathrm{uh}}{\partial \mathrm{x}}+\psi\frac{\partial \mathrm{vh}}{\partial \mathrm{y}}=\psi. \tag{4–27a}$$

Since backwater effects can be neglected a priori in this analysis, this is no reason to maintain the different scalings in x and y of (4–18c, d) that lead to the justification for their neglect. With this in mind, y is rescaled such that

$$y = \psi\hat{y},$$

so that (4–27a) becomes

$$\frac{\partial uh}{\partial x} + \frac{\partial vh}{\partial \hat{y}} = \psi. \tag{4–27b}$$

Assuming that the dimensionless perturbation amplitude a is infinitesimally small, the following asymptotic expansions are introduced:

$$u = au_1 + \ldots., \tag{4–28}$$

$$v = v_0 + av_1 + \ldots., \tag{4–29}$$

$$h = h_0 + ah_1 + \ldots. \tag{4–30}$$

These expansions are truncated at linear order in amplitude a .

Substituting (4–28), (4–29) and (4–30) into (4–25), (4–26) and (4–27b), the following equations are obtained at $O(1)$:

$$1 - \frac{v_0^2}{h_0} = 0, \tag{4–31}$$

$$\frac{\partial v_0 h_0}{\partial \hat{y}} = \psi. \tag{4–32}$$

Applying the boundary condition of no flow at $\hat{y} = 0$, (4–32) is integrated to yield

$$v_0 h_0 = \psi \hat{y}. \tag{4–33}$$

Between (4–31) and (4–33), the following solutions are obtained:

$$v_0 = \psi^{\frac{1}{3}} \hat{y}^{\frac{1}{3}}, \quad h_0 = \psi^{\frac{2}{3}} \hat{y}^{\frac{2}{3}}. \tag{4–34, 35}$$

These are the base–normal solutions.

At the next order, $O(a)$, the governing equations give

$$-k \sin kx - \frac{v_0}{h_0} u_1 = 0, \tag{4–36}$$

$$-2v_1 + \frac{v_0}{h_0} h_1 = 0, \tag{4–37}$$

$$h_0 \frac{\partial u_1}{\partial x} + h_0 \frac{\partial v_1}{\partial \hat{y}} + \frac{dh_0}{d\hat{y}} v_1 + v_0 \frac{\partial h_1}{\partial \hat{y}} + \frac{dv_0}{d\hat{y}} h_1 = 0. \tag{4–38}$$

With the use of (4–34) and (4–35), (4–36) gives the solution

$$u_1 = -\psi^{\frac{1}{3}} \hat{y}^{\frac{1}{3}} k \sin kx. \tag{4–39}$$

It is found that u_1 is positive between $x = 0$ and π/k, and negative between $x = -\pi/k$ and 0. Since the point $x = 0$ corresponds to an indentation, (4–39) indicates that flow gathers toward the indentations.

The first–order differential equation (4–38) admits solutions of the form

$$v_1 = \psi^{\frac{1}{3}} v_1^{\star} \cos kx, \tag{4–40}$$

$$h_1 = \psi^{\frac{2}{3}} h_1^{\star} \cos kx. \tag{4–41}$$

Substituting with the use of (4–39), (4–40) and (4–41), equation (4–38) gives the following differential equation for $v_1^{\star}$:

$$3\frac{dv_1^{\star}}{d\hat{y}} + 2\hat{y}^{-1} v_1^{\star} - k^2 \hat{y}^{\frac{1}{3}} = 0. \tag{4–42}$$

The solution of (4–42) is composed of the corresponding homogeneous and particular solutions; that is

$$v_1^{\star} = B_0 \hat{y}^{-\frac{2}{3}} + \frac{k^2}{6} \hat{y}^{\frac{4}{3}}, \tag{4–43}$$

where B_0 is an integral constant. With the use of (4–40), (4–41) and (4–43), (4–37) gives

$$h_1^{\star} = 2B_0 \hat{y}^{-\frac{1}{3}} + \frac{k^2}{3} \hat{y}^{\frac{5}{3}}. \tag{4–44}$$

Applying the boundary condition (4–8), B_0 is found to be zero. Then v_1 and h_1 are finally obtained as

$$v_1 = \psi^{\frac{1}{3}} \frac{k^2}{6} \hat{y}^{\frac{4}{3}} \cos kx, \tag{4–45}$$

$$h_1 = \psi^{\frac{2}{3}} \frac{k^2}{3} \hat{y}^{\frac{5}{3}} \cos kx. \tag{4–46}$$

The solution (4–45) shows that the velocity at troughs (e.g. $\tilde{y} = 0$ in Figure 4–2) is proportional to the square of k and is maximized for infinitely large values of k, or infinitesimally small wavelength. This is the fundamental reason for the failure of the linear model of Smith and Bretherton (1972) to select drainage basin wavelength.

b) Full nonlinear analysis

In fact, it is possible to obtain an exact nonlinear solution to (4–25), (4–26) and (4–27a). This solution is here used to illustrate that the normal flow approximation of those equations implies the unsatisfactory result of infinite flow concentration in the troughs for any $y > 0$.

Equations (4–25), (4–26) and (4–27) reduce to

$$\frac{q_y}{q_x} = -\frac{1}{ka \sin kx}, \tag{4–47}$$

$$\frac{\partial q_x}{\partial x} + \psi \frac{\partial q_y}{\partial y} = \psi, \tag{4–48}$$

where q_x and q_y are the discharges per unit width in the x and y directions, respectively, given by

$$q_x = uh, \quad q_y = vh. \tag{4–49, 50}$$

Since streamlines are defined such that

$$\frac{dy}{dx} = \frac{v}{u}, \tag{4–51}$$

it follows for the present case that

$$\frac{dy}{dx} = -\frac{1}{ka \sin kx}. \tag{4–52}$$

Equation (4–52) is integrated to yield

$$y = -\frac{1}{2ak^2} \ln \frac{1-\cos kx}{1+\cos kx} + B_1. \tag{4–53}$$

Suppose the streamline passes through the point (x_p, y_p), as shown in Figure 4–5. The integral constant B_1 is then calculated as

$$B_1 = y_p + \frac{1}{2ak^2} \ln \frac{1-\cos kx_p}{1+\cos kx_p}. \tag{4–54}$$

The continuity equation (4–48) can be integrated to yield

$$\int\int_{A_p} \text{div} \cdot \mathbf{q}\, dA_p = \int_{S_p} \mathbf{q} \cdot \mathbf{n}_p\, dS_p = \int\int_{A_p} \psi\, dA_p, \tag{4–55}$$

where div $= (\partial/\partial x,\ \partial/\partial(y/\psi))$, A_p is a given area, S_p is the closed curve surrounding A_p and $\mathbf{n}_p$ is a unit outward vector normal to S_p. If A_p is defined to be the area APBO shown in Figure 4–5, the discharge crossing OA, PB and BO vanishes, and (4–55) reduces to

$$\int_0^{x_p} q_y(x,y_p)\, dx = \psi A_p(x_p,y_p). \tag{4–56}$$

The $A_p(x_p,y_p)$ can be expressed as

$$A_p(x_p,y_p) = x_p y_p + \int_{x_p}^{x_b} y(x;\, x_p,y_p)\, dx, \tag{4–57}$$

where x_b is the x coordinate of the point B where the streamline crosses the x axis. This value can be derived from (4–53) and (4–54) at $y = 0$; that is

$$\frac{1}{2ak^2} \ln \frac{1 - \cos\ kx_b}{1 + \cos\ kx_b} = y_p + \frac{1}{2ak^2} \ln \frac{1 - \cos\ kx_p}{1 + \cos\ kx_p}. \tag{4–58}$$

Substituting (4–57) into (4–56) and taking the derivative with regard to x_p, q_y is obtained as

$$q_y(x_p,y_p) = \frac{\psi(x_b - x_p)}{ak \sin\ kx_p}. \tag{4–59}$$

With the aid of (4–58), (4–59) reduces to

$$q_y(x_p,y_p) = \psi \frac{\frac{1}{k}\cos^{-1}\left[\frac{2}{1+\exp(2ak^2y_p+\ln\frac{1-\cos kx_p}{1+\cos kx_p})} - 1\right] - x_p}{ak \sin kx_p}. \tag{4–60}$$

The above equation is of considerable interest. Note that $q_y(0, 0) = 0$, but $q_y(0, y_p)$ is equal to infinity for any $y_p > 0$. Since the point $x = 0$ corresponds to the trough, it follows that infinite discharge gathers in the indentations in the absence of friction or backwater effects. It is this feature of the normal flow approximation applied to the topography of (4–1) that led to the failure to obtain finite wavelength selection in Lowenhertz (1991). She was able to overcome this difficulty only at the expense of introducing an ad–hoc "smearing" function. Here, however, it will be found that the problem can be resolved satisfactorily by properly including the backwater and friction terms.

If y_p is large enough, q_y converges to the simple form

$$q_y(x_p,y_p) = \frac{\psi(\frac{\pi}{k} - x_p)}{ak \sin kx_p}. \tag{4–61}$$

4.4.2 Linear analysis including the backwater and the Reynolds stress terms

In this analysis, a perturbation technique using a, ψ and ϵ as small parameters is employed. As seen in (4–19), (4–20) and (4–21), the small parameters ψ and ϵ scale the magnitude of the streamwise backwater effect and the

transverse Reynolds stress, respectively. While ψ and ϵ are characteristic parameters of each system, bed amplitude a is a parameter which can be chosen arbitrarily. Here the following composite expansions are introduced in order to allow for a linear analysis in a .

$$u = au_1 + O(a^2)$$
$$= a[u_{100} + \psi u_{110} + \epsilon u_{101} + O(\psi^2, \psi\epsilon, \epsilon^2)] + O(a^2), \qquad (4\text{–}62a)$$

$$v = v_0 + av_1 + O(a^2)$$
$$= v_{000} + \psi v_{010} + \epsilon v_{001} + \psi^2 v_{020} + \psi\epsilon v_{011} + \epsilon^2 v_{002} + O(\psi^3, \psi^2\epsilon, \psi\epsilon^2, \epsilon^3)$$
$$+ a[v_{100} + \psi v_{110} + \epsilon v_{101} + O(\psi^2, \psi\epsilon, \epsilon^2)] + O(a^2), \qquad (4\text{–}63a)$$

$$h = h_0 + ah_1 + O(a^2)$$
$$= h_{000} + \psi h_{010} + \epsilon h_{001} + \psi^2 h_{020} + \psi\epsilon h_{011} + \epsilon^2 h_{002} + O(\psi^3, \psi^2\epsilon, \psi\epsilon^2, \epsilon^3)$$
$$+ a[h_{100} + \psi h_{110} + \epsilon h_{101} + O(\psi^2, \psi\epsilon, \epsilon^2)] + O(a^2). \qquad (4\text{–}64a)$$

Some elaboration is in order concerning the nature of these expansions. Terms of $O(a^2)$ have been dropped, while terms of $O(\psi^2)$, $O(\psi\epsilon)$, $O(\epsilon^2)$, $O(a\psi)$ and $O(a\epsilon)$ have been retained. A necessary condition for the validity of the expansion is that a be one order of magnitude below the minimum of ψ and ϵ. This condition is compatible with a linear stability analysis in a.

In the limit as $a \to 0$, the expansions reduce to forms describing the base flow;

$$u = 0, \qquad (4\text{–}62b)$$

$$v = v_0(y)$$
$$= v_{000} + \psi v_{010} + \epsilon v_{001} + \psi^2 v_{020} + \psi\epsilon v_{011} + \epsilon^2 v_{002}, \qquad (4\text{–}63b)$$

$$h = h_0(y)$$
$$= h_{000} + \psi h_{010} + \epsilon h_{001} + \psi^2 h_{020} + \psi\epsilon h_{011} + \epsilon^2 h_{002}. \qquad (4\text{–}64b)$$

The base–normal solution for v and h is recovered as ψ and ϵ go to zero, i.e. $v_0(y) \rightarrow v_{000}(y)$ and $h_0(y) \rightarrow h_{000}(y)$.

Let $y = \ell$ denote the dimensionless distance downstream of the ridge at which the threshold condition for bed erosion is reached. The normalization (4–18d) ensures that $\ell = 1$ for the base–normal flow. It can be deduced from (4–17a), (4–18d) and (4–63b) that ℓ deviates slightly from unity in the case of the base flow. This deviation, however, is not a function of the transverse direction x.

When transverse bed variation is included according to (4–1), ℓ will be found to be a function of x. This variation will prove to be the key in determining the characteristic wavenumber of drainage basin spacing. The linear terms in ϵ and ψ in (4–63b) and (4–64b) will be found to play a role in the variation of ℓ in x up to linear order in a in (4–63a, b, c). The nonlinear terms in ψ and ϵ in (4–63b) and (4–64b) are found not to affect the process of wavenumber selection up to linear order in a. As a result, the terms v_{020}, v_{011}, v_{002}, h_{020}, h_{011} and h_{002} are not computed here.

a) Boundary and integral conditions

In order to solve (4–19) ~ (4–21) with the use of the above expansions, it is

first useful to specify appropriate boundary and integral conditions on the problem. According to (4–7), there is to be no water inflow at the divide of Figure 5–2. In dimensionless notation, then,

$$vh = 0 \text{ at } y = 0. \tag{4–65}$$

The bed profile specified by (4–1) is periodic in x; here solutions to (4–19) ~ (4–21) that are likewise periodic in x are sought. It follows from conditions of symmetry that the transverse discharge uh must vanish at both troughs and ridges of Figure 4–2. The presence of uniform rainfall ensures that depth h is nonzero everywhere except at y = 0. It thus follows that

$$u = 0 \text{ at } x = 0, \pm \frac{\pi}{k}, \pm 2\frac{\pi}{k}, \ldots \tag{4–66}$$

Finally, (4–21) can be integrated over one wavelength from $x = -\pi/k$ to $x = +\pi/k$ and reduced with (4–65) and (4–66) to yield the following result;

$$\int_{-\pi/k}^{\pi/k} vh \, dx = 2\frac{\pi}{k} y. \tag{4–67}$$

b) Solution at $O(a^0)$

Substituting (4–62), (4–63) and (4–64) into (4–20), (4–21), and (4–65) the following equations are obtained at lowest order:

$$1 - \frac{v_{000}^2}{h_{000}} = 0, \tag{4–68}$$

$$\frac{dv_{000}h_{000}}{dy} = 1, \tag{4–69}$$

with the boundary condition

$$v_{000}y_{000} = 0 \text{ at } y = 0. \tag{4–70}$$

Equation (4–69) can be integrated with the aid of (4–70) to yield

$$v_{000}h_{000} = y. \tag{4–71}$$

Equations (4–68) and (4–71) then give the following solutions:

$$v_{000} = y^{\frac{1}{3}}, \quad h_{000} = y^{\frac{2}{3}}. \tag{4–72, 73}$$

These forms can be immediately recognized as the base–normal solution obtained in 4.3.2. As such, they do not include any of the effects of perturbed bed topography, backwater or turbulent diffusion.

The following equations are found to govern the terms at $O(a^0\psi^1\epsilon^0)$ in the expansions (4–62) to (4–64):

$$F^2 v_{000}\frac{dv_{000}}{dy} = -\frac{dh_{000}}{dy} - 2\frac{v_{000}}{h_{000}}v_{010} + \left(\frac{v_{000}}{h_{000}}\right)^2 h_{010}, \tag{4–74}$$

$$\frac{d}{dy}(v_{010}h_{000} + v_{000}h_{010}) = 0, \tag{4–75}$$

with the boundary condition

$$v_{010}h_{000} + v_{000}h_{010} = 0 \text{ at } y = 0. \tag{4–76}$$

With the aid of (4–72) and (4–73), (4–74) ~ (4–76) give solutions of the form

$$v_{010} = -\frac{F^2 + 2}{9}, \tag{4–77}$$

$$h_{010} = \frac{F^2 + 2}{9} y^{\frac{1}{3}}. \tag{4–78}$$

At $O(a^0\psi^0\epsilon^1)$ of the expansion, the governing equations yield

$$-2\frac{v_{000}}{h_{000}}v_{001} + (\frac{v_{000}}{h_{000}})^2 h_{001} = 0, \tag{4–79}$$

$$\frac{d}{dy}(v_{001}h_{000} + v_{000}h_{001}) = 0, \tag{4–80}$$

with the boundary condition

$$v_{001}h_{000} + v_{000}h_{001} = 0 \text{ at } y = 0. \tag{4–81}$$

Equations (4–79) ~ (4–81) can be solved with the aid of (4–72) and (4–73), yielding

$$v_{001} = 0, \quad h_{001} = 0. \tag{4–82, 83}$$

Before starting the analysis at the next order, $O(a^1)$, it is useful to summarize the base solutions at $O(a^0)$ as follows:

$$v_0 = y^{\frac{1}{3}} - \psi\frac{F^2+2}{9} + O(\psi^2, \psi\epsilon, \epsilon^2), \tag{4–84}$$

$$h_0 = y^{\frac{2}{3}} + \psi\frac{F^2+2}{9}y^{\frac{1}{3}} + O(\psi^2, \psi\epsilon, \epsilon^2). \tag{4–85}$$

Calculated curves for v_0 and h_0 are depicted in Figure 4–6 for the case $F = 0.5$ and three values of ψ. It is readily seen that the base–normal solution is quite accurate as long as ψ is sufficiently small.

Note that the base solutions are not carried to $O(\psi^2, \psi\epsilon, \epsilon^2)$ here, as the results do not affect wavelength selection at the linear order in a.

c) Solution at $O(a^1)$

At $O(a^1\psi^0\epsilon^0)$ in the expansions, the following equations are obtained:

$$\frac{\partial h_{100}}{\partial x} - \frac{v_{000}}{h_{000}}u_{100} + k \sin kx = 0, \tag{4–86}$$

$$-2\frac{v_{000}}{h_{000}}v_{100} + \left(\frac{v_{000}}{h_{000}}\right)^2 h_{100} = 0, \tag{4–87}$$

$$h_{000}\frac{\partial u_{100}}{\partial x} = 0, \tag{4–88}$$

with the boundary condition

$$u_{100} = 0 \text{ at } x = 0, \tag{4–89}$$

and the integral condition

$$\int_{-\pi/k}^{\pi/k} (v_{000}h_{100} + h_{000}v_{100})\, dx = 0 \tag{4–90}$$

These relations yield the solutions

$$u_{100} = 0 \tag{4–91}$$

$$h_{100} = \cos kx \tag{4–92}$$

$$v_{100} = \frac{1}{2} y^{-\frac{1}{3}} \cos kx. \tag{4–93}$$

At $O(a^1\psi^1\epsilon^0)$ in the expansion, the following equations are obtained:

$$-\frac{\partial h_{110}}{\partial x} - \frac{v_{000}}{h_{000}}u_{110} = 0, \tag{4–94}$$

$$F^2 v_{000}\frac{\partial v_{100}}{\partial y} + F^2 v_{100}\frac{\partial v_{000}}{\partial y} + \frac{\partial h_{100}}{\partial y} = -2\frac{v_{000}}{h_{000}}\left(\frac{v_{010}}{v_{000}} - \frac{h_{010}}{h_{000}}\right)v_{100}$$

$$-2\frac{v_{000}}{h_{000}}v_{110}-2\left(\frac{v_{000}}{h_{000}}\right)^2\left(\frac{v_{010}}{v_{000}}-\frac{h_{010}}{h_{000}}\right)h_{100}+\left(\frac{v_{000}}{h_{000}}\right)^2 h_{110},$$

(4–95)

$$\frac{\partial u_{110}}{\partial x}h_{000}+\frac{\partial}{\partial y}\left(v_{000}h_{100}+v_{100}h_{000}\right)=0. \tag{4–96}$$

with the boundary condition

$$u_{110}=0 \text{ at } x=0, \tag{4–97}$$

and the integral condition

$$\int_{-\pi/k}^{\pi/k}\left(v_{110}h_{000}+h_{110}v_{000}+v_{010}h_{100}+h_{010}v_{100}\right)dx = 0. \tag{4–98}$$

With the aid of (4–72) and (4–73), (4–94) ~ (4–98) give the solutions

$$u_{110}=-\frac{y^{-\frac{4}{3}}}{2k}\sin kx, \tag{4–99}$$

$$h_{110}=-\frac{y^{-\frac{5}{3}}}{2k^2}\cos kx, \tag{4–100}$$

$$v_{110}=-\left(\frac{y^{-2}}{4k^2}+\frac{F^2+2}{9}y^{-\frac{2}{3}}\right)\cos kx. \tag{4–101}$$

At $O(a^1\psi^0\epsilon^1)$, the following equations are obtained:

$$-\frac{\partial h_{101}}{\partial x}-\frac{v_{000}}{h_{000}}u_{101}=0, \tag{4–102}$$

$$-2\frac{v_{000}}{h_{000}}v_{101}+\left(\frac{v_{000}}{h_{000}}\right)^{2}h_{101}+y\frac{\partial^{2}v_{100}}{\partial x^{2}}=0, \tag{4–103}$$

$$\frac{\partial u_{101}}{\partial x}h_{000}=0, \tag{4–104}$$

with the boundary condition

$$u_{101}=0 \text{ at } x=0, \tag{4–105}$$

and the integral condition

$$\int_{-\pi/k}^{\pi/k}(v_{101}h_{000}+h_{101}v_{000}+v_{001}h_{100}+h_{001}v_{100})\,dx = 0. \tag{4–106}$$

The solutions are found to be

$$u_{101}=0, \tag{4–107}$$

$$h_{101}=0, \tag{4–108}$$

$$v_{101}=-\frac{k^{2}}{4}y\cos kx. \tag{4–109}$$

The solutions at $O(a^{1})$ can now be summarized as follows:

$$u_1 = \left[-\psi \frac{y^{-\frac{4}{3}}}{2k} + O(\psi^2, \psi\epsilon, \epsilon^2) \right] \sin kx, \tag{4–110}$$

$$v_1 = \left[\frac{y^{-\frac{1}{3}}}{2} - \psi \left(\frac{y^{-2}}{4k^2} + \frac{F^2 + 2}{9} y^{-\frac{1}{3}} \right) - \epsilon \frac{k^2}{4} y + O(\psi^2, \psi\epsilon, \epsilon^2) \right] \cos kx, \tag{4–111}$$

$$h_1 = \left[1 - \psi \frac{y^{-\frac{5}{3}}}{2k^2} + O(\psi^2, \psi\epsilon, \epsilon^2) \right] \cos kx. \tag{4–112}$$

Recalling from (4–1) and Figure 4–2 that $x = 0$ corresponds to the bottom of a trough, equation (4–111) is seen to predict intensified flow velocity at indentations associated with the bed perturbation. In order to look at the effect of wavenumber on the profile of v_1 for $x = 0$, calculated results for three different wavenumbers are shown in Figure 4–7. It is seen that $v_1|_{x=0}$ for a wavenumber $k = 30$ is larger than the corresponding value for $k = 0.3$ for small values of y. This tendency is, however, reversed for large values of y. This reversal suggests the existence of some finite value of k which maximizes the flow intensification at a certain distance downstream of the divide.

Finally, the complete form of the solutions to the order indicated in (4–62) ~ (4–64) is

$$u = a\left[-\psi \frac{y^{-\frac{4}{3}}}{2k} + O(\psi^2, \psi\epsilon, \epsilon^2) \right] \sin kx + O(a^2), \tag{4–113}$$

$$v = y^{\frac{1}{3}} - \psi \frac{F^2 + 2}{9} + O(\psi^2, \psi\epsilon, \epsilon^2)$$

$$+ a\Big[\frac{y^{-\frac{1}{3}}}{2} - \psi\Big(\frac{y^{-2}}{4k^2} + \frac{F^2+2}{9}y^{-\frac{1}{3}}\Big) - \epsilon\frac{k^2}{4}y + O(\psi^2,\psi\epsilon,\epsilon^2)\Big]\cos kx + O(a^2), \tag{4–114}$$

$$h = y^{\frac{2}{3}} + \psi\frac{F^2+2}{9}y^{\frac{1}{3}} + O(\psi^2,\psi\epsilon,\epsilon^2) + a\Big[1 - \psi\frac{y^{-\frac{5}{3}}}{2k^2} + O(\psi^2,\psi\epsilon,\epsilon^2)\Big]\cos kx + O(a^2). \tag{4–115}$$

Note that the terms in the expansions (4–62) ~ (4–64) of $O(\psi^2)$, $O(\psi\epsilon)$, and $O(\epsilon^2)$ have not been obtained explicitly here. It suffices to mention that these terms are independent of the bed perturbation introduced in (4–1), and thus contain no functionality in transverse direction x or transverse wavenumber k. As a result, they play no role in the determination of characteristic wavelength.

4.5 Threshold hypothesis

According to the scenario of the threshold concept, the wavelength which minimizes the distance from the divide to the first point downstream at which the threshold condition for bed erosion is attained should dominate, at least in the initial stages of bed erosion. Here this wavelength is called the characteristic wavelength associated with the threshold concept. To obtain the characteristic wavelength, the distance to the point at which the threshold condition is first realized must be related to velocity intensification.

As pointed out in Chapter 2, the appropriate dimensioned form of the Exner

relation for the present purely erosional analysis is

$$\frac{\partial \tilde{\eta}_b}{\partial \tilde{t}} = \begin{cases} 0 & \text{if } \tilde{\tau} \leq \tilde{\tau}_{th} \\ -\frac{1}{1-\lambda_p} E_s (\tilde{\tau} - \tilde{\tau}_{th})^{\gamma} & \text{if } \tilde{\tau} > \tilde{\tau}_{th} \end{cases}, \tag{4–116}$$

where λ_p denotes bed porosity, E_s is a positive constant, and $\tilde{\tau}$ denotes the magnitude of the bed shear stress vector, given by

$$\tilde{\tau} = (\tau_x^2 + \tau_y^2)^{1/2} = \rho C_f (u^2 + v^2). \tag{4–117}$$

It follows from (4–117) that a threshold velocity magnitude V_{th} can be defined as follows:

$$\tau_{th} = \rho C_f V_{th}^2. \tag{4–118}$$

This threshold velocity was introduced earlier to allow for a nondimensional treatment of the governing equations. It follows from (4–18a,b), (4–117), and (4–118) that the dimensionless form for the condition describing the attainment of threshold conditions is

$$u^2 + v^2 = 1. \tag{4–119}$$

Now let $y = \ell(x)$ denote the distance downstream of the divide at which the threshold condition is attained, as described in Figure 4–2. Substituting the expansions (4–62) and (4–63) into (4–119) and reducing, it is found that the

threshold condition reduces to

$$\begin{aligned}
&[v_{000}(y) + \psi v_{010}(y) + \epsilon v_{001}(y) \\
&+ \psi^2 v_{020}(y) + \psi\epsilon v_{011}(y) + \epsilon^2 v_{002}(y) \\
&+ a v_{100}(x,y) + a\psi v_{110}(x,y) + a\epsilon v_{101}(x,y) \\
&+ O(a^2)]|_{y=\ell} = 1.
\end{aligned} \tag{4–120}$$

Comparing (4–72) and (4–120), it is seen that the base–normal solution yields the result

$$\ell = 1. \tag{4–121}$$

Indeed, the normalizations (4–18) were chosen so as to provide this result.

The $O(\psi)$, $O(\epsilon)$, $O(\psi^2)$, $O(\psi\epsilon)$, and $O(\epsilon^2)$ terms in (4–120) correspond to the deviation of the base flow from the base normal flow, and contain no dependency in x. Where ℓ_0 denotes the distance, independent of x, at which threshold conditions are obtained by the base mode, these terms insure that ℓ_0 differs slightly from unity. Since ℓ_0 does not depend upon x, these terms play no role in wavelength selection here.

The $O(a)$, $O(a\psi)$, and $O(a\epsilon)$ terms in (4–120), however, depend upon x, as seen by a perusal of (4–114). Indeed, it is seen from that equation that as long as ψ and ϵ are small, flow velocity is maximized in the troughs (e.g. $x = 0$) near $y = 1$. This in turn implies that the threshold condition is reached in a shorter distance from the divide along the troughs (e.g. $x = 0$) than for any other values of x. The question of wavelength selection, then concerns the determination of the

wavenumber k that allows for the shortest distance along a trough from the divide to the point at which the threshold condition is attained.

In general, the distance $\ell(x)$ can be written in terms of its deviation from the base normal value:

$$\ell = 1 - \Delta\ell(x). \tag{4–122}$$

where $\Delta\ell$ denotes the deviation from the threshold distance predicted from the base normal solution. The negative sign in (4–122) has been introduced so that the maximum value of $\Delta\ell$ corresponds to the shortest distance from the divide to the point at which threshold conditions are realized. Substituting (4–122) into (4–120) and reducing with the forms of (4–114), it is found that

$$\Delta\ell(x) = \Delta\ell_0 + a\,\Delta\ell_1(x), \tag{4–123a}$$

where

$$\Delta\ell_0 = -\psi\frac{F^2+2}{3} + O(\psi^2, \psi\epsilon, \epsilon^2), \tag{4–123b}$$

$$\Delta\ell_1(x) = 3\left[\frac{1}{2} - \psi\left(\frac{1}{4k^2} + \frac{F^2+2}{9}\right) - \epsilon\frac{k^2}{4} + O(\psi^2, \psi\epsilon, \epsilon^2)\right]\cos kx + O(a). \tag{4–123c}$$

Here the value $\Delta\ell_0$ is associated with the deviation of the base flow from the base

normal flow; it is not a function of x. The parameter $\Delta\ell_1(x)$, on the other hand, is a function of both x and k, and thus plays a crucial role in determining characteristic wavenumber. The condition for maximum trough value of $\Delta\ell$ takes the form

$$\frac{\partial}{\partial k}\Delta\ell(0) = \frac{\partial}{\partial k}\Delta\ell_1(0) = 0. \tag{4–124}$$

This yields the characteristic wavenumber k_c given below;

$$k_c = \left(\frac{\psi}{\epsilon}\right)^{\frac{1}{4}}. \tag{4–125}$$

The nature of the maximum of $\Delta\ell_1(0)$ in k is explored in Figure 4–8 for the case F = 0.5, ϵ = 0.00017, and the values of ψ of 0.0017, 0.017, and 0.17.

4.6 Discussion

Recapitulating, ψ and ϵ are given by the relations

$$\psi = \frac{H_{th}}{SL_{th}}, \quad \epsilon = \alpha\frac{S^2}{\sqrt{C_f}}.$$

Using (4–18e) to relate dimensionless wavenumber k to its dimensioned form $\tilde{k}$, and recalling that $\tilde{k} = 2\pi/\tilde{\lambda}$ where $\tilde{\lambda}$ denotes the dimensioned wavelength of basin spacing shown in Figure 4–2, (4–125) is seen to yield the following result for characteristic wavelength $\tilde{\lambda}_c$:

$$\tilde{\lambda}_c = \frac{2\pi H_{th}}{S} \left(\alpha \frac{S^3 L_{th}}{\sqrt{C_f} H_{th}} \right)^{\frac{1}{4}}$$

$$= 2\pi \, \alpha^{\frac{1}{4}} S^{-\frac{1}{4}} C_f^{-\frac{1}{8}} H_{th}^{\frac{3}{4}} L_{th}^{\frac{1}{4}}. \qquad (4\text{–}126)$$

A threshold shear velocity u^*_{th} can be defined as follows:

$$u^*_{th} = \sqrt{C_f} V_{th}. \qquad (4\text{–}127)$$

Using (4–127) and (4–17b), (4–126) can be reduced to

$$\tilde{\lambda}_c = \frac{2\pi}{g} \left(\frac{\alpha}{C_f} \right)^{\frac{1}{4}} u^{*\frac{9}{4}}_{th} S^{-\frac{5}{4}} I^{-\frac{1}{4}}. \qquad (4\text{–}128)$$

An appropriate value for α is 0.2 (Ikeda, 1991); likewise, a crude but reasonable estimate for C_f for overland flow is 0.01 (Yoon et al., 1971; Shen et al., 1973). With these values, (4–128) takes the form

$$\tilde{\lambda}_c = 1.36 \, u^{*\frac{9}{4}}_{th} S^{-\frac{5}{4}} I^{-\frac{1}{4}}. \qquad (4\text{–}129)$$

It is thus seen that the predicted characteristic wavelength of drainage basin spacing is proportional to the threshold shear velocity to the 9/4 power, slope to the minus 5/4 power, and rainfall intensity to the minus 1/4 power.

In order to determine the meaning of (4–129), it is useful to have some reasonable estimates for u^*_{th}, S and I applicable to overland flow. It is known that the threshold shear velocity over cohesive soils varies from about 5 cm/s for sandy

loam to about 15 cm/s for rigid clay (Kikkawa, 1985). Here a value of 10 cm/s is taken for a sample calculation. Slope S is assumed to be 0.01. Rainfall intensity is assumed to be 100 mm/h, i.e. 2.78×10^{-5} m/s.

From these estimates, it is found from (4–127), (4–10), and (4–9) that $V_{th} = 1.00$ m/s, $L_{th} = 3670$ m, and $H_{th} = 0.102$ m. The parameters ψ and ϵ are found from (4–23) and (4–24) to take the respective values 2.78×10^{-3} and 2.00×10^{-4}, justifying the assumption that they are small. Characteristic wavelength is computed from (4–129) to be 33.1 m.

This value of wavelength is of the right order of magnitude, but still somewhat smaller than the typical spacing between the smallest tributaries in a typical drainage basin (Dietrich, 1993 personal communication), which is often found to be of the order of 100 m. It is important to realize, however, that the spacing observed in nature is likely the result of a long process of erosion, only the earliest stages of which are predicted by the present theory. Both nonlinear and long–time effects can be expected to modify the spacing about the value predicted by the present theory. In Figure 4–9, a flat, tilted plane with an initial low slope is shown, along with the incipient channel heads predicted by the present theory. These channel heads would then proceed to migrate upstream, with some incipient basins being captured by others. At the same time, the entire plane would be eroded into a convex profile, with a much steeper upper reach (e.g. Smith and Bretherton, 1974). The initial spacing would provide a base scale for, but not precisely determine, the spacing resulting after the passage of geologic time.

4.7 Conclusions

A theoretical model is presented to explain the process of upstream–driven drainage basin inception.

As a first simple model, normal flow over a tilted bed that is wavy in the transverse direction is considered. A linear formulation yields the result that maximum flow concentration is realized at infinitely large wavenumber k, or zero distance of spacing between adjacent incipient basins. A fully nonlinear treatment reveals that the absence of backwater effects leads to infinite concentration of flow at the center of indentations, or troughs of the wavy bed. This the reason why the normal flow models of both Smith and Bretherton (1974) and Loewenhertz (1991) fail to predict a finite incipient spacing of drainage basins.

In order to perform the analysis so as to include both backwater effects and the effect of transverse Reynolds stresses, a perturbation technique involving three small parameters a, ψ, and ϵ is adopted. Here the parameter a characterizes the amplitude of the wavy bed, ψ characterizes streamwise backwater effects, and ϵ characterizes the Reynolds stresses. The analysis gives both the velocity and depth distributions in explicit form. It is found that effects scaling with the parameter ψ tend to increase characteristic wavelength k_c, and effects scaling with ϵ tend to decrease it. The model successfully predicts that maximized flow concentration to indentations is realized at a finite wavenumber.

A threshold hypothesis for bed erosion is introduced to predict the characteristic wavelength $\tilde{\lambda}_c$. According to this model, it is found that k_c falls in the range $= 0.1 \sim 10$, which corresponds to a characteristic wavelength of the order of H_{th}/S. The relation between the characteristic wavelength and the threshold shear velocity for bed erosion, the slope of the tilted plane, and rainfall intensity is obtained in explicit form.

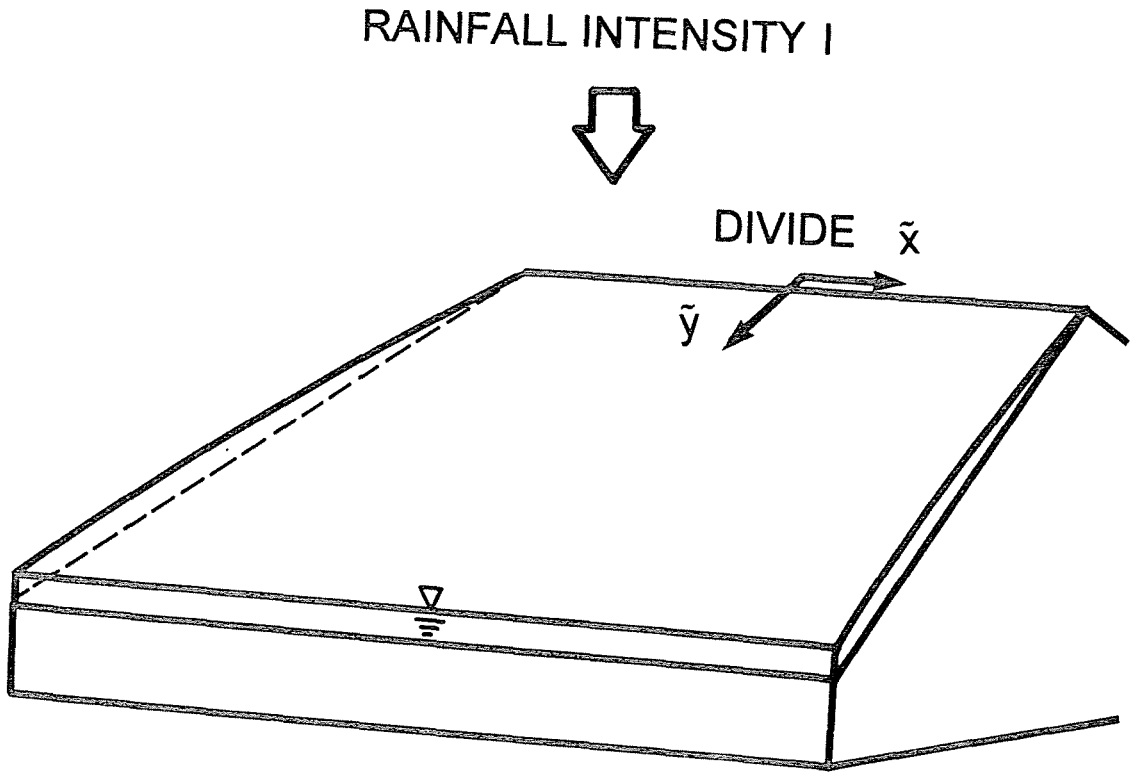

Figure 4–1. Schematic diagram showing a plateau. Flow is in the positive y direction.

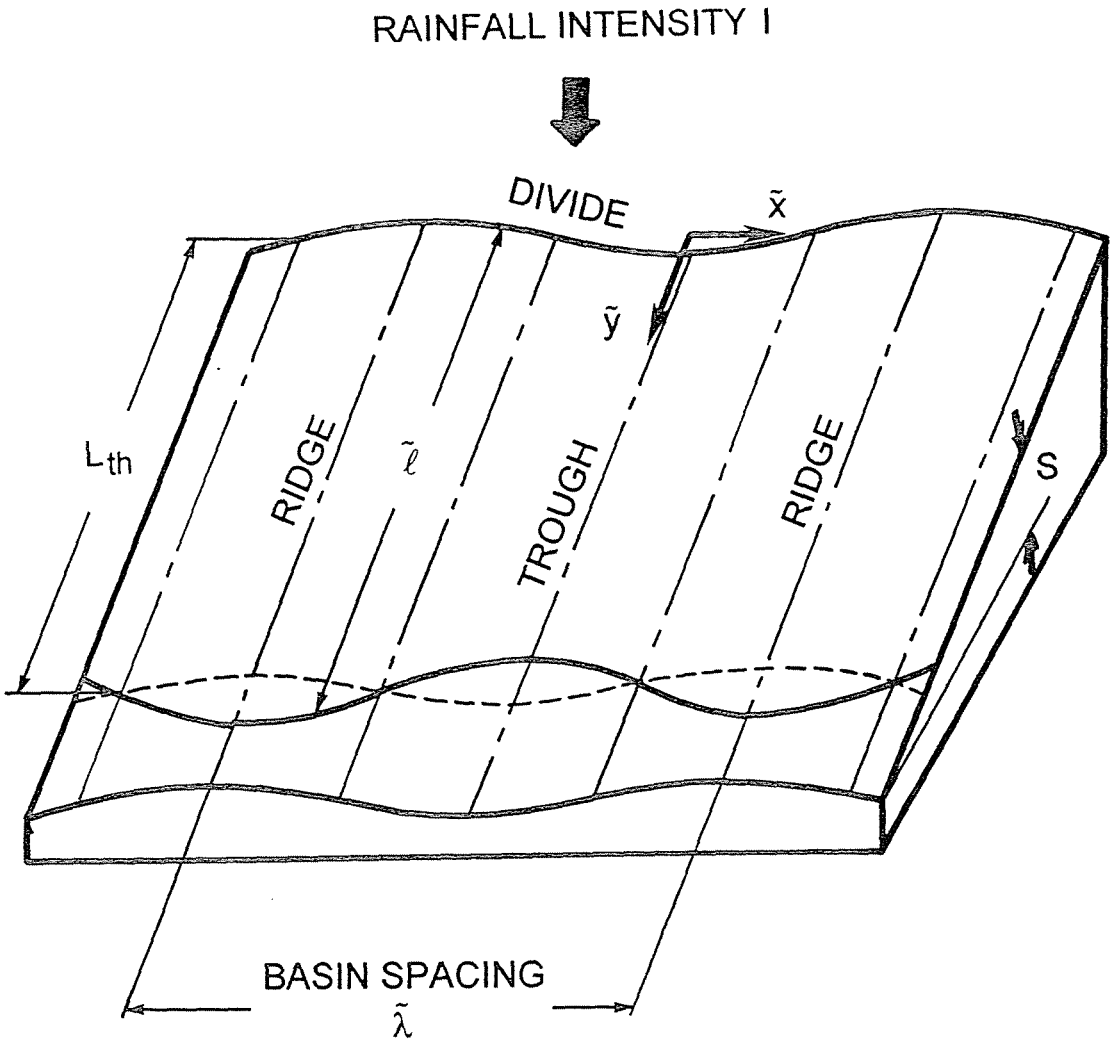

Figure 4–2. Schematic diagram showing perturbation on the plateau.

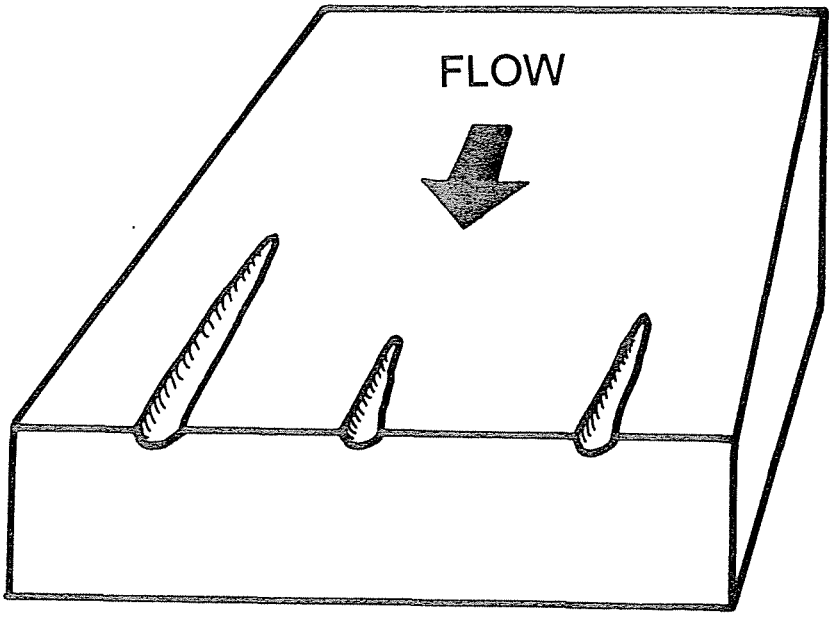

Figure 4–3. Schematic diagram showing upstream–driven channel inception

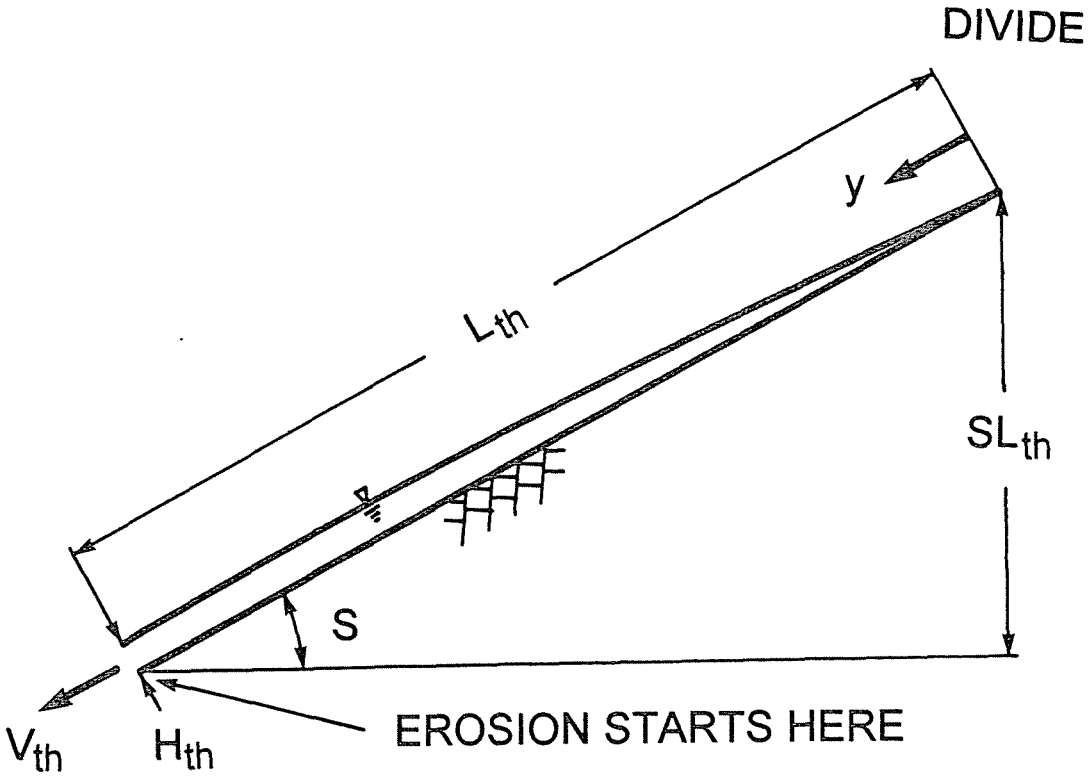

$$\psi = \frac{H_{th}}{SL_{th}}$$

Figure 4–4. Definition diagram showing parameter $\psi = H_{th}/(SL_{th})$.

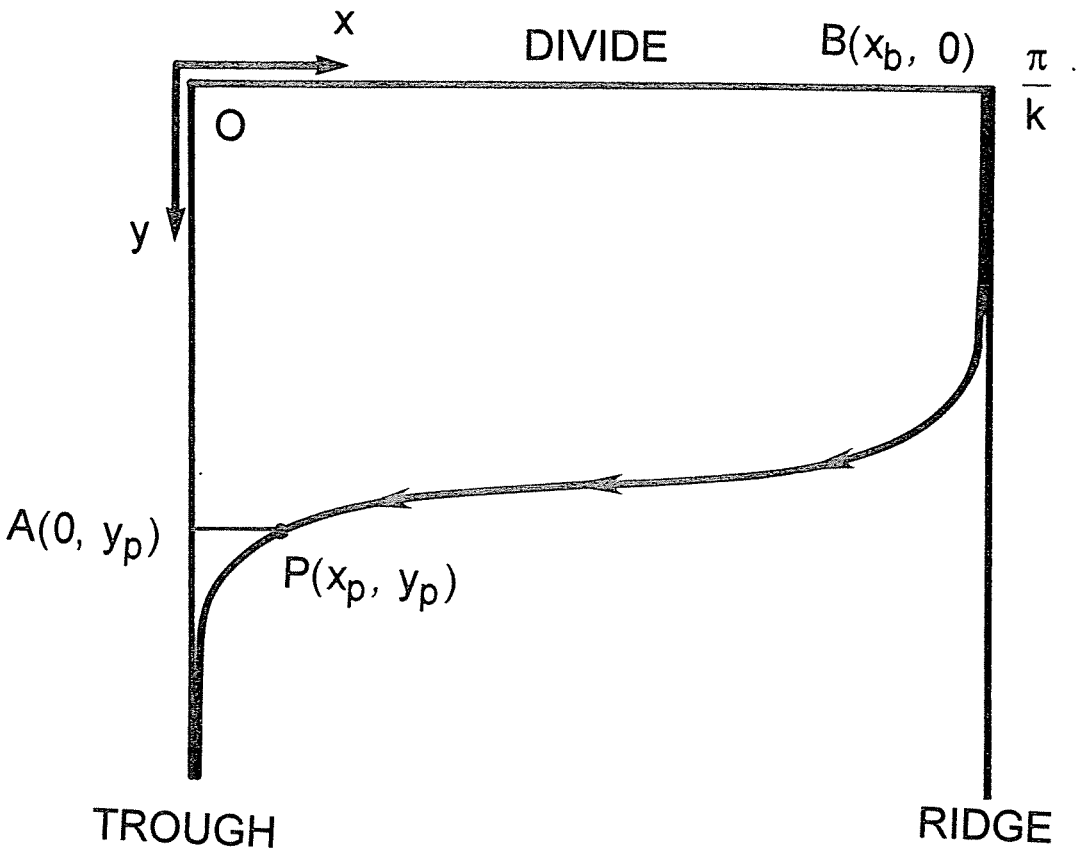

Figure 4–5. Streamline derived from the nonlinear analysis of normal flow assumption

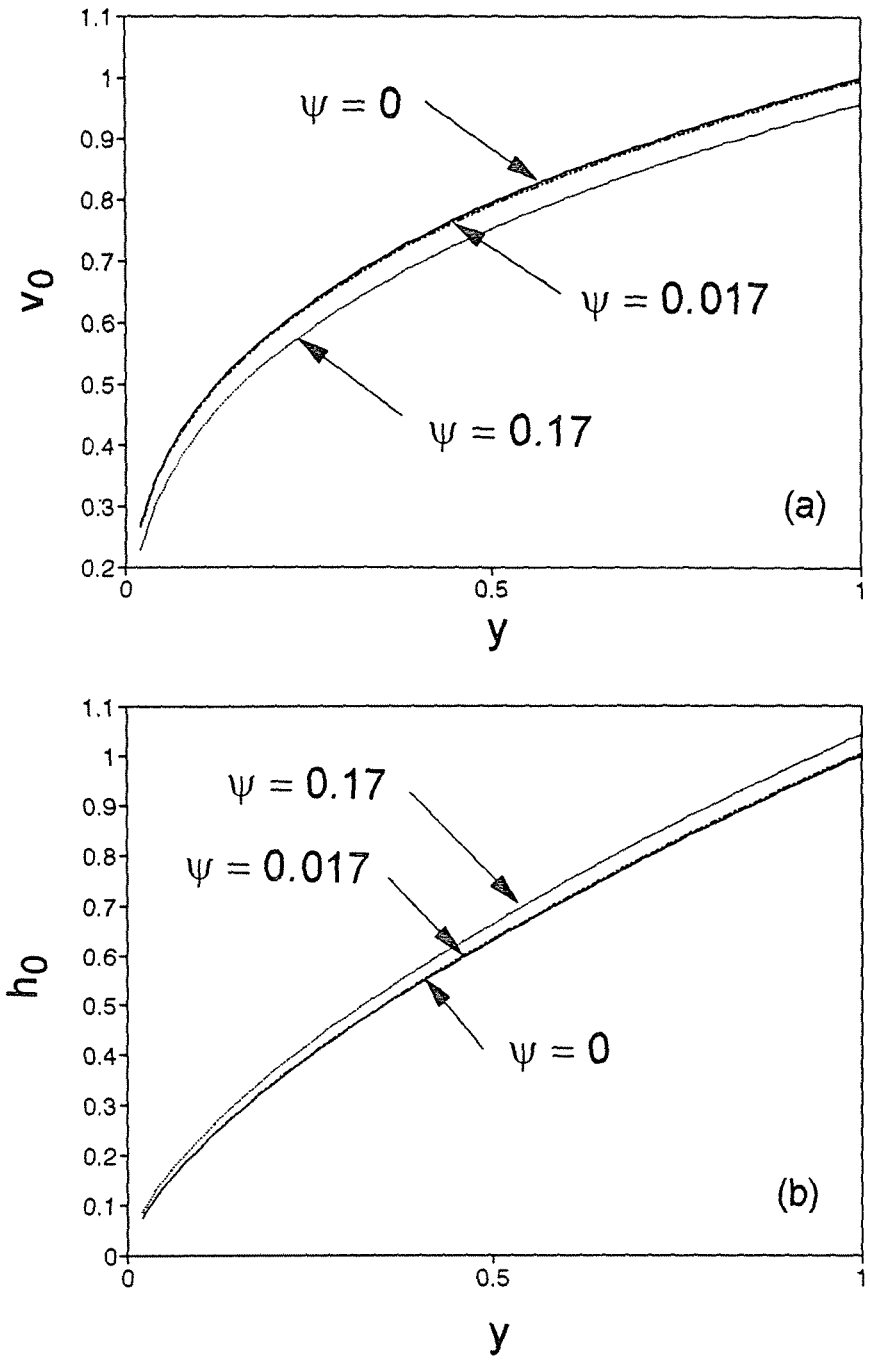

Figure 4–6. Velocity and depth profiles for the case F = 0.5, and ψ = 0, 0.017 and 0.17. (a) v_0, (b) h_0.

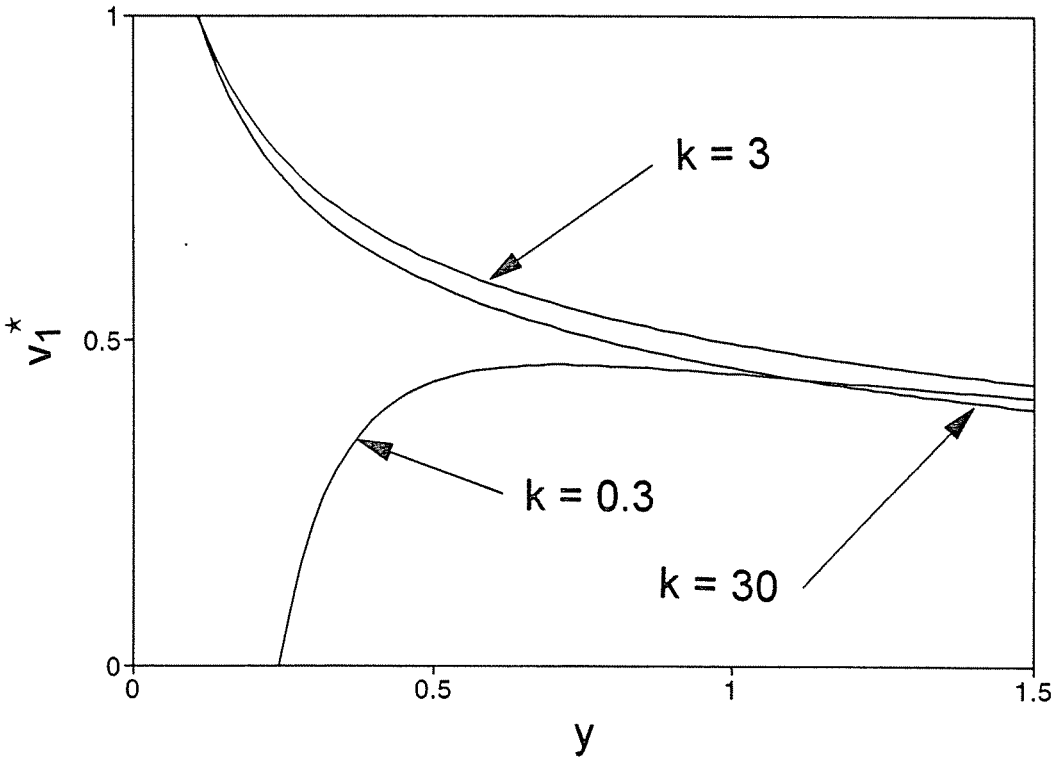

Figure 4–7. Profile of $v_1^\star$ for the cases k = 0.3, 3 and 30, F = 0.5, ψ = 0.017, and ϵ = 0.00017.

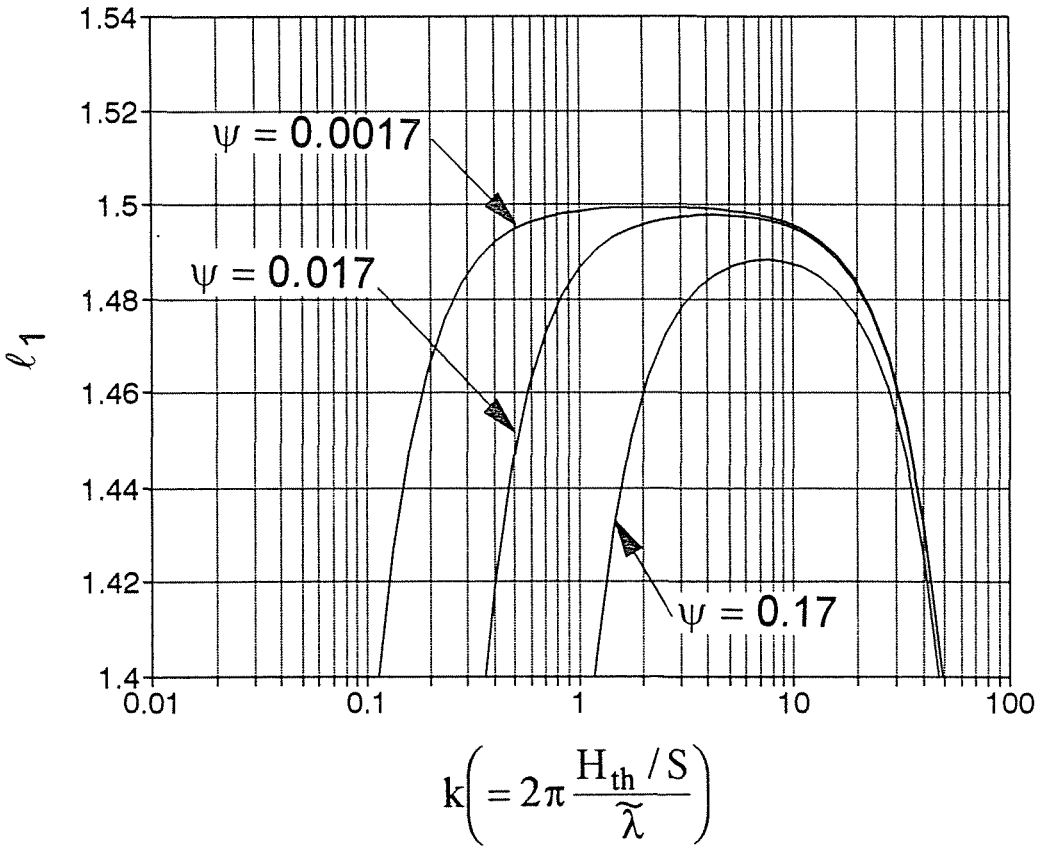

Figure 4–8. Perturbed threshold distance ℓ_1 versus k and ψ for the case F = 0.5 and ϵ = 0.00017.

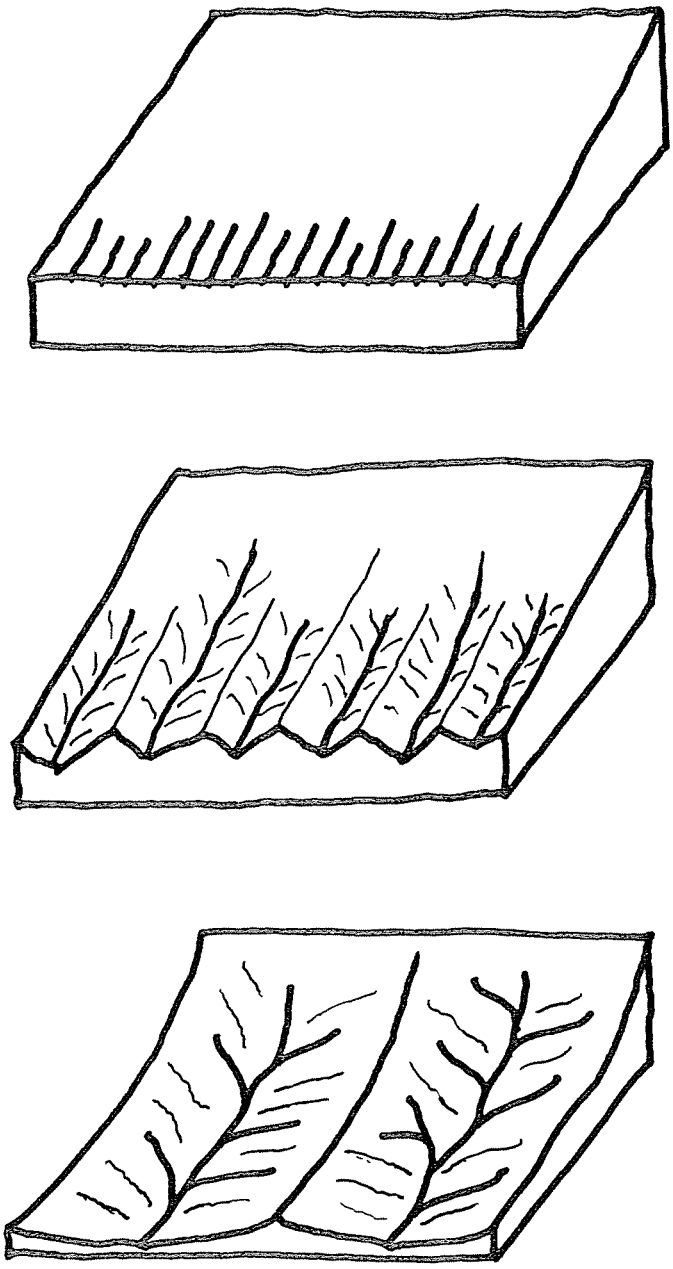

Figure 4–9. Schematic diagram showing long–time processes of drainage basin development.

5. DOWNSTREAM–DRIVEN CHANNEL INCEPTION USING A THRESHOLD HYPOTHESIS

5.1 Introduction

The downstream–driven analysis in the absence of rainfall of Chapter 3 did not lead to the selection of a finite wavelength of drainage basin spacing. Here that analysis of flow over a step is modified to include both rainfall and the threshold hypothesis of the previous chapter.

5.2 Conceptual model

Figure 5–1 shows a plateau composed of cohesive material which is flat, but which has a slight slope S in the $\tilde{y}$ direction. The downstream edge of the plateau terminates in a step–like overfall. It is assumed that uniform rainfall is supplied everywhere on the plateau, resulting in a sheet flow that increases in depth and velocity in the downstream direction, eventually cascading over the step. As noted in the figure, the $\tilde{y}$ coordinate is directed downstream, with its origin located at the divide, and the $\tilde{x}$ coordinate is taken to be perpendicular to it. The slope S is assumed to be low enough that the flow is subcritical in the Froude sense.

Due to uniform rainfall, the flow discharge increases linearly in the downstream direction. As a result, bed shear stress increases in the downstream direction and finally reaches the threshold condition, where erosion starts to occur on the surface of the plateau. Only the case for which the threshold is reached before the flow cascades over the step is considered here.

The edge of such a step as seen in nature can never be expected to be

straight. The irregular shape of the edge can be described by the superposition of Fourier modes with various wavenumbers. At least at the linear level, this fact allows the solution of the flow upstream of an irregular step to be described by the superposition of solutions upstream of sinuous steps with various wavenumbers. Here the flow solution for a sinuous step with specified wavenumber is obtained.

It is assumed that a small perturbation is given to an otherwise straight step, so that its edge is described by the following relation;

$$\tilde{y} = L_B - \tilde{a} \cos \tilde{k}\tilde{x}. \qquad (5\text{–}1)$$

Here L_B is basin length shown in Figure 5–1, and $\tilde{a}$ and $\tilde{k}$ denote the amplitude and wavenumber of the perturbation, respectively. In the present linear analysis, this amplitude is assumed to be infinitesimally small. In the case of subcritical overland flow, the indentations should act to attract the flow, causing a gathering of streamlines. The protuberances should result in a commensurate repulsion of the flow. As a result, boundary shear stress in the vicinity of the overfall can be expected to be intensified near the indentations and reduced near the protuberances.

It is assumed here that downstream–driven channel inception follows the scenario similar to that in the upstream–driven case. Once channels are formed, each channel gathers more and more water, preventing other channels from being formed nearby. The first channel heads to form will tend to dominate on the plateau, at least in the early stages of development. In other words, the channels formed in the shortest distance downstream from the divide are assumed to dominate on the plateau.

The transverse distance between each drainage basin is given by the spacing

of the channels, which corresponds to the wavelength $\tilde{\lambda}$ of the perturbation (5–1). This is illustrated in Figure 5–1.

The main goal of the present analysis is the prediction of the distance $\tilde{\lambda}$ between adjacent drainage basins in terms of the proposed threshold hypothesis. There should exist a relation between the wavelength of the perturbation (5–1) and the distance downstream of the divide where erosion first begins. If there exists a specific wavelength at which the distance from the divide to the threshold point is minimized, channels with that wavelength should tend to dominate, at least in the initial stages of development.

5.3 Formulation

5.3.1 Governing relations

In accordance with Figure 5–1, it is assumed that a flat plateau has a slight slope S descending in the positive $\tilde{y}$ direction. Bed elevation in excess of that of the upstream end can be expressed as

$$\tilde{\eta}_b = -S\tilde{y}. \tag{5–2}$$

Note that as appeared to the analysis of Chapter 3, the bed is assumed to be perfectly flat upstream of the wavy step. In the present case, the backwater effect is much larger than the Reynolds stress, especially, in the vicinity of the overfall. The Reynolds stress terms are thus neglected in this analysis. Equations (2–20) and (2–21) then take the forms

$$\tilde{u}\frac{\partial\tilde{u}}{\partial\tilde{x}} + \tilde{v}\frac{\partial\tilde{u}}{\partial\tilde{y}} = -g\frac{\partial\tilde{h}}{\partial\tilde{x}} - \frac{C_f\sqrt{\tilde{u}^2+\tilde{v}^2}}{\tilde{h}}\tilde{u}, \tag{5–3}$$

$$\tilde{u}\frac{\partial\tilde{v}}{\partial\tilde{x}} + \tilde{v}\frac{\partial\tilde{v}}{\partial\tilde{y}} = -g\frac{\partial\tilde{h}}{\partial\tilde{y}} + gS - \frac{C_f\sqrt{\tilde{u}^2+\tilde{v}^2}}{\tilde{h}}\tilde{v}, \tag{5–4}$$

$$\frac{\partial\tilde{u}\tilde{h}}{\partial\tilde{x}} + \frac{\partial\tilde{v}\tilde{h}}{\partial\tilde{y}} = I. \tag{5–5}$$

The streamwise discharge per unit width is taken to vanish at the divide; that is

$$\tilde{v}\tilde{h} = 0 \text{ at } \tilde{y} = 0. \tag{5–6}$$

The transverse velocity is taken to vanish there as well; that is

$$\tilde{u} = 0 \text{ at } \tilde{y} = 0. \tag{5–7}$$

The flow is assumed to be subcritical everywhere over the flow domain. The following boundary condition, corresponding to critical flow in the Froude sense, is applied at the sinusoidal step at the downstream end:

$$\frac{\tilde{u}_n^2}{g\tilde{h}} = 1 \text{ at } \tilde{y} = L_B - \tilde{a}\cos\tilde{k}\tilde{x}, \tag{5–8}$$

where $\tilde{u}_n$ is the component of velocity normal to the step.

The following dimensionless parameters are introduced;

$$(\tilde{u}, \tilde{v}) = V_0(u', v'), \quad \tilde{h} = H_0 h, \quad \tilde{x} = (H_0/S)x, \qquad (5\text{–}9a, b\ c)$$

$$(\tilde{y}, \tilde{a}) = L_B(y, a), \quad \tilde{k} = (H_0/S)^{-1}k, \qquad (5\text{–}9c, d)$$

where V_0 and H_0 are velocity and depth at the point of overfall in the absence of any perturbation ($\tilde{a} = 0$).

Using the above normalizations, the governing equations reduce to

$$u'\frac{\partial u'}{\partial x} + \psi v'\frac{\partial u'}{\partial y} = -\frac{\partial h}{\partial x} - C_s\frac{\sqrt{u'^2 + v'^2}}{h}u', \qquad (5\text{–}10)$$

$$u'\frac{\partial v'}{\partial x} + \psi v'\frac{\partial v'}{\partial y} = -\psi\frac{\partial h}{\partial y} + 1 - C_s\frac{\sqrt{u'^2 + v'^2}}{h}v', \qquad (5\text{–}11)$$

$$\frac{\partial u' h}{\partial x} + \psi\frac{\partial v' h}{\partial y} = \psi, \qquad (5\text{–}12)$$

where the dimensionless parameter C_s is given by

$$C_s = \frac{C_f}{S} = F^{-2}, \qquad (5\text{–}13)$$

and the dimensionless parameter ψ is defined by

$$\psi = \frac{H_0}{SL_B}. \qquad (5\text{–}14)$$

Here H_0 is taken to be much smaller than SL_B, allowing ψ to be used as a small parameter in this analysis. The justification for this is illustrated in Figure 5–2, it is identical to the reasoning used in Chapter 4. As seen in (5–10), (5–11) and (5–12), ψ appears as a multiplier on the terms associated with streamwise backwater effects. This implies that ψ provides a measure of the strength of streamwise backwater effects.

Here it is useful to specify appropriate boundary and integral conditions on the problem. Equations (5–6) and (5–7) can be rewritten in dimensionless form as

$$u' = 0,\ \hat{vh} = 0 \text{ at } y = 0. \qquad (5\text{–}15a, b)$$

The condition of no water transfer between adjacent basins leads to the boundary condition

$$u' = 0 \text{ at } x = 0, \pm \frac{\pi}{k}, \pm 2\frac{\pi}{k}, \ldots. \qquad (5\text{–}16)$$

Equation (5–12) can be integrated over one wavelength from $x = -\pi/k$ to $x = \pi/k$ and reduced with (5–15) and (5–16) to yield the following result:

$$\int_{-\pi/k}^{\pi/k} \hat{vh}\, dx = 2\frac{\pi}{k} y. \qquad (5\text{–}17)$$

Finally, (5–8) can be rewritten in dimensionless form as

$$(u'\sin\theta + v'\cos\theta)^2 = h \text{ at } y = y_e, \qquad (5\text{–}18a)$$

where

$$\sin\theta = \frac{dy_e/dx}{\sqrt{1 + (dy_e/dx)^2}}, \quad \cos\theta = \frac{1}{\sqrt{1 + (dy_e/dx)^2}}, \qquad (5\text{–}18b, c)$$

$$y_e = 1 - a\cos kx. \qquad (5\text{–}18d)$$

6.4 Solution

6.4.1 Solution in the outer region

When terms of $O(\psi)$ are dropped, (5–10), (5–11) and (5–12) reduce to

$$u'\frac{\partial u'}{\partial x} = -\frac{\partial h}{\partial x} - C_s\frac{\sqrt{u'^2 + v'^2}}{h}u', \qquad (5\text{–}19)$$

$$u'\frac{\partial v'}{\partial x} = 1 - C_s\frac{\sqrt{u'^2 + v'^2}}{h}v', \qquad (5\text{–}20)$$

$$\frac{\partial u'h}{\partial x} = 0. \qquad (5\text{–}21)$$

Integration of (5–21) with the use of (5–16) yields

$$u' = 0. \qquad (5\text{–}22)$$

This result implies that u' has the magnitude not larger than the order of ψ. With this in mind, the following renormalization is introduced:

$$u' = \psi u''. \tag{5–23}$$

This allows the equations to be rescaled as

$$\psi^2 u'' \frac{\partial u''}{\partial x} + \psi^2 v' \frac{\partial u''}{\partial y} = -\frac{\partial h}{\partial x} - \psi C_s \frac{\sqrt{\psi^2 u''^2 + v'^2}}{h} u'', \tag{5–24}$$

$$\psi u'' \frac{\partial v'}{\partial x} + \psi v' \frac{\partial v'}{\partial y} = -\psi \frac{\partial h}{\partial y} + 1 - C_s \frac{\sqrt{\psi^2 u''^2 + v'^2}}{h} v', \tag{5–25}$$

$$\psi \frac{\partial u'' h}{\partial x} + \psi \frac{\partial v' h}{\partial y} = \psi. \tag{5–26}$$

Dropping terms smaller than $O(1)$, the governing equations take the form

$$-\frac{\partial h}{\partial x} = 0, \tag{5–27}$$

$$1 = C_s \frac{v'^2}{h}, \tag{5–28}$$

$$\frac{\partial u'' h}{\partial x} + \frac{\partial v' h}{\partial y} = 1. \tag{5–29}$$

The following expansions are introduced:

$$u'' = a u_1'' + \ldots., \tag{5–30a}$$

$$v' = v_0' + a v_1' + \ldots., \tag{5–30b}$$

$$h = h_0 + ah_1 + \ldots\ldots \tag{5–30c}$$

Substitution of (5–30) into (5–27), (5–28) and (5–29) yields the following equations at $O(1)$:

$$1 = C_s \frac{v_0'^2}{h_0}, \tag{5–31}$$

$$\frac{\partial v_0' h_0}{\partial y} = 1, \tag{5–32}$$

with the boundary conditions

$$v_0' h_0 = 0 \text{ at } y = 0, \tag{5–33}$$

$$v_0^2 = h_0 = 1 \text{ at } y = 1. \tag{5–34}$$

Integration of (5–32) with the use of (5–33) yields the result

$$v_0' h_0 = y. \tag{5–35}$$

Between (5–31) and (5–35), the following solutions are obtained:

$$v_0' = C_s^{-1/3} y^{1/3}, \tag{5–36}$$

$$h_0 = C_s^{1/3} y^{2/3}. \tag{5–37}$$

These results should already be familiar as the base normal flow of Chapter 4.

At the next order, $O(a)$, the governing equations yield the following forms:

$$-\frac{\partial h_1}{\partial x} = 0, \tag{5–38}$$

$$2C_s \frac{v_0'}{h_0} v_1' - C_s \left(\frac{v_0'}{h_0} \right)^2 h_1 = 0, \tag{5–39}$$

$$\frac{\partial u_1''}{\partial x} h_0 + \frac{\partial v_1' h_0}{\partial y} + \frac{\partial v_0' h_1}{\partial y} = 0, \tag{5–40}$$

with the boundary conditions

$$u_1'' = 0, \quad v_0' h_1 + v_1' h_0 = 0 \quad \text{at } y = 0, \tag{5–41a, b}$$

$$u_1'' = 0 \quad \text{at } x = 0, \pm \frac{\pi}{k}, 2\frac{\pi}{k}, \ldots, \tag{5–42}$$

$$2v_1' = h_1 \text{ at } y = 1 - a \cos kx, \tag{5–43}$$

and the integral condition

$$\int_{-\pi/k}^{\pi/k} (v_0' h_1 + v_1' h_0)\, dx = 0. \tag{5–44}$$

Equation (5–38) can be integrated to yield

$$h_1 = f_0(y). \tag{5–45a}$$

Here $f_0(y)$ is a free function of y. Substituting (5–45a) into (5–39), v_1' is found to take the form

$$v_1' = \frac{1}{2} C_s^{-2/3} y'^{-1/3} f_0(y). \qquad (5–46a)$$

Substituting (5–36), (5–37), (5–45a) and (5–46a) into (5–44), it is found that $f_0(y)$ vanishes. Then the following solutions are obtained:

$$v_1' = 0, \quad h_1 = 0. \qquad (5–45b, 46b)$$

Substituting (5–36), (5–37), (5–45b) and (5–46b) into (5–40), and applying (5–42a), u_1'' is also found to vanish; that is

$$u_1'' = 0. \qquad (5–47)$$

While the boundary condition (5–33) is satisfied with the solution (5–36) and (5–37), (5–34) cannot be satisfied. Obviously, the neglect of terms smaller than $O(1)$ in (5–24), (5–25) and (5–26) is not valid in the vicinity of the step. Because of the abrupt change of velocity and depth of flow there, the neglected terms are not small. This fact implies the existence of two distinct regions, one of which is an outer region where (5–27), (5–28) and (5–29) are valid as the governing equations, the other of which is an inner region in the vicinity of the step where the gradients of velocity and depth are too large to be neglected. The solutions (5–36), (5–37), (5–45b), (5–46b) and (5–47) are seen to correspond to solutions in the outer region. As described in the subsequent section, outer, inner and intermediate layers

are defined in a context that differs from the above. In order to avoid confusion, the word "region" is distinguished from the word "layer" in the following way. The entire domain is first divided into the outer and inner regions. The inner region is then divided into the outer, intermediate and inner layers, as schematized in Figure 5–3.

The small parameter ψ is not employed as a formal parameter for perturbation analysis here. However, it should be noted that v_0' and h_0 are of the order of $a^0\psi^0$, u_1', v_1' and h_1 are of the order of $a^1\psi^0$, and u_1'' is of the order of $a^1\psi^1$. Since our concern here is how the perturbation provided at the downstream step affects on the flow upstream, terms of the order of $a^0\psi^1$ independent of the wavenumber k are not computed here.

5.4.2 Solution in the inner region

In the inner region near the overfall, the following inner variable is introduced:

$$y' = \frac{1 - y}{\psi}. \tag{5–48}$$

Substituting (5–48) into (5–10), (5–11) and (5–12), the governing equations in the inner region take the form

$$u'\frac{\partial u'}{\partial x} - v'\frac{\partial u'}{\partial y'} = -\frac{\partial h}{\partial x} - C_s\frac{\sqrt{u'^2 + v'^2}}{h}u', \tag{5–49}$$

$$u'\frac{\partial v'}{\partial x} - v'\frac{\partial v'}{\partial y'} = \frac{\partial h}{\partial y'} + 1 - C_s\frac{\sqrt{u'^2 + v'^2}}{h}v', \tag{5–50}$$

$$\frac{\partial u'h}{\partial x} - \frac{\partial v'h}{\partial y'} = \psi. \tag{5–51}$$

If terms smaller than $O(1)$ are neglected again, the right hand side of (5–51) may be dropped; that is

$$\frac{\partial u'h}{\partial x} - \frac{\partial v'h}{\partial y'} = 0. \tag{5–52}$$

Equations (5–49), (5–50) and (5–52) are familiar because they are very similar to the governing equations used in Chapter 3. Note the lack of rainfall source term in (5–52). The implication is that the inner region is sufficiently thin compared to the length of the basin that the rainfall source term can be neglected. In other words, the effect of rainfall is of the order of ψ in the thin region near the downstream step and the governing equations are reduced to those for the flow without rainfall by dropping terms of $O(\psi)$. Solutions up to the order of ψ^0 are obtained here, using the same strategy as in Chapter 3. As described in the previous section, terms of the order of $a^0\psi^1$ have no dependency on the wavenumber k of perturbation; they add some correction to the base state solutions. Since the main purpose of this analysis is to obtain the relation between the wavenumber k and the flow intensification caused by the perturbation, terms of the order of $a^0\psi^1$ are not computed here.

The strategy used to derive the solutions in the inner region is substantially identical to that used in Chapter 3. Therefore, only a brief explanation is provided below.

a) Transformation

It is once again convenient to employ the conformal transformation used in Chapter 3. The transformed coordinates are illustrated in Figure 3–8. The transformation is expressed as

$$x = \xi - ae^{-k\eta}\sin k\xi, \quad y' = \eta + ae^{-k\eta}\cos k\xi. \qquad (5\text{–}53a, b)$$

The Jacobian of the transformation is

$$J = \frac{\partial(x,\ y)}{\partial(\xi,\ \eta)} = 1 - 2ake^{-k\eta}\cos k\xi + (ak)^2 e^{-2k\eta}. \qquad (5\text{–}53c)$$

The equations of motion written in the transformed plane now take the form

$$\frac{u}{J^{1/2}}\frac{\partial u}{\partial \xi} - \frac{v}{J^{1/2}}\frac{\partial u}{\partial \eta} - \frac{uv}{J}\frac{\partial J^{1/2}}{\partial \eta} - \frac{v^2}{J}\frac{\partial J^{1/2}}{\partial \xi}$$

$$= -\frac{1}{J^{1/2}}\frac{\partial h}{\partial \xi} + \frac{ake^{-k\eta}\sin\ k\xi}{J^{1/2}} - C_s\frac{\sqrt{u^2 + v^2}}{h}u, \qquad (5\text{–}54)$$

$$\frac{u}{J^{1/2}}\frac{\partial v}{\partial \xi} - \frac{v}{J^{1/2}}\frac{\partial v}{\partial \eta} + \frac{uv}{J}\frac{\partial J^{1/2}}{\partial \xi} + \frac{u^2}{J}\frac{\partial J^{1/2}}{\partial \eta}$$

$$= \frac{\delta}{J^{1/2}}\frac{\partial h}{\partial \eta} + \frac{1 - ake^{-k\eta}\cos\ k\xi}{J^{1/2}} - C_s\frac{\sqrt{u^2 + v^2}}{h}v, \qquad (5\text{–}55)$$

$$\frac{\partial(J^{1/2}uh)}{\partial \xi} - \frac{\partial(J^{1/2}vh)}{\partial \eta} = 0. \qquad (5\text{–}56)$$

where u and v are the velocities in the ξ and η directions, respectively.

Here a is taken as a small parameter; the following expansions in powers of a are introduced:

$$u = au_1 + a^2u_2 + ..., \tag{5–57a}$$

$$v = v_0 + av_1 + a^2v_2 + ..., \tag{5–57b}$$

$$h = h_0 + ah_1 + a^2h_2 + ... \tag{5–57c}$$

At leading order, i.e. $O(a^0)$, (5–55) and (5–56) give

$$-v_0\frac{dv_0}{d\eta} - \frac{dh_0}{d\eta} = 1 - C_s\frac{v_0^2}{h_0}, \tag{5–58}$$

$$\frac{dv_0h_0}{d\eta} = 0. \tag{5–59}$$

For the subcritical flow considered here, (5–58) and (5–59) describe a simple M2 backwater curve. Since $v_0 = h_0 = 1$ at the step, (5–59) can be integrated to yield

$$v_0h_0 = 1. \tag{5–60}$$

Between (5–58) and (5–60), the following ordinary differential equation for v_0 is obtained:

$$\frac{dv_0}{d\eta} = -\frac{C_s v_0^3 - 1}{v_0^{-2} - v_0}. \tag{5–61}$$

This describes the base flow in the absence of perturbations.

At the next order, $O(a)$, the governing equations give

$$-v_0 \frac{\partial u_1}{\partial \eta} - k^2 v_0^2 e^{-k\eta} \sin k\xi + \frac{\partial h_1}{\partial \xi} = k e^{-k\eta} \sin k\xi - C_s \frac{v_0}{h_0} u_1, \tag{5–62}$$

$$-v_0 \frac{\partial v_1}{\partial \eta} - v_1 \frac{\partial v_0}{\partial \eta} - k v_0 \frac{\partial v_0}{\partial \eta} e^{-k\eta} \cos k\xi - \frac{\partial h_1}{\partial \eta} - k \frac{\partial h_0}{\partial \eta} e^{-k\eta} \cos k\xi = -2C_s \frac{v_0}{h_0} v_1 + C_s \left(\frac{v_0}{h_0} \right)^2 h_1, \tag{5–63}$$

$$k h_0 \frac{\partial u_1}{\partial \xi} - h_0 \frac{\partial v_1}{\partial \eta} - h_1 \frac{\partial v_0}{\partial \eta} - v_0 \frac{\partial h_1}{\partial \eta} - v_1 \frac{\partial h_0}{\partial \eta} + k \frac{\partial v_0 h_0}{\partial \eta} e^{-k\eta} \cos k\xi = 0. \tag{5–64}$$

The first order equations (5–62) ~ (5–64) admit solutions of the form

$$u_1 = u_1^\star(\eta) \sin k\xi, \quad v_1 = v_1^\star(\eta) \cos k\xi, \tag{5–65a, b}$$

$$h_1 = h_1^\star(\eta) \cos k\xi. \tag{5–65c}$$

Substituting (5–65) into (5–62), (5–63) and (5–64), and reducing with the aid of (5–58) and (5–60), the following equations are obtained:

$$\frac{du_1^\star}{d\eta} = C_s v_0 u_1^\star - \frac{k}{v_0} h_1^\star - \left(k^2 v_0 + \frac{k}{v_0} \right) e^{-k\eta}, \tag{5–66}$$

$$\frac{dv_1^\star}{d\eta} = -\frac{k}{v_0(v_0^2 - v_0^{-1})} u_1^\star - \frac{v_0 \frac{dv_0}{d\eta} - 2C_s v_0^3 + v_0^{-2}\frac{dv_0}{d\eta}}{v_0^2 - v_0^{-1}} v_1^\star$$
$$- \frac{C_s v_0^5 - \frac{dv_0}{d\eta}}{v_0^2 - v_0^{-1}} h_1^\star - \frac{kC_s v_0^4 - kv_0 - k^2}{v_0^2 - v_0^{-1}} e^{-k\eta}, \tag{5–67}$$

$$\frac{dh_1^\star}{d\eta} = \frac{k}{v_0^2 - v_0^{-1}} u_1^\star + \frac{2v_0^{-1}\frac{dv_0}{d\eta} - 2C_s v_0}{v_0^2 - v_0^{-1}} v_1^\star$$
$$+ \frac{C_s v_0^3 - v_0 \frac{dv_0}{d\eta}}{v_0^2 - v_0^{-1}} h_1^\star + \frac{kC_s v_0^2 - kv_0^{-1} - k^2 v_0}{v_0^2 - v_0^{-1}} e^{-k\eta}. \tag{5–68}$$

Equations (5–66), (5–67) and (5–68) can be written in compact matrix form as

$$\frac{d\boldsymbol{u}}{d\eta} = \underset{\sim}{\mathscr{L}}(\eta)\,\boldsymbol{u} + \boldsymbol{m}(\eta)e^{-k\eta} \tag{5–69a}$$

where

$$\boldsymbol{u} = \begin{bmatrix} u_1^\star \\ v_1^\star \\ h_1^\star \end{bmatrix}, \tag{5–69b}$$

$$\underset{\sim}{\mathscr{L}}(\eta) = \begin{bmatrix} L_{11} & L_{12} & L_{13} \\ L_{21} & L_{22} & L_{23} \\ L_{31} & L_{32} & L_{33} \end{bmatrix}, \tag{5–69c}$$

$$L_{11} = C_s v_0,\ L_{12} = 0,\ L_{13} = -\frac{k}{v_0},\ L_{21} = -\frac{k}{v_0(v_0^2 - v_0^{-1})},$$

$$L_{22} = -\frac{v_0\frac{dv_0}{d\eta} - 2C_s v_0^3 - v_0^{-2}\frac{dv_0}{d\eta}}{v_0^2 - v_0^{-1}},\ L_{23} = -\frac{C_s v_0^5 - \frac{dv_0}{d\eta}}{v_0^2 - v_0^{-1}},$$

$$L_{31} = \frac{k}{v_0^2 - v_0^{-1}},\ L_{32} = \frac{2v_0^{-1}\frac{dv_0}{d\eta} - 2C_s v_0}{v_0^2 - v_0^{-1}},\ L_{33} = \frac{C_s v_0^3 - v_0\frac{dv_0}{d\eta}}{v_0^2 - v_0^{-1}},$$

and

$$\underset{\sim}{m}(\eta) = \begin{bmatrix} m_1 \\ m_2 \\ m_3 \end{bmatrix}, \tag{5–69d}$$

$$m_1 = -\left(k^2 v_0 + \frac{k}{v_0}\right),\ m_2 = -\frac{kC_s v_0^4 - kv_0 - k^2}{v_0^2 - v_0^{-1}},$$

$$m_3 = \frac{kC_s v_0^2 - kv_0^{-1} - k^2 v_0^3}{v_0^2 - v_0^{-1}}.$$

Note that $\underset{\sim}{\mathscr{L}}(\eta)$ and $\underset{\sim}{m}(\eta)$ are functions of η via the parameter v_0 and its first derivative.

b) Solution in the outer layer.

As shown in figure 5–3, the inner region, which corresponds to a zone near the overfall, is further divided into three layers. The inner layer is an extremely thin zone near the edge, at which singularities appear in the derivatives of v and h. The outer layer is a much larger zone of near–normal flow, the deviations from which are modest. The inner and outer solutions are joined in the intermediate zone. This treatment is completely analogous to that of Chapter 3.

The outer layer is attained as η approaches infinity, at which v_0 approaches $C_s^{1/3}$ and $dv_0/d\eta$ approaches 0. In the outer layer, then, the governing equations reduce to

$$\frac{d\,\boldsymbol{u}^{o}}{d\eta} = \mathcal{A}^{o}\,\boldsymbol{u} + \boldsymbol{m}^{o}e^{-k\eta}, \tag{5–70a}$$

where

$$\mathcal{A}^{o} = \begin{bmatrix} C_s^{2/3} & 0 & -C_s^{1/3} \\ -\dfrac{kC_s}{1-C_s} & \dfrac{2C_s^{2/3}}{1-C_s} & -\dfrac{1}{1-C_s} \\ \dfrac{kC_s^{2/3}}{1-C_s} & -\dfrac{2C_s^{4/3}}{1-C_s} & \dfrac{C_s^{2/3}}{1-C_s} \end{bmatrix}. \tag{5–70b}$$

and

$$\boldsymbol{m}^{o} = \begin{bmatrix} -(k^2C_s^{-1/3} + kC_s^{1/3}) \\ \dfrac{k^2C_s^{2/3}}{1-C_s} \\ -\dfrac{k^2C_s^{1/3}}{1-C_s} \end{bmatrix}, \tag{5–70c}$$

Solving the above differential system, the following solution is obtained:

$$\omega^0 = A_0 \begin{bmatrix} \dfrac{kC_s^{1/3}}{C_s^{2/3} - \lambda_1} \\ \dfrac{1 + C_s^{1/3}\lambda_1}{2C_s^{2/3} - \lambda_1} \\ 1 \end{bmatrix} e^{-\lambda_1 \eta} + \begin{bmatrix} kC_s^{1/3} \\ 0 \\ 0 \end{bmatrix} e^{-k\eta} \qquad (5\text{–}71)$$

Here λ_1 is a negative real root of the following equation:

$$(C_s - 1)\lambda_n^3 + C_s^{2/3}(4 - C_s)\lambda_n^2 - C_s(k^2 + 3C_s^{1/3})\lambda_n + 2k^2 C_s^{5/3} = 0. \qquad (5\text{–}72)$$

c) Solution in the inner layer

In the inner layer, then, η is renormalized as

$$\eta^* = \delta^{-1}\eta. \qquad (5\text{–}73)$$

where δ is a small parameter appropriate to capture the singularity of the edge. The governing equations (5–54) ~ (5–56) thus take the form

$$F^2\left(\delta \frac{u}{J^{1/2}} \frac{\partial u}{\partial \xi} - \frac{v}{J^{1/2}} \frac{\partial u}{\partial \eta^*} - \frac{uv}{J} \frac{\partial J^{1/2}}{\partial \eta^*} - \delta \frac{v^2}{J} \frac{\partial J^{1/2}}{\partial \xi} \right)$$

$$= -\delta \frac{1}{J^{1/2}} \frac{\partial h}{\partial \xi} + \delta \left(\frac{ake^{-\delta k \eta^*} \sin k\xi}{J^{1/2}} - \frac{\sqrt{u^2 + v^2}}{h} u \right), \qquad (5\text{–}74)$$

$$F^2\left(\delta \frac{u}{J^{1/2}} \frac{\partial v}{\partial \xi} - \frac{v}{J^{1/2}} \frac{\partial v}{\partial \eta^*} + \delta \frac{uv}{J} \frac{\partial J^{1/2}}{\partial \xi} + \frac{u^2}{J} \frac{\partial J^{1/2}}{\partial \eta^*} \right)$$

$$= \frac{1}{J^{1/2}} \frac{\partial h}{\partial \eta^*} + \delta \left(\frac{1 - ake^{-\delta k \eta^*} \cos k\xi}{J^{1/2}} - \frac{\sqrt{u^2 + v^2}}{h} v \right), \qquad (5\text{–}75)$$

$$\delta \frac{\partial (J^{1/2} u\ h)}{\partial \xi} - \frac{\partial (J^{1/2} v\ h)}{\partial \eta^*} = 0. \qquad (5\text{–}76)$$

where

$$J = 1 - 2ak \cos k\xi\ (1 - k\delta\eta^* + ...) + (ak)^2 (1 - 2k\delta\eta^* + ...)$$

$$= 1 - ak \cos k\xi + (ak)^2 + \delta\,(2ak^2 \cos \xi - 2a^2 k^3)\eta^* + O(\delta^2), \qquad (5\text{–}77)$$

The following expansions are introduced:

$$u = a u_{10}(\xi) + a\delta^{1/2} u_{11}(\xi, \eta^*) + ..., \qquad (5\text{–}78a)$$

$$v = 1 + a v_{10}(\xi) + \delta^{1/2} v_{01}(\eta^*) + a\delta^{1/2} v_{11}(\xi, \eta^*) + ..., \qquad (5\text{–}78b)$$

$$h = 1 + a h_{10}(\xi) + \delta^{1/2} h_{01}(\eta^*) + a\delta^{1/2} h_{11}(\xi, \eta^*) + ... \qquad (5\text{–}78c)$$

Substituting (5–78) into (5–74), (5–75) and (5–76), and after manipulations similar to those performed in Chapter 3, the following solutions are obtained as the final form:

$$u = aA_1 \sin k\xi, \tag{5–79a}$$

$$v = 1 - M\eta^{1/2} + aA_2 \cos k\xi + ..., \tag{5–79b}$$

$$h = 1 + M\eta^{1/2} + 2aA_2 \cos k\xi + ..., \tag{5–79c}$$

where

$$M = \left[\frac{2}{3} (C_s - 1) \right]^{1/2}. \tag{5–79d}$$

d) Solution in the intermediate layer

The full differential system (5–69) is then solved numerically in the intermediate layer. The outer solution contains the one free constant A_0, which provides the basis for a shooting method. A guess for the value of A_0 is made; the Runge–Kutta method is then used to step the solution downstream of the point η_i of matching with the outer solution. Here the point η_i defining the interface between the outer and intermediate layer can then be defined such that v_0 is sufficiently close to unity. At the point $\eta = \delta$, matching with the inner solution is performed. In particular, the parameters A_1 and A_2 are estimated as

$$A_1 = u_1^{\star}(\eta, A_0)|_{\eta=\delta} \tag{5–80a}$$

$$A_2 = v_1^{\star}(\eta, A_0)|_{\eta=\delta} \tag{5–80b}$$

$$2A_2 = h_1^{\star}(\eta, A_0)|_{\eta=\delta} \tag{5–80c}$$

A Newton–Raphson technique is used to improve the successive guesses for A_0. The method is continued until all three unknown constants A_0, A_1, and A_2 are successfully evaluated.

5.4.3 Composite solution

Let the variables in the outer and inner regions be denoted by the superscripts O and I, respectively. Composite solutions which are valid in both the outer and inner regions take the form

$$u = u^O + u^I - \lim_{y\to 1} u^O \ (\text{or} \lim_{\eta\to\infty} u^I), \tag{5–81}$$

$$v = v^O + v^I - \lim_{y\to 1} v^O \ (\text{or} \lim_{\eta\to\infty} v^I) \tag{5–82}$$

$$h = h^O + h^I - \lim_{y\to 1} h^O \ (\text{or} \lim_{\eta\to\infty} h^I) \tag{5–83}$$

where the outer solutions up to $O(a)$ are given as

$$u^O = 0 + O(\psi), \quad v^O = C_s^{-1/3} y^{1/3} + O(\psi), \tag{5–84a, b}$$

$$h^O = C_s^{1/3} y^{2/3} + O(\psi). \tag{5–84c}$$

Note that terms of $O(a)$ do not appear in the outer solutions. The inner solutions up to $O(a)$ take the form

$$u^I = a u_1^{*I}(\eta) \sin k\xi + O(\psi), \tag{5–85a}$$

$$v^I = v_0^I(\eta) + a v_1^{*I}(\eta) \cos k\xi + O(\psi), \tag{5–85b}$$

$$h^I = h_0^I(\eta) + a h_1^{*I}(\eta) \cos k\xi + O(\psi). \tag{5–85c}$$

where u_1^{*I}, v_0^I, v_1^{*I}, h_0^I and h_1^{*I} are solutions in the inner region obtained in 5.4.2.

Substituting $y = 1$ into (5–84) and taking the limit as $\eta \to \infty$ of (5–85), the following results are obtained:

$$\lim_{y \to 1} u^O = \lim_{\eta \to \infty} u^I = 0, \tag{5–86a}$$

$$\lim_{y \to 1} v^O = \lim_{\eta \to \infty} v^I = C_s^{-1/3}, \tag{5–86b}$$

$$\lim_{y \to 1} h^O = \lim_{\eta \to \infty} h^I = C_s^{1/3}. \tag{5–86c}$$

The outer solutions are written in the outer variable y and the inner solutions are written in the transformed, inner variable η. In order to obtain convenient forms for the solutions, it is necessary to unify these variables. Since the flow of concern here is in the vicinity of the step and coordinates of physical plane are more convenient to use, the non–transformed, the inner variable y' is used for

the common variable in both regions.

Equations (5–84a, b, c) are rewritten as

$$u^{O} = 0 + O(\psi^2), \tag{5–87a}$$

$$v^{O} = C_s^{-1/3}(1 - \psi y')^{1/3} + O(\psi), \tag{5–87b}$$

$$h^{O} = C_s^{1/3}(1 - \psi y')^{2/3} + O(\psi). \tag{5–87c}$$

Within the region $0 \leq y' \leq 1$, (5–87b, c) can be expanded in powers of ψ as follows:

$$v^{O} = C_s^{-1/3} - \frac{\psi}{3} C_s^{-1/3} y' + O(\psi), \tag{5–87d}$$

$$h^{O} = C_s^{1/3} - \psi \frac{2}{3} C_s^{1/3} y' + O(\psi). \tag{5–87e}$$

From (5–53), the following relations are obtained:

$$\xi = x + ae^{-ky'} \sin kx, \quad \eta = y' - ae^{-ky'} \cos kx. \tag{5–88a, b}$$

Substituting (5–88) and applying Taylor's expansion, the inner solutions can be rewritten as:

$$u^{I} = au_1^{\star I}(y') \sin kx + O(\psi), \tag{5–89a}$$

$$v^{I} = v_0^{I}(y') + a\left[v_1^{\star I}(y') - \frac{\partial v_0^{I}}{\partial y'} e^{-ky'} \right] \cos kx + O(\psi), \tag{5–89b}$$

$$h^I = h_0^I(y') + a\left[h_1^{\star I}(y') - \frac{\partial h_0^I}{\partial y'} e^{-ky'} \right] \cos kx + O(\psi). \qquad (5\text{–}89c)$$

Substituting (5–87) and (5–89) into (5–81) ~ (5–83), and using (5–86), the composite solutions are finally found to take the forms

$$u = a u_1^{\star I}(y') \sin kx + O(\psi), \qquad (5\text{–}90)$$

$$v = v_0^I(y') + a\left[v_1^{\star I}(y') - \frac{\partial v_0^I}{\partial y'} e^{-ky'} \right] \cos kx + O(\psi), \qquad (5\text{–}91)$$

$$h = h_0^I(y') + a\left[h_1^{\star I}(y') - \frac{\partial h_0^I}{\partial y'} e^{-ky'} \right] \cos kx + O(\psi). \qquad (5\text{–}92)$$

Because terms of $O(\psi)$ have no dependency on the wavenumber k of perturbation, they are dropped hereinafter.

5.5 Threshold hypothesis

According to the scenario of the threshold concept, the perturbation with the wavelength which minimizes the distance from the divide to the threshold point should dominate. This wavelength is called the characteristic wavelength associated with the threshold concept. To obtain the characteristic wavelength, the distance where the threshold condition is realized is related to the degree to which velocity is intensified by the overfall.

Bed shear stress τ is normalized as

$$\tilde{\tau} = \rho C_f V_0^2 \tau. \tag{5–93}$$

Dimensionless shear stress τ is then expanded in the small parameter a:

$$\tau = \tau_0 + a\tau_1 + O(a^2). \tag{5–94}$$

With the aid of (2–28) and (5–91), τ_0 and τ_1 are expressed by the relations

$$\tau_0 = [v_0^I(y')]^2, \tag{5–95}$$

$$\tau_1 = 2v_0^I(y')\left[v_1^{*I}(y') - \frac{\partial v_0^I}{\partial y'} e^{-ky'} \right] \cos kx. \tag{5–96}$$

Suppose that the threshold condition is realized at $y' = \ell$ as the result of the perturbation; that is

$$\tau(\ell) = \tau_{th}, \tag{5–97}$$

where $\tau_{th} = \tilde{\tau}_{th}/\rho C_f V_0^2$ and $\tilde{\tau}_{th}$ again denotes the threshold shear stress for bed erosion. The distance of the threshold point ℓ upstream from the base mode edge is expanded as

$$\ell = \ell_0 + a\ell_1 + O(a^2), \tag{5–98}$$

The location of the threshold point ℓ_0 in the absence of a perturbation is defined by the relation

$$\tau_0(\ell_0) = \tau_{th}. \tag{5–99}$$

The relation between ℓ_0 and τ_{th} can be found as follows. The inner solution of the base state $v_0^I(y')$ can be calculated using (5–61), which can be rewritten in the common variable y' and integrated to yield

$$\int_1^{v_0^I(y')} \frac{v_0 - v_0^{-2}}{C_s v_0^3 - 1}\, dv_0 = y'. \tag{5–100}$$

The parameter τ_0 can be evaluated from (5–95) and (5–100) with y' set equal to ℓ_0. With the aid of (5–99), it is found that

$$[v_0^I(\ell_0)]^2 = \tau_{th}, \tag{5–101a}$$

where

$$\int_1^{v_0^I(\ell_0)} \frac{v_0 - v_0^{-2}}{C_s v_0^3 - 1}\, dv_0 = \ell_0. \tag{5–101b}$$

The relation between ℓ_0 and τ_{th} is shown in Figure 5–4 for the cases $C_s = 4$ and 25.

Applying Taylor's expansion, the shear stress τ at $y = \ell$ up to the order of a is given by

$$\tau(\ell) = \tau_0(\ell_0) + a\ell_1 \left.\frac{\partial \tau_0}{\partial y}\right|_{y'=\ell_0} + a\tau_1(\ell_0). \tag{5–102}$$

Between (5–97), (5–99) and (5–102), the following relation is obtained:

$$\ell_1(x) = -\frac{\tau_1(\ell_0)}{\left.\frac{\partial \tau_0}{\partial y}\right|_{y'=\ell_0}} . \qquad (5\text{–}103)$$

With the use of (5–95) and (5–96), (5–103) can be written as

$$\ell_1(x) = \left[e^{-k\ell_0} - \frac{v_1^{*I}(\ell_0)}{\left.\frac{\partial v_0^I}{\partial y'}\right|_{y'=\ell_0}} \right] \cos kx. \qquad (5\text{–}104)$$

The parameter ℓ_1 is thus seen to be maximized when x = 0. It is seen from Figure 5–1 that the line x = 0 corresponds to the center of an indentation. Equation (5–104) thus implies that the distance ℓ is maximized along lines in the y' direction that originate at the center of indentations. The result is

$$\ell_1(0) = \left[e^{-k\ell_0} - \frac{v_1^{*I}(\ell_0)}{\left.\frac{\partial v_0^I}{\partial y'}\right|_{y'=\ell_0}} \right]. \qquad (5\text{–}105)$$

Now the distance $\ell_1(0)$ is measured upstream from the base mode edge. As shown in figure 5–1, maximum $\ell_1(0)$ corresponds to the minimum distance from divide to the point at which threshold conditions are reached. In analogy to Chapter 4, then, the characteristic wavenumber k_c is the one that maximizes $\ell_1(0)$.

Figure 5–5 shows ℓ_1 versus k and ℓ_0. The value of C_s (= $C_f/S = F^{-2}$) is

taken to be 4 in Figure 5–5a. It is found that ℓ_1 is maximized for k = 0.8 ~ 4 over the computed range. This corresponds to a characteristic wavelength $\tilde{\lambda}_c$ of the order of H_0/S. The figure also shows that while the absolute value of ℓ_1 decreases for larger values of ℓ_0, which corresponds to a threshold location farther from the edge, the characteristic wavenumber k_c increases as ℓ_0 increases. According to Figure 5–4, larger values of ℓ_0 correspond to smaller values of τ_{th}. Since when τ_{th} is small, the shear stress at the edge is much larger than the threshold value, it is found that a larger shear stress results in a smaller characteristic wavenumber k_c, i.e. a longer characteristic wavelength of drainage basin spacing.

The case $C_s = 25$ is depicted in Figure 5–5b. Comparing this figure with Figure 5–5a, for the same value of ℓ_0, it is seen that ℓ_1 is maximized at larger wavenumbers in this case than in the previous one. This implies that the characteristic wavelength decreases as either the Froude number or slope decreases. Roughly speaking, the magnitude of the inertial forces scales with the Froude number. It may be noted by way of explanation that a larger inertial force prevents flow from concentrating at small values of k.

The velocity V_0 and depth H_0 at the downstream step are related to the rainfall intensity I and the basin length L_B by the following continuity relation:

$$V_0 H_0 = I L_B. \tag{5–106}$$

The condition of a Froude number of unity at the downstream step yields the relation

$$V_0^2 = g H_0. \tag{5–107}$$

Between (5–106) and (5–107), V_0 and H_0 are obtained as

$$V_0 = (gIL_B)^{1/3}, \quad H_0 = g^{-1/3}(IL_B)^{2/3}. \qquad (5–108a, b)$$

The normalized threshold shear stress is then expressed as

$$\tau_{th} = \frac{\tilde{\tau}_{th}}{\rho C_f (gIL_B)^{2/3}} = \frac{u_{th}^{*2}}{C_f (gIL_B)^{2/3}}. \qquad (5–109)$$

The characteristic wavelength $\tilde{\lambda}_c$ can be obtained as follows. Specifying u_{th}^*, C_f, I and L_B, the normalized shear stress τ_{th} is calculated by (5–109). By further specifying S, C_s can be calculated, and the corresponding value of ℓ_0 can be obtained from (5–101). The characteristic wavenumber k_c can be calculated with the use of (5–105). Finally, the characteristic wavelength of drainage basin spacing is obtained from the following relation:

$$\tilde{\lambda}_c = 2\pi \frac{H_0}{k_c S}. \qquad (5–110)$$

In order to clarify the implications of the above result, it is useful to specify some possible values for u_{th}^*, C_f, I, L_B and S applicable to the present case. As noted in Chapter 4, the threshold shear velocity over cohesive soils varies from about 5 cm/s for sandy loam to about 15 cm/s for rigid clay. Here a value of 10 cm/s is taken for a sample calculation. A crude but reasonable estimate for C_f is 0.01 (Yoon et al., 1971; Shen et al., 1973). The rainfall intensity I is assumed to be 100 mm/hour; i.e. 2.78×10^{-5} m/s. The basin length L_B is assumed to be 7900 m.

The slope S is assumed to be 0.0025, corresponding to $C_s = 4$.

From these estimates, it is found from (5–108a, b) and (5–109) that $V_0 = 1.29$ m/s, $H_0 = 0.17$ m, $\psi = 8.61 \times 10^{-3}$ and $\tau_{th} = 0.6$. With the aid of Figure 5–4, the parameter ℓ_0 is found to take the value 0.05, so that the dimensional distance of the threshold point from the downstream step is 3.4 m. It is found from Figure 5–5a that $k_c = 0.8$. Using the relation (5–110), the characteristic wavelength of drainage basin spacing $\tilde{\lambda}_c$ is found to be 534 m.

In order to compare with the upstream–driven case analyzed in the previous chapter, the corresponding characteristic wavelength of drainage basin spacing predicted by the upstream–driven model for the same values of u^*_{th}, S, C_f, and I is calculated here. According to (4–129), $\tilde{\lambda}_c$ is found to be 188 m. In addition, with the use of (4–17c), L_{th} can be calculated to be 14700 m. The upstream–driven theory predicts a smaller characteristic wavelength than the downstream–driven theory. It is also found for this case that the upstream–driven process requires a longer basin length than the downstream–driven process. The downstream–driven process is characterized by the existence of a step at the downstream end, which accelerates the flow approaching the step. Because of this flow acceleration, the shear stress in the downstream–driven process can reach the threshold value in a shorter distance downstream of the divide than that for the upstream–driven process. This fact may allow for the following categorization by basin length of the three models presented in this study by basin length. If there is no step, the upstream–driven process should dominate. If the basin length is terminated by a step in a distance shorter than L_{th}, the downstream–driven process should dominate. If the dimensionless threshold shear stress is larger than unity ($\tau_{th} > 1$), which corresponds to the following criterion:

$$L_B < \frac{u_{th}^{*3}}{gI(\beta C_f)^{3/2}}, \qquad (5\text{–}111)$$

the shear stress everywhere on the plateau is below the threshold value, resulting in no erosion on the surface. If this is the case, only the step foot erosion model is applicable. The predicted characteristic wavelength would be infinitesimally small.

Categorization is also possible in terms of basin slope. If the basin slope S is smaller than the friction factor C_f, which corresponds to a Froude number less than unity, either the downstream–driven or upstream–driven process could dominate. If the basin slope S is larger than the friction factor C_f, the flow is supercritical and only the upstream–driven process can dominate.

5.6 Conclusions

The threshold hypothesis proposed in Chapter 4 has been applied to the process of downstream–driven channel inception. Although this problem was analyzed in Chapter 3 using the "step foot erosion model", here a model based on surface erosion is formulated.

It is found that the distance from the downstream step to the threshold point, ℓ_1 is maximized at wavenumber k = 0.1 ~ 10. This implies that the characteristic wavelength $\tilde{\lambda}_c$ is such that $S\tilde{\lambda}_c/H_0$ is in the range 0.1 ~ 10.

The characteristic wavenumber k_c maximizing ℓ_1 decreases as ℓ_0 increases or τ_{th} decreases. That is, if the shear stress at the downstream step increases, resulting in a longer distance from the downstream step threshold point, the characteristic wavelength $\tilde{\lambda}_c$ is correspondingly longer. The analysis predicts that a

larger Froude number corresponds to a longer characteristic wavelength $\tilde{\lambda}_c$.

It is found that the model of downstream–driven channel inception predicts a longer characteristic wavelength than the upstream–driven one.

It is suggested that the upstream–driven process should dominate when the basin length is sufficiently long or the basin slope is large enough for the flow to be supercritical. The downstream–driven process should dominate when the basin is terminated by a step in a distance shorter than L_{th}, and when the slope is small enough for the flow to be subcritical.

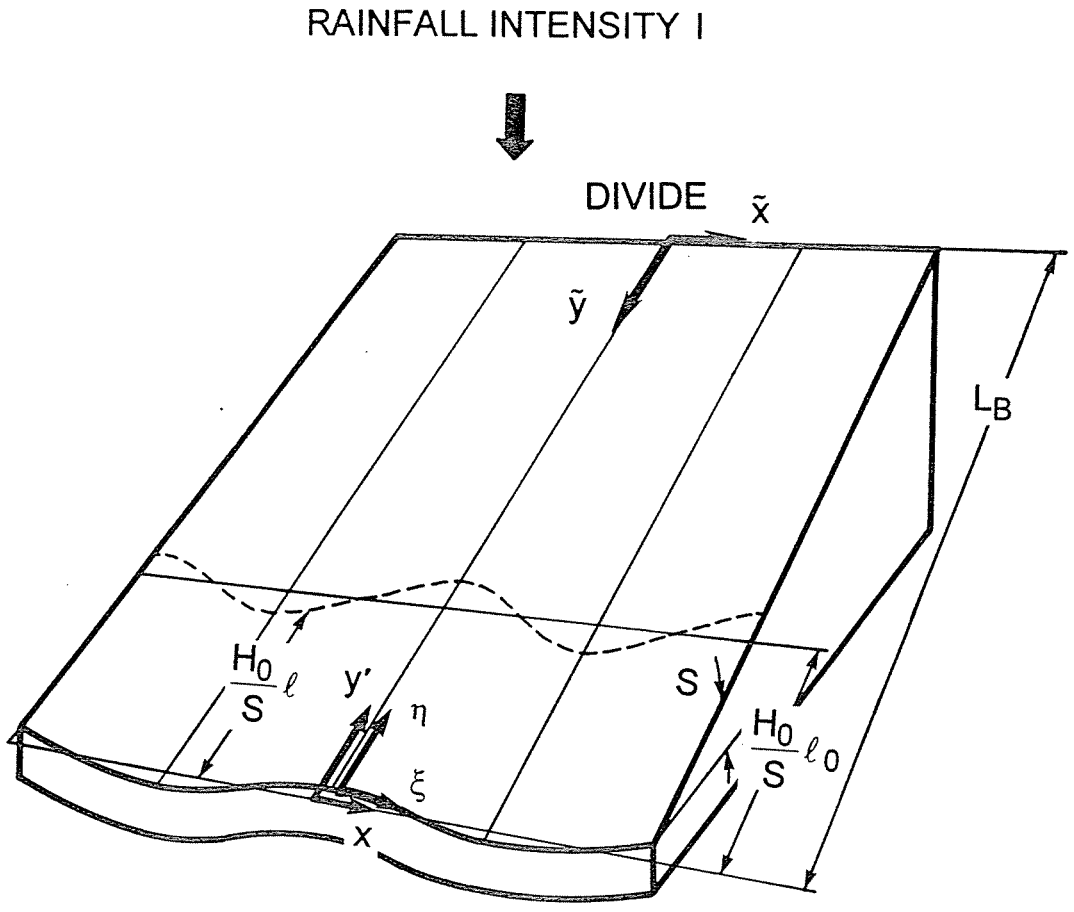

Figure 5–1. Schematic diagram showing a plateau with a sinuous step at the downstream end. Note that the plateau is tilted but absolutely flat. Flow is in the positive y direction.

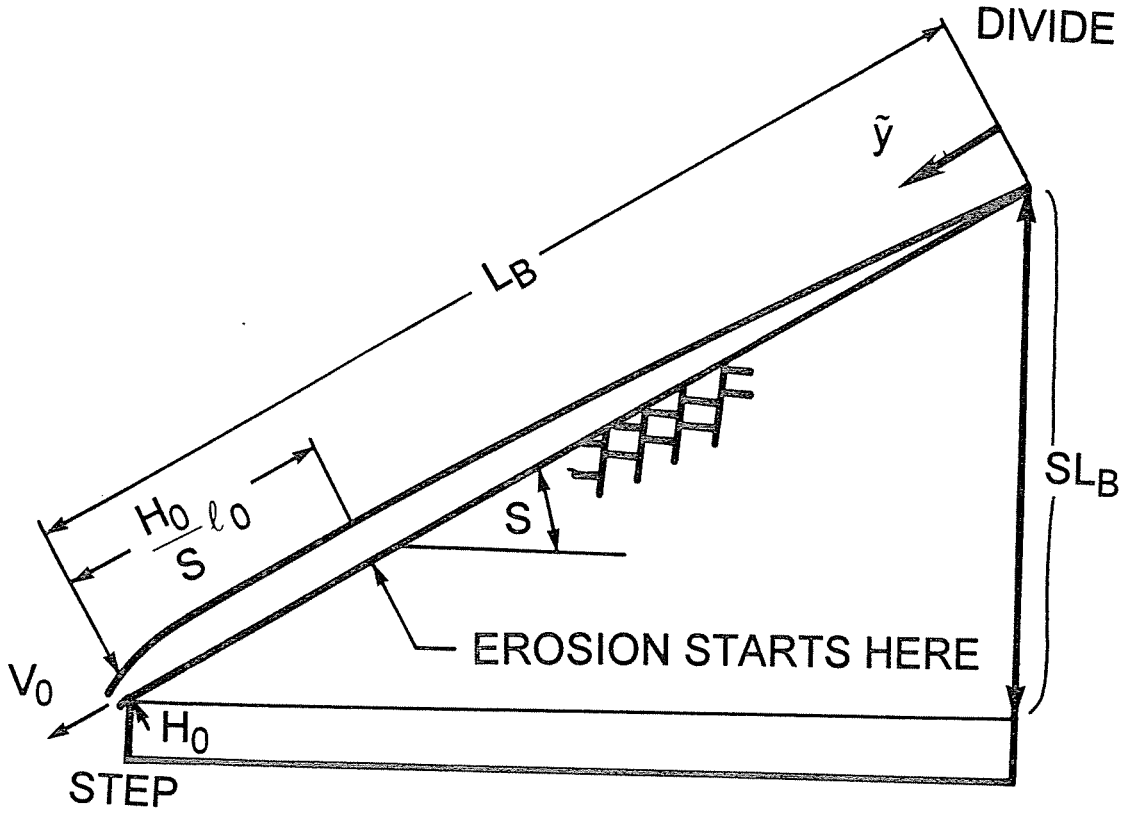

$$\psi = \frac{H_0}{SL_B}$$

Figure 5–2. Definition diagram parameter $\psi = H_0/(SL_B)$.

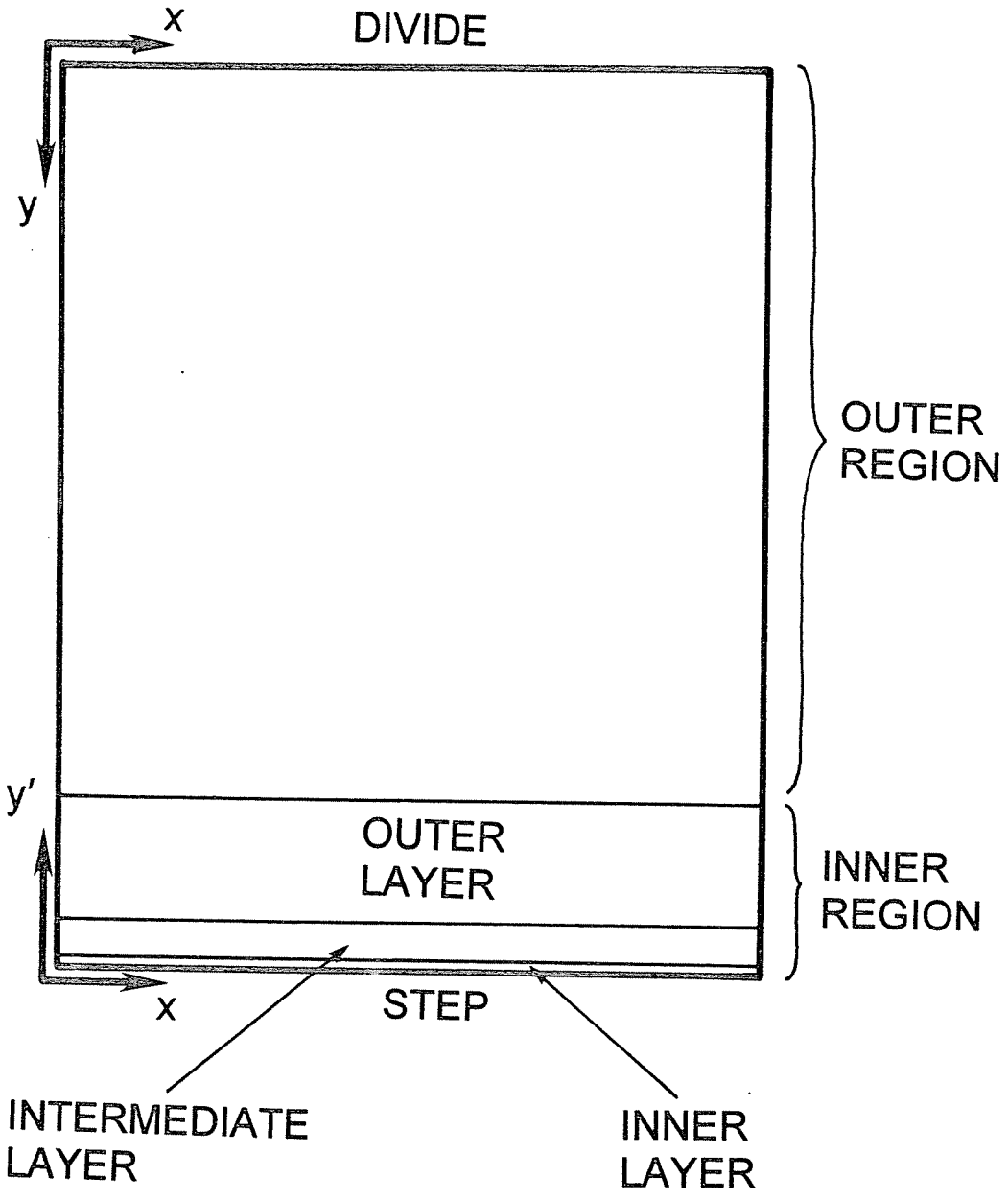

Figure 5–3. Schematic diagram showing the outer and inner regions, and the outer, intermediate and inner layers.

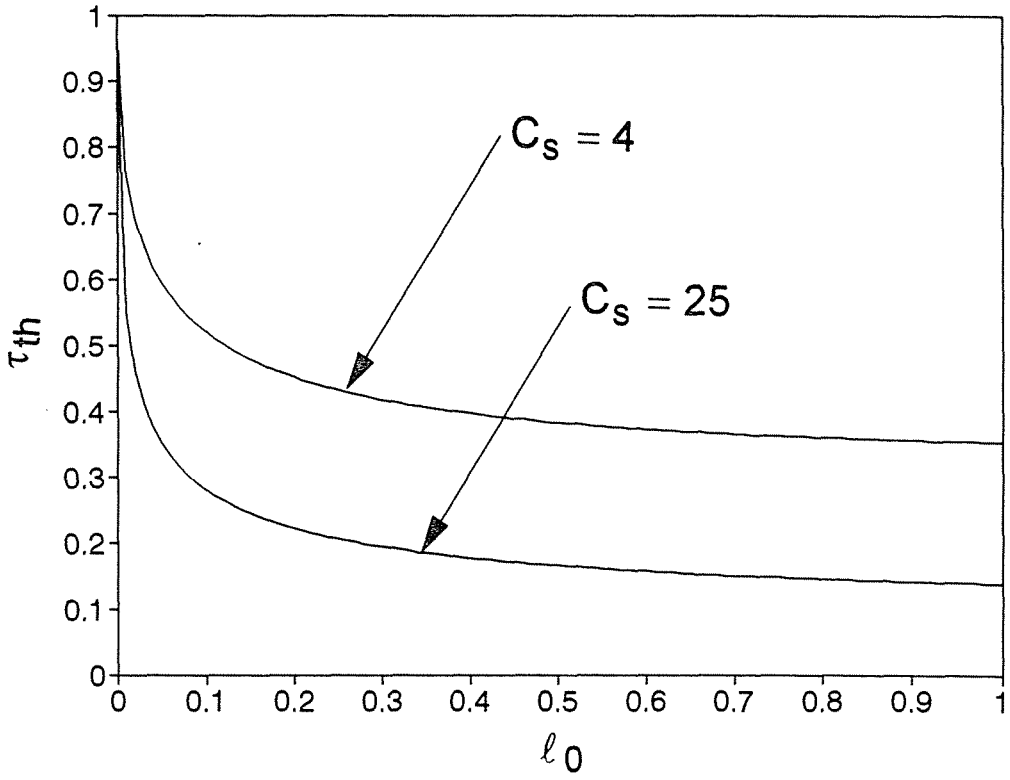

Figure 5–4. Dimensionless threshold shear stress τ_{th} versus ℓ_0 and C_s.

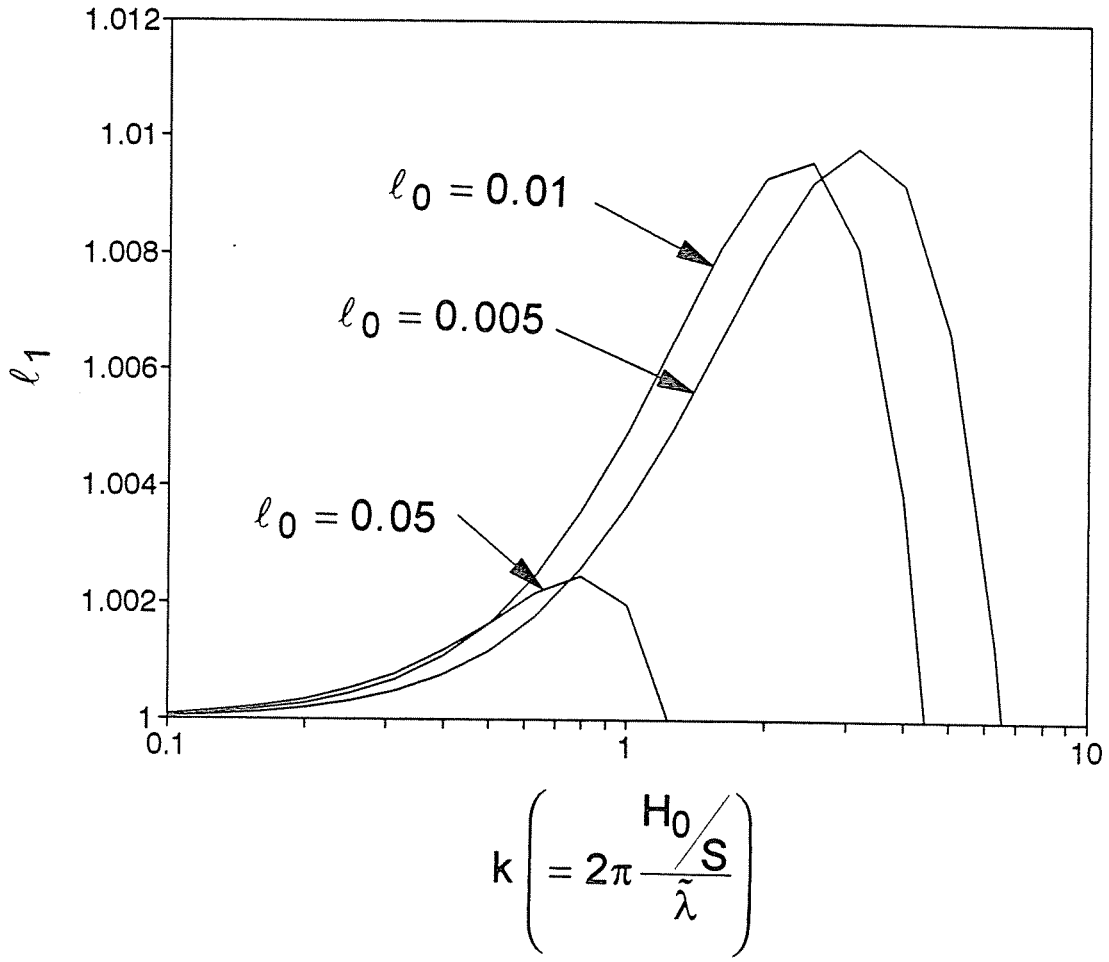

Figure 5–5a. Perturbed threshold distance ℓ_1 versus k and ℓ_0 for the case $C_s = 4$ (F = 0.5).

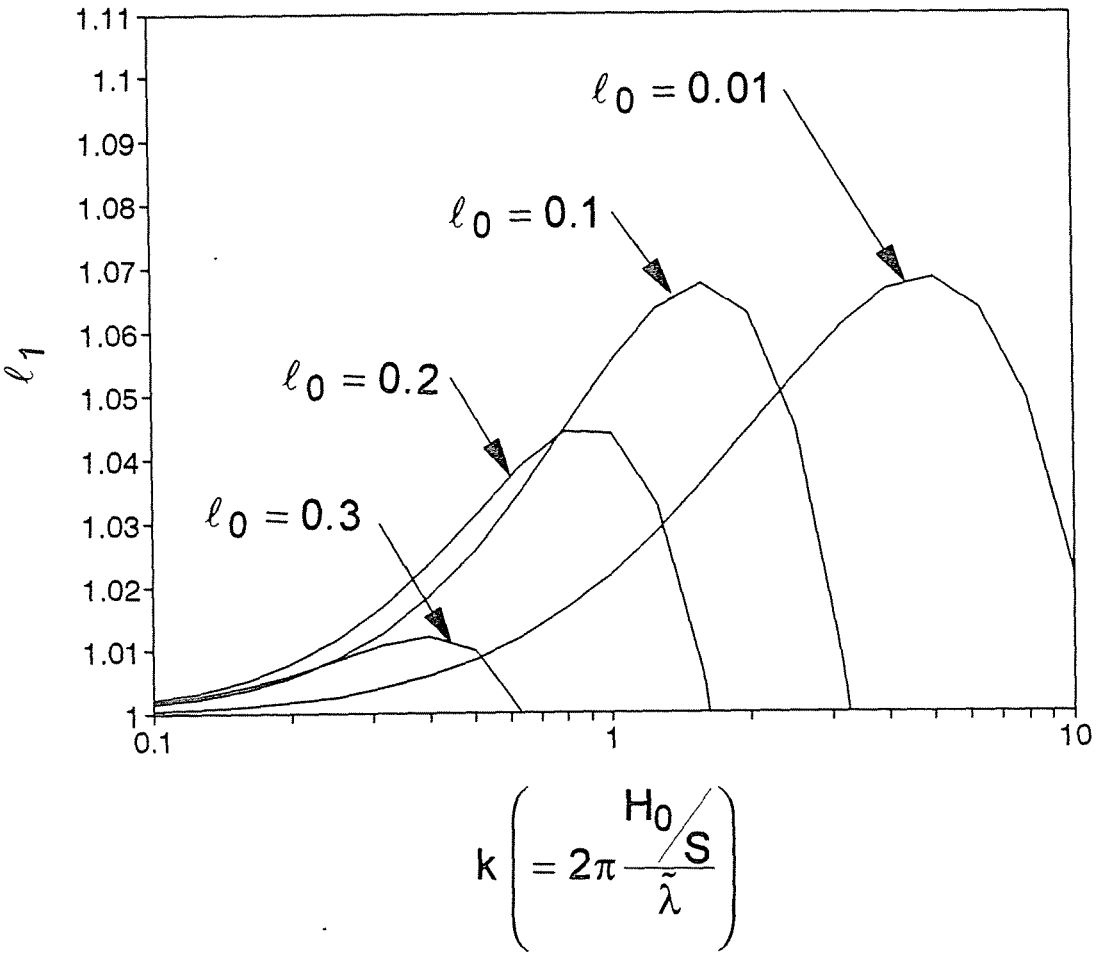

Figure 5–5b. Perturbed threshold distance ℓ_1 versus k and ℓ_0 for the case $C_s = 25$ (F = 0.2).

6. SUMMARY AND CONCLUSIONS

Theoretical models for explaining the process of drainage basin inception are presented. The models proposed here are clasified into three distinct kinds, the step foot erosion model, the upstream–driven threshold model, and the downstream–driven threshold model. The common concept of these three models is that channelization is caused by erosion due to a sheet flow on a plateau.

The first model analyzed is the step foot erosion model. A sheet flow over a flat but tilted plateau which has a perturbed step at the downstream end is considered. A perturbation technique is adopted to obtain the velocity distribution and water surface profile near the sinuous step. The analysis predicts that flow intensification is maximized near indentations, where it is a function of wavenumber and the Froude number. In this model, bed shear stress is assumed to be below the threshold value for erosion everywhere over the plateau. The surface is thus not subject to fluvial action, and the erosion can be assumed to be concentrated at the foot of the step. By relating the retreat speed of the step with discharge per unit width at the downstream end, a simple linear stability analysis is performed to obtain the wavenumber maximizing the growth rate of the perturbation. The analysis predicts that the growth rate is maximized for infinitely large wavenumber. The implication is that perturbation with infinitesimally small wavelength grows fastest, resulting in infinitesimally small basin spacing. It is concluded that the simple assumptions of the step foot erosion model cannot explain the process of drainage basin inception.

As a first attempt to include surface erosion, which was not considered in the step foot erosion model, a threshold hypothesis is introduced to explain the process

of upstream–driven channel inception. In this model, there is assumed to be a uniform rainfall. The resulting sheet flow on the plateau surface is characterized by an increasing bed shear stress toward the downstream end. A small wavy perturbation provided on the plateau surface results in a tendency for the flow to gather in the indentations. A perturbation technique is again used to obtain the velocity distribution and water surface profile over the wavy bed. When the streamwise backwater effect is small, it is found that the transverse Reynolds stress plays an important role in reducing flow intensification in the troughs for large values of k. The analysis predicts that the flow intensification is maximized when the wavelength is of the order of flow depth divided by slope. Performing a linear analysis with the use of the results obtained by the perturbation analysis, the distance from the upstream end to the threshold point is obtained. In accordance with the threshold hypothesis, it is found that a basin spacing of the order of flow depth divided by slope is predicted to dominate on the plateau.

The threshold hypothesis is finally applied to explain the process of downstream–driven channel inception. A plateau with a step–like overfall at the downstream end subject to a uniform rainfall is considered. It is found that when the streamwise backwater effect is sufficiently small, a boundary layer is formed in the vicinity of the step, in which the effects of rainfall and the Reynolds stress are both negligible. A perturbation analysis is brought to bear to obtain the velocity distribution and water surface profile near the sinuous step. It is found that in a certain zone near the step, flow intensification occurs upstream of indentations. Following the threshold hypothesis, the upstream shift of the threshold point caused by flow intensification is assumed to provide a criterion for channelization. Using a linear analysis, the magnitude of the shift is obtained as a function of wavenumber,

the distance from the downstream end of the plateau to the point where the base flow attain the threshold condition and the Froude number. The characteristic basin spacing is again found to be the order of flow depth divided by slope.

It should be emphasized that both threshold models predict a finite value of wavenumber which characterizes the preferential wavelength of perturbations associated with incipient channlization. A finite value of this characteristic wavenumber has never been obtained theoretically before. The observed basin spacing appears to be somewhat larger than that predicted in this study. This is perhaps due to both nonlinear and long–time processes, which cannot be adequately represented in the present linear analysis.

7. REFERENCES

Abrahams, A. D., Channel networks: a geomorphological perspective, Water Resources Research, 20(20), 161–168, 1984.

Ariathurai, R., and Arulanandan, K., Erosion rates of cohesive soils, Journal of Hydr. Div., ASCE, 104(2), 279–283, 1978.

Etcheverry, B. A., Irrigation practice and engineering, McGraw Hill Book Co., Inc., New York, N.Y., Vol.II, 1915, p.57.

Horton, R. E., Erosional development of streams and their drainage basins; Hydrophysical approach to quantitative mophology, Geol. Soc. Am. Bull., 56, 275–370, 1945.

Howard, A. D., Theoretical model of optimal drainage networks, Water Resources Research, 26(9), 2107–2117, 1990.

Ikeda, S., and Izumi, N., Width and depth of self–formed straight gravel rivers with bank vegetation, Water Resources Research, 26(10), 2353–2364, 1990.

Ikeda, S., and Izumi, N., Stable channel cross sections of straight sand rivers, Water Resources Research, 27(9), 2429–2438, 1991.

Kikkawa, H., Fluvial hydraulics, Maruzen, Tokyo, 1985 (in Japanese).

Loewenherz, D. S., Stability and the initiation of channelized surface drainage: a reassessment of the short wavelength limit, J. Geophys. Res., 96, 8453, 1991.

Luke, J., Special solutions for nonlinear erosion problems, J. Geophys. Res., 79(26), 4035–4040, 1974.

Meinhardt, H. A., Models of biological pattern formation, Academic Press, Berlin, 1982.

Montgomery, D. R., and Dietrich, W. E., Source area, drainage density and channel initiation, Water Resources Research, 25(8), 1907–1918, 1989.

Parker, G., Self–formed straight rivers with equilibrium banks and mobile bed, 1, The sand–silt river, J. Fluid Mech., 89(1) 109–125, 1978.

Partheniades, E., Erosion and deposition of cohesive soils, Journal of the Hydraulic Division, ASCE, 91(1), 105–139, 1965.

Rodi, W., Turbulence models and their application in hydraulics, IAHR, 1980.

Roth, G. and Siccardi, F., Hydrodynamic description of the erosional

development of drainage patterns, Water Resources Research, 25(2), 319–332, 1989.

Sawai, K., Ashida, K., and Imamoto, H., Stream network evolution and sediment yield on a bare slope. Proc. 3rd. Int. Symp. on River Sedimentation, S. Y. Wang, ed., University of Mississippi, 1986.

Shen, H. W., and Li, R. M., Rainfall effect on sheet flow over smooth surface, Journal of the Hydraulic Division, ASCE, 99(5), 771–792, 1973.

Smith, T., and Bretherton, F. B., Stability and the conservation of mass in drainage basin evolution, Water Resources Research, 8(6), 1506–1529, 1972.

Strahler, A. N., Dimensional analysis applied to fluvially eroded landforms, Bull. of the Geological Soc. of Amer., Vol.69, p. 279–300, 1958.

Webel, G. and Schatzmann, M., Transverse mixing in open channel flow, Journal of Hydraulic Engineering, 110(4), 423–435, 1984.

Willgoose, G., Bras, R., and Rodriguez–Iturbe, I., A coupled channel network growth and hillslope evolution model 1. Theory, Water Resources Research, 27(7), 1671–1684, 1991.

Willgoose, G., Bras, R., and Rodriguez–Iturbe, I., A coupled channel network growth and hillslope evolution model 2. Nondimensionalization and applications, Water Resources Research, 27(7), 1685–1696, 1991.

Yoon, Y. N., and Wenzel, H. G., Jr., Mechanics of sheet flow under simulated rainfall, Journal of the Hydraulics Division, ASCE, 97(9), 1367–1386.